

AD-A136 306

DEVELOPMENT OF X-RAY LASER MEDIA MEASUREMENT OF GAIN
AND DEVELOPMENT OF C..(U) ROCHESTER UNIV N Y LAB FOR
LASER ENERGETICS J FORSYTH FEB 83

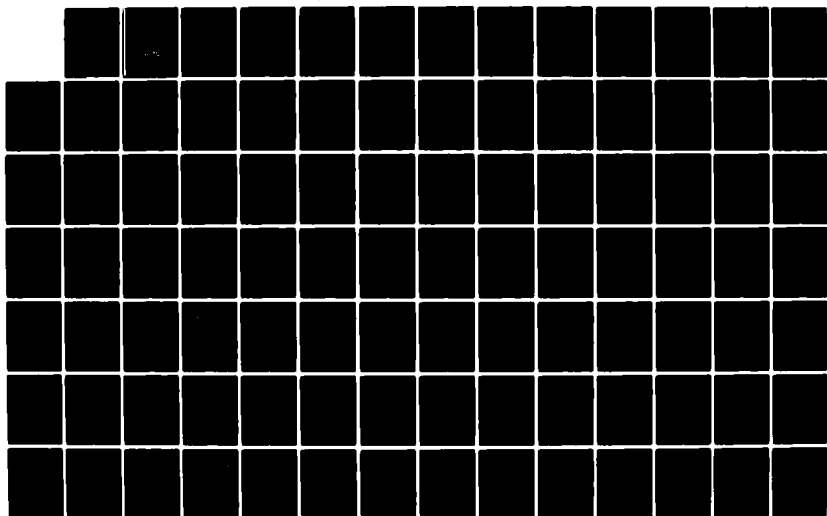
1/3

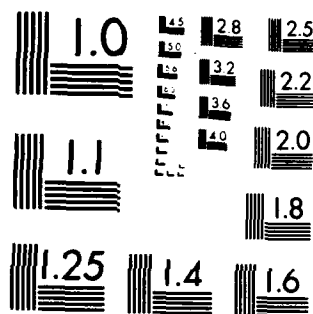
UNCLASSIFIED

AFOSR-TR-83-1136-VOL-2 AFOSR-81-0059

F/G 14/2

NL





MICROCOPY RESOLUTION TEST CHART
NATIONAL BUREAU OF STANDARDS-1963-A

AFOSR-TR- 83 - 1136

February 1983

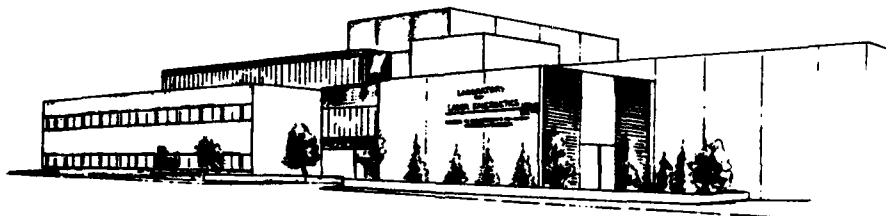
Volume 2

A136306

Annual Scientific Report
1 January 1982 - 31 December 1982

Grant AFOSR-81-0059

**Development of X-Ray Laser Media:
Measurement of Gain and Development of
Cavity Resonators for Wavelengths
Near 130 Angstroms**



Laboratory for Laser Energetics
University of Rochester
250 East River Road
Rochester, New York 14623

UR
LE

SELECTED
DEC 27 1983
A

83

12

27

Approved for public release;
distribution unlimited.

DTIC FILE COPY

Unclassified

SECURITY CLASSIFICATION OF THIS PAGE (When Data Entered)

REPORT DOCUMENTATION PAGE		READ INSTRUCTIONS BEFORE COMPLETING FORM
1. REPORT NUMBER AFOSR-TR- 83 - 1136	2. GOVT ACCESSION NO.	3. RECIPIENT'S CATALOG NUMBER
4. TITLE (and Subtitle) DEVELOPMENT OF X-RAY LASER MEDIA: MEASUREMENT OF GAIN AND DEVELOPMENT OF CAVITY RESONATORS FOR WAVELENGTHS NEAR 130 ANGSTROMS		5. TYPE OF REPORT & PERIOD COVERED Annual Scientific Report 1/1/82 - 12/31/82
		6. PERFORMING ORG. REPORT NUMBER
7. AUTHOR(s) Dr. James Forsyth		8. CONTRACT OR GRANT NUMBER(s) AFOSR-81-0059
9. PERFORMING ORGANIZATION NAME AND ADDRESS Laboratory for Laser Energetics, College of Engineering & Applied Science, University of Rochester, 250 E. River Rd., Rochester, NY 14623		10. PROGRAM ELEMENT, PROJECT, TASK AREA & WORK UNIT NUMBERS 61102F 2301/A8
11. CONTROLLING OFFICE NAME AND ADDRESS Air Force Office of Scientific Research /NP Bolling Air Force Base Washington, D. C. 20332		12. REPORT DATE February 1983
		13. NUMBER OF PAGES 161
14. MONITORING AGENCY NAME & ADDRESS (if different from Controlling Office)		15. SECURITY CLASS. (of this report) Unclassified
		15a. DECLASSIFICATION/DOWNGRADING SCHEDULE
16. DISTRIBUTION STATEMENT (of this Report) Approved for public release; distribution unlimited.		
17. DISTRIBUTION STATEMENT (of the abstract entered in Block 20, if different from Report)		
18. SUPPLEMENTARY NOTES		
19. KEY WORDS (Continue on reverse side if necessary and identify by block number) X-Ray, Reflectors, Laser, Plasma		
20. ABSTRACT (Continue on reverse side if necessary and identify by block number) A two part study of soft x-ray laser media is presented. Experimental observation of significant population inversion on the Balmer alpha transition in hydrogen-like fluorine at 81 Å in a line-focus laser plasma is reported. An analysis of the expected performance of soft x-ray multilayer reflects is presented. This volume discusses reflecting properties of X-ray multilayer devices.		

DD FORM 1473
1 JAN 73

EDITION OF 1 NOV 65 IS OBSOLETE
S/N 0102-LF-014-6601

Unclassified

SECURITY CLASSIFICATION OF THIS PAGE (When Data Entered)

3.0 Reflecting Properties of X-Ray Multilayer

Chapter I-III

AIR FORCE OFFICE OF SCIENTIFIC RESEARCH (AFSC)
NOTICE OF TRANSMITTAL TO DTIC
This technical report has been reviewed and is
approved for public release IAW AFR 190-12.
Distribution is unlimited.
MATTHEW J. KENPER
Chief, Technical Information Division

Reflecting Properties of X-Ray Multilayer Devices

by

Alan E. Rosenbluth

James M. Forsyth

Institute of Optics

College of Engineering and Applied Science

University of Rochester

Rochester, New York

1982



6

DTIC COPY INSPECTED 1	
Reflecting Properties of X-Ray Multilayer Devices	
Alan E. Rosenbluth / James M. Forsyth	
Post	Special
A-1	

Abstract

In recent years much progress has been reported in the fabrication of multilayer reflectors for x-ray and XUV radiation ($1\text{\AA} - 600\text{\AA}$).

The characteristic optical properties of materials at these wavelengths (dielectric constants are complex and approach unity), allow one to obtain solutions to Maxwell's equations for a quasi-periodic reflector whose layers may contain arbitrary index gradients.

This solution can be formulated as a difference equation that propagates the amplitude reflectance across each layer pair. The difference equation resembles the Airy summation for single layers, but has a simpler Ricatti form.

From the difference equation one can derive design criteria for maximization of multilayer reflectivity. These criteria provide guidance in the selection of appropriate multilayer materials, and have been used to derive approximate scaling laws for multilayer reflecting properties.

The difference equation forms the basis for a non-perturbative analysis of multilayer reflectivity in the presence of random thickness errors (including the residual loss in reflectivity that remains when reflectance monitoring is used to compensate for thickness errors during multilayer fabrication). Under certain circumstances, the difference equation can be used to analyze the effect of interfacial roughness on multilayer reflectivity. Accurate closed-form solutions to such stochastic problems can be found by neglecting higher order powers in the incoherent component of multilayer reflectivity.

The reflecting properties of x-ray multilayers may contain qualitative signatures that correspond to these different kinds of structural defects.

Our theoretical results indicate that significant constraints on efficiency and field of view are involved in using multilayers to extend optical technology to the x-ray regime. Examples discussed include microscopes operating at short x-ray wavelengths ($1\text{\AA} - 2\text{\AA}$), where multilayers can provide a useful level of spectral selectivity, and resonant cavities for projected x-ray lasers ($50\text{\AA} - 200\text{\AA}$), where the coupling of the intracavity field to the amplifier can be strongly increased if the cavity configuration is based on two multilayers that are tuned to reflect at normal incidence.

Table of Contents

Acknowledgments.....	ii
Abstract.....	iii
Table of Contents.....	v
List of Figures.....	ix
List of Tables.....	xii
Chapter I Introduction	
Section I-1 - Literature Review.....	I-1-1
Part A) X-Ray Multilayer Reflectors.....	I-1-1
Part B) Crystal Diffraction.....	I-1-6
Part C) Thin Film Formalisms.....	I-1-9
Section I-2 - Outline of Text.....	I-2-1
Chapter II Theoretical Analysis of Multilayer Reflectors	
Section II-1 - Analytic Formalism.....	II-1-1
Part A) Introduction.....	II-1-1
Part B) Notation, Preliminary Results, and Characterization of Approximations.....	II-1-3
Part C) Characteristic Matrix Solution for the X-Ray Regime.....	II-1-15

Part D) Difference Equation for Amplitude Reflectance.....	II-1-20
Section II-2 - Defect-Free Multilayers.....	II-2-1
Part A) Reflectivity of Periodic Multilayers.....	II-2-1
Part B) Structural Optimization of Periodic Multilayers.....	II-2-9
Part C) Optimum Materials Choices.....	II-2-26
Section II-3 - Scaling of Multilayer Reflection Properties.....	II-3-1
Section II-4 - Non-Periodic Multilayer Designs.....	II-4-1
Section II-5 - Effect of Accumulating Random Thickness Errors on Multilayer Reflectivity.....	II-5-1
Part A) Introduction.....	II-5-1
Part B) Analysis of Accumulating Thickness Errors.....	II-5-3
Part C) Discussion of Solution.....	II-5-37
Section II-6 - Non-Accumulating Random Thickness Errors.....	II-6-1
Part A) Introduction.....	II-6-1
Part B) First Method of Analysis.....	II-6-7
Part C) Second Method of Analysis.....	II-6-14
Part D) Discussion.....	II-6-19
Chapter III Applications of X-Ray Multilayer Coatings	
Section III-1 - General Considerations.....	III-1-1
Part A) Introduction.....	III-1-1

Part B) General Constraints on	
Multilayer Performance.....	III-1-2
Section III-2 - Cavity Mirrors for X-Ray Lasers.....	III-2-1
Part A) Multilayer Coated Cavity Mirrors.....	III-2-1
Part B) Ring Cavity.....	III-2-8
Part C) Damage.....	III-2-14
Section III-3 - Multilayer Coatings for	
Short Wavelength X-Ray Microscopy.....	III-3-1
Part A) Introduction.....	III-3-1
Part B) Calculation of Performance.....	III-3-6
Chapter IV Conclusion	
Section IV-1 - Summary of This Work.....	IV-1-1
Part A) Introduction.....	IV-1-1
Part B) Summary of Chapters II and III.....	IV-1-4
Section IV-2 - Suggestions for Future Work.....	IV-2-1
Part A) Interfacial Roughness.....	IV-2-1
Part B) Future Work.....	IV-2-21
Bibliography.....	V-1-1
Appendix 1 Perturbation Solution for the Unit Cell.....	A-1-1
Appendix 2 Difference Equation for Amplitude Reflectivity.....	A-2-1
Appendix 3 Reflectivity of a Periodic Multilayer with J Cells.....	A-3-1
Appendix 4 Sufficient Criterion for the Bragg Condition.....	A-4-1

Appendix 5	Comparison of Absorption and Dispersion Corrections.....	A-5-1
Appendix 6	Algorithm for Optimizing Division Parameter.....	A-6-1
Appendix 7	Peak Reflectivity of Periodic Multilayers.....	A-7-1
Appendix 8	Demonstration that Periodic Multilayer has Extremum Reflectivity.....	A-8-1
Appendix 9	Two-by-Two Optimization of Periodic Multilayers.....	A-9-1
Appendix 10	Accumulating Thickness Errors Outside Steady-State Regime.....	A-10-1
Appendix 11	Phenomenological Solution for Multilayer Reflectivity in the Presence of Non-Accumulating Errors.....	A-11-1
Appendix 12	Effect of Interlayer Diffusion on Cell Parameters.....	A-12-1
Appendix 13	Analysis of Ring Cavity.....	A-13-1
Appendix 14	Scalar Model of Smoothing Film Roughness.....	A-14-1
Appendix 15	Analysis of Roughening Films and Columnar Films.....	A-15-1
Appendix 16	Materials Combinations that Maximize Integrated Reflectivity.....	A-16-1
Figure II-2-4	(color illustration).....	Bound at back

List of Figures

	Page
Figure II-1-1.....Characteristic Matrix Analysis of X-Ray Structures.....	II-1-5
Figure II-1-2.....Coordinate System for CM Solution.....	II-1-2
Figure II-1-3.....Propagation Equation for Amplitude Reflectance.....	II-1-22
Figure II-2-1.....Structure of Unit Cell - Bilayer Reflector.....	II-2-7
Figure II-2-2.....Comparison of Absorption Correction to Dispersion Correction.....	II-2-19
Figure II-2-3.....Reflectance of W/C Multilayer.....	II-2-3
Figure II-2-4.....Optimum X-Ray Multilayer Parameters.....	Bound at back of text
Figure II-2-5.....Reflectivity Attainable from Tungsten and Carbon.....	II-2-31
Figure II-3-1.....Scaling of Optimum Thickness Ratio.....	II-3-2
Figure II-3-2.....Wavelength Scaling of Unit Decrement.....	II-3-5
Figure II-3-3.....Angular Width of Reflection Profile.....	II-3-12
Figure II-4-1.....Comparison of Optimization Schemes.....	II-4-3
Figure II-5-1.....Deterministic versus Non-Deterministic Components of Reflected Beam.....	II-5-17
Figure II-5-2.....Successive Approximations for the Expected Amplitude Reflectance.....	II-5-24

Figure II-5-3.....Effect of Random Thickness Errors -	
First Example.....	II-5-32
Figure II-5-4.....Effect of Random Thickness Errors -	
Second Example.....	II-5-34
Figure II-5-5.....Effect of Random Thickness Errors -	
Third Example.....	II-5-35
Figure II-6-1.....Effect of Non-Accumulating	
Thickness Errors.....	II-6-21
Figure III-1-1.....Scaling of Reflectivity Degradation.....	III-1-8
Figure III-2-1.....Proposed Cavity Configuration.....	III-2-3
Figure III-2-2.....Other Cavity Configurations.....	III-2-5
Figure III-3-1.....Correction of Astigmatism by	
Successive Grazing Reflections.....	III-3-2
Figure III-3-2.....Multilayer-Coated	
X-Ray Microscope Performance.....	III-3-7
Figure IV-2-1.....Categories of Roughness.....	IV-2-2
Figure IV-2-2.....Coordinate System for	
Scattered Radiation.....	IV-2-7
Figure IV-2-3.....Effect of Roughness I.....	IV-2-16
Figure IV-2-4.....Effect of Roughness II.....	IV-2-20
Figure A-6-1.....Algorithms for Obtaining	
Optimum Division Parameter.....	A-6-6
Figure A-9-1.....Structure of Unit Cell in a Bilayer Reflector	
(Non-Centrosymmetric Geometry).....	A-9-2

Figure A-10-1.....	Test of Approximate Solution for	
	Non-Steady-State Coherent Reflectivity.....	A-10-7
Figure A-10-2.....	Random Component of Reflected Beam.....	A-10-10
Figure A-11-1.....	Unit Cell Decomposition for	
	Non-Accumulating Errors.....	A-11-2
Figure A-16-1.....	Explanation of Entries in Table A-16-1.....	A-16-2

List of Tables

Table II-2-1.....Optimum X-Ray Multilayer Parameters.....	II-2-28
Table III-2-1.....Optimum Materials for Ring Cavity.....	III-2-11
Table A-16-1.....Materials Combinations that Maximize Integrated Reflectivity.....	A-16-2

Chapter I Introduction

Section I-1 - Literature Review

Part A) X-Ray Multilayer Reflectors

In recent years much progress has been reported in the fabrication of reflecting multilayers having period lengths in the 100\AA regime (Haelbich and Kunz, 1976; Haelbich, Segmuller, and Spiller, 1979; Barbee and Keith, 1979; Spiller et al., 1980; Barbee, 1981; Spiller, 1982b; Underwood and Barbee, 1982). Such devices may be regarded either as short-wavelength multilayer coatings, or as artificial crystals having large spacings between the diffracting "planes". (There are few true crystals having spacings larger than about 12\AA .)

These devices should prove useful for the spectral region below $\sim 600\text{\AA}$ (Spiller, 1972, 1976). In this part of the spectrum all materials have complex dielectric constants that depart only slightly from unity; i.e. materials are absorbing and are incapable of providing a high single-surface reflectivity.

In this work we present a theoretical analysis of the reflecting properties of x-ray multilayers. In the present chapter we review the field, and also discuss related topics (and associated terminology) from other fields, such as x-ray diffraction theory.

According to Barbee (1982), the first attempts to fabricate x-ray multilayers (generally unsuccessful) were made by Koeppel (1929) and Deubner (1930).

More recently, Dinklage (1967) succeeded in fabricating iron/magnesium reflectors having a reasonably stable reflecting power (room temperature half-life about one year). Dinklage has not reported an absolute reflectivity for these structures.

Spiller (1972, 1976) recognized that in an absorbing multilayer it is not necessarily desirable to minimize the absorption of both the high and the low index layers. By making the thickness of a strongly absorbing high index layer substantially thinner than one quarter-wave, one decreases the absorption of the layer more rapidly than one does the reflectivity, allowing in principle for a more than compensating increase in the total number of reflecting layers. Larger total reflectivities are then obtained when a dense, high Z material is used in high index layers that are alternated with low absorption spacing layers.

Haelbich and Kunz (1976) achieved 1.28 peak reflectivity at 150\AA (15° incidence to the normal) from a 9 layer structure of gold and carbon that was designed according to the above considerations. Carbon was chosen as a spacer material because of its low absorption, and because it does not diffuse readily with metals.

Haelbich, Segmuller, and Spiller (1979) used a rhenium/tungsten alloy (ReW) as a high index layer and carbon as a low index layer to obtain 9.58 peak reflectivity (15° angle of incidence) with 7 layers at 200\AA . The ReW alloy was found to provide smoother layers than did other high density

materials such as gold.

In these early efforts, the number of participating layers that the structures could contain was limited by an inability to precisely control the layer thicknesses, and so avoid the accumulation of dephasing due to random errors (Haelbich and Kunz, 1976; Haelbich, Segmuller, and Spiller, 1979). In order to reach absorption-limited reflectivities, x-ray multilayers must contain a larger number of layer pairs than are required in optical multilayers, because at x-ray wavelengths the interaction of an individual unit cell with the incident beam is weak. (As a rule of thumb, a multilayer should contain more than $(600\text{\AA} / \lambda)^2$ pairs of layers in order to achieve absorption-limited reflectivity at normal incidence; see sec. II-3.)

In the above experiments, the deposited materials were transferred to the substrates by vacuum evaporation. Barbee and Keith (1979), and Barbee (1982), report the fabrication of tungsten/carbon multilayers with periods as short as 15\AA using a vacuum sputtering technique. Sophisticated deposition apparatus and procedures appear to be the key to their achievement of high quality diffracting structures.

Spiller et al. (1980) report the implementation of an in-situ reflectance monitoring technique in which the interference oscillations of a reflected x-ray probe beam are monitored during multilayer fabrication. Such a system directly monitors the phasing between the partially deposited upper layer and the preceding stack (in contrast to the usual crystal oscillator which monitors the (mass) thickness of the upper layer alone). In essence, the reflectance monitoring technique allows the

reflection component from the upper layer to be brought into phase with the preceding stack, despite any thickness errors that this stack may contain.

At present Spiller's group at IBM and Barbee's group at Stanford may be regarded as the dominant centers for research in this field. X-ray multilayers have also recently been fabricated by Soviet researchers using laser evaporation of the materials to be deposited (Gaponov et al., 1981).

The most commonly used materials in multilayers to date are carbon for the low index layer and tungsten or rhenium/tungsten alloy for the high index layer. The optical constants of rhenium ($Z = 75$) and tungsten ($Z = 74$) are generally comparable, so the nominal performance of the two materials should be similar in the absence of defects. We will generally use tungsten/carbon multilayers when presenting numerical examples. In doing so we use preliminary versions of the optical constants data in Henke et al. (1982), generously provided to us by the authors.

Vinogradov and Zeldovich (1977) present an analytic treatment of reflection from periodic x-ray multilayers. They use (normal incidence) coupled wave equations whose unknowns are the envelope functions of high-frequency electromagnetic field oscillations. (The "carrier frequency" is taken to be the spatial periodicity of the multilayer structure.) Such coupled-wave equations apply to multilayer reflectivity when the coupling constant is weak, as it is in the x-ray case. Vinogradov and Zeldovich obtain expressions for the reflectivity of a periodic multilayer containing an arbitrary number of layers. They also determine the condition which optimizes the ratio in thickness of the two

different layers, and finally they derive what is in effect a hybrid optimization condition that gives the optimum total thickness of the period, when the thickness ratio is also optimized. (The two relations together thus implicitly give a refractive correction to Bragg's law.)

Part B) Crystal Diffraction

In many respects, reflection from x-ray multilayers is similar to diffraction from crystals in the Bragg mode (atomic planes parallel to the crystal surface); this is particularly true in the case of periodic multilayers.

Most crystals have period lengths (or "d-spacings") that are a few angstroms or less between adjacent diffracting planes, so that the longest wavelength that can be reflected from most crystals is less than ten angstroms. (The longest wavelength that can be reflected is approximately twice the period length, which is referred to as the "2d-spacing". The basic period of a crystal (as a physical entity) is usually referred to as the "unit cell".)

The optical constants of materials in the soft x-ray region ($5\text{\AA} - 125\text{\AA}$) and the extreme vacuum ultraviolet ($125\text{\AA} - 600\text{\AA}$) have a qualitative similarity to the optical constants of materials at conventional x-ray wavelengths (0.5\AA to 5\AA).

In the high frequency (but non-relativistic) regime where the radiation-induced electron oscillations are limited primarily by electron inertia rather than by coupling with the atom ("free-electron regime"), the real part of the index of refraction (less unity) scales as λ^2 , while the imaginary part scales as λ^4 (Heitler, 1954, p.208), so that at short x-ray wavelengths absorption becomes small compared to dispersion.

Since the real part of the index of refraction is less than one for electromagnetic frequencies above the plasma frequency, "total external reflection" of x-rays can occur when the angle of incidence to a single

reflecting surface is less than the critical angle given by

$\xi_c = \sqrt{2(1 - \text{Re}(n))}$ radians, with n the index of refraction of the substrate (James, 1965, p.171). X-ray reflectivities that approach unity can therefore be obtained at glancing angles (typically $\sim 89^\circ$ to the normal) when absorption is small. Total external reflection of short wavelength x-rays can therefore be quite efficient.

In the soft x-ray region the imaginary part of the index of refraction can become comparable in magnitude to the real part (less unity). The effective number of free electrons per atom (known as the "atomic scattering factor") must then be treated as a complex quantity whose dependence on wavelength is irregular due to atomic resonances. (However, it appears from the data in (Henke, et al., 1982) that for most materials the imaginary part of the index scales very broadly as λ^2 in the soft x-ray region.)

The most rigorous theory of diffraction from crystals is generally considered to be the dynamical theory of Ewald and von Laue (Batterman and Cole, 1964; James, 1965, p.413). In the Ewald - von Laue theory the physical structure of the crystal is represented by a complex dielectric constant that is spatially periodic, and that has as interaction with radiation given by Maxwell's material equations.

The dynamical theory can be used to treat multiple reflection processes in which an incident beam interacts resonantly with more than one set of atomic planes at once, but in the most common case only one pair of structural spatial frequency components (positive and negative), plus a DC component, are considered to be active at one time.

From a fully classical point of view, the polarizability can be taken to be proportional to a local electron density, but under a semiclassical model the polarizability must be calculated quantum mechanically. At short wavelengths where the dipole approximation breaks down, the dielectric constant will therefore depend on the scattering angle. This effect is small if the 2d-spacing is larger than an individual atom.

When the surface of a thick crystal is cut parallel to the diffracting planes, the reflectivity predicted by the Ewald - von Laue theory is the same as that obtained with the earlier theory of Darwin and Prins (James, 1965, p.429). In essence, the Darwin-Prins solution is obtained by requiring that the change in the forward and backward-traveling amplitudes, as each cell is traversed, be consistent with the cell reflectance and transmittance.

Part C) Thin Film Formalisms

Kogelnik (1976) has derived (from coupled wave equations) a differential equation that propagates the amplitude reflectance through a quasi-periodic structure. This differential equation is similar to the difference equation with which we treat x-ray multilayer reflectivity in Chapter II.

We derive our difference equation from a characteristic matrix solution for the fields within the unit cell of an x-ray multilayer; this unit cell may contain an arbitrary one-dimensional index gradient. Such a solution exists (in principle) for any medium in which the index of refraction varies only in one dimension (Born and Wolf, 1976, p.51). The characteristic matrix solution for homogeneous layers is commonly used in optical thin-film calculations.

Although this work centers on the analysis of structures with a one-dimensional index variation, we summarize in Chapter IV the results of a preliminary analysis we have made of the effect of interfacial roughness on multilayer reflectivity.

This analysis is based on that of Eastman (1978), who showed that a one-dimensional formalism can be used to treat interfacial roughness when the roughness has a sufficiently gradual variation within the layers. Eastman's methods have been summarized and extended by Carniglia (1981).

Shellan et al. (1978) use a coupled wave formalism to make a perturbation treatment of the effect of random thickness errors in dielectric multilayers. Our non-perturbative analysis of random thickness errors in x-ray multilayers is presented in sec. II-5.

Section I-2 - Outline of Text

This work contains four chapters, each of which is divided into sections, and parts of sections. The present chapter reviews the field, Chapter II presents our theoretical analysis of x-ray multilayer reflectors, Chapter III uses this theory to discuss applications for x-ray multilayers, and Chapter IV summarizes our results.

The text uses a common enumeration system to number pages, equations, figures and tables. As an example, the first equation of section 1 in Chapter II is numbered "eq. II-1-1", the second is eq. II-1-2, and so on through the final equation of the section (eq. II-1-25). The first equation of the next section is then eq. II-2-1, and so forth. The same system is used to number pages, figures, and tables.

In sec. II-1 we introduce the basic formalism for our treatment of reflection from x-ray multilayers. Like the Ewald - von Laue theory of diffraction from crystals, we begin with a physical description of the multilayer in terms of a spatially varying complex dielectric constant. We assume, as is natural for multilayers, that the dielectric constant varies only in one dimension. This assumption has an analogy with the Ewald - von Laue theory, in that we, in effect, neglect a portion of that set of spatial frequencies which are also neglected in the Ewald - von Laue theory when only one reflection is regarded as being active (see above); for example, in the case of a periodic multilayer, we, in effect, neglect any spatial frequencies that are not parallel to the active pair of spatial frequencies (assumed to be normal to the

substrate).

However, unlike the dynamical theory, we do not require that the multilayer be periodic; in effect we allow each of the active spatial frequencies to be replaced by a narrow continuum of spatial frequencies.

Our formalism does not introduce such a continuum explicitly, but instead makes direct use of the structural properties of the discrete cells. This is accomplished with a difference equation that propagates the amplitude reflectance from cell to cell (derived in sec. II-1).

In sec. II-2 we consider the reflectivity of ideal, defect-free multilayers; our main interest is in the optimization of the layer thicknesses and materials.

Sec. II-3 considers the angular and spectral scaling of the reflection properties of tungsten/carbon multilayers.

Sec. II-4 considers the possible utility of aperiodic reflector designs, with particular emphasis on the layer by layer optimization scheme of Carniglia and Apfel (1980). The in-situ reflectance monitoring technique reported by Spiller et al. (1980) lends itself naturally to this kind of design procedure.

Sec. II-5 considers the effect of random errors in the layer thicknesses. We make the problem tractable by neglecting higher powers in a quantity that may be regarded as the incoherent reflectivity of the degraded structure. In this way the analysis is able to treat a full range of error magnitudes, from those which cause only a slight decrease in reflectivity, to those large enough to substantially degrade the reflectivity.

Spiller et al. (1980) have verified experimentally that in-situ reflectance monitoring strongly reduces the degradation in reflectivity caused by thickness errors. We model this effect quantitatively in sec. II-6. However, due to the complicated interaction involved in the monitoring process, the results of sec. II-6 should probably not be regarded as strongly quantitative predictions.

In the first section of Chapter III we discuss points of general relevance concerning the application of x-ray multilayers. In sec. III-2 we discuss the possibility of using x-ray multilayers to form cavity mirrors for projected x-ray lasers ($\lambda \sim 100\text{\AA}$). Sec. III-3 considers the utility of multilayer coatings in short wavelength x-ray microscopes ($\lambda \sim 1\text{\AA}$).

The first section of Chapter IV summarizes the results of the preceding chapters. Sec. IV-2 discusses possible avenues for future research, and also summarizes a preliminary investigation of the effect of interfacial roughness on multilayer reflectivity. In terms of the above discussion, the analysis of sec. IV-2 may be said to permit the continuum of spatial frequencies in the multilayer structure to have a narrow extent in the non-normal direction.

Chapter II Theoretical Analysis of Multilayer Reflection

Section II-1 - Analytic Formalism

Part A) Introduction

We have seen in the preceeding chapter that the dynamical theory of x-ray diffraction is based on the assumption of a spatially-varying, complex dielectric constant which has an interaction with radiation defined by Maxwell's material equations. Despite the seemingly ad-hoc nature of this assumption, the dynamical theory is generally considered to be the most rigorous theory of x-ray diffraction, and has been found to yield fairly reliable results with crystalline structures having angstrom periodicities (Batterman and Cole 1964).

Because such assumptions permit the use of classical techniques of electromagnetic theory, we will also use them in our treatment of x-ray multilayer reflectors. However, in our case the effective dielectric constant need not be assumed to be periodic, but must, on the other hand, be assumed to be a purely one-dimensional function varying only in the direction perpendicular to the multilayer surface.

Our formalism will tie in closely with traditional methods of thin-film optics. It will be applicable to a broader range of problems involving x-ray multilayers than are other x-ray formalisms, and will provide analytic

solutions in the x-ray regime to problems that require cumbersome numerical calculations if traditional thin-film methods are used.

Our formalism will contain the structural properties of the different cells explicitly, whereas the Ewald-von Laue or coupled-wave formalisms are based on the Fourier components of the diffracting structures. Fourier components are somewhat inconvenient to use when analyzing aperiodic multilayers.

An additional advantage of our formalism is that it proceeds via a well-characterized series of assumptions from standard results of electromagnetic theory. For this reason our solutions include certain higher-order terms that must be included in order to obtain even a lowest-order analysis of certain problems of interest. Such problems include the determination of the layer thicknesses in multilayers made by in-situ reflectance monitoring (sec. II-4) and the determination of the effect on reflectivity of random thickness errors in multilayer structures (sec. II-5).

Part B) Notation, Preliminary Results, and Characterization of Approximations

The core of our formalism is an analytic solution for the electromagnetic fields inside the unit cell of an x-ray multilayer that has an arbitrary gradient structure. In the optical regime, such a solution cannot be obtained analytically with arbitrary gradients (see below); we are able to obtain analytic solutions in the x-ray case by treating the decrement in the dielectric constant as a small quantity.

It has been shown (Born and Wolf, 1975, p.51) that when the dielectric constant has a purely one-dimensional spatial variation along a direction z , Maxwell's partial differential equations can be separated into ordinary differential equations involving variables $U(z)$ and $V(z)$, where U and V are defined in terms of the electromagnetic fields through the relations

$$\begin{aligned} H_x &= U(z) e^{ik_0 \sin \theta y} \\ E_y &= -V(z) e^{ik_0 \sin \theta y} \end{aligned} \quad (\text{II-1-1})$$

for the P case and

$$\begin{aligned} E_x &= U(z) e^{ik_0 \sin \theta y} \\ H_y &= V(z) e^{ik_0 \sin \theta y} \end{aligned} \quad (\text{II-1-2})$$

for the S case. (We define the P case to be that in which the magnetic

field H points along the x-axis, and the S case to be that in which the E field points along x.)

Here the parameter k_0 is defined by

$$k_0 = \frac{2\pi}{\lambda} \quad (\text{II-1-3})$$

with λ the vacuum wavelength. θ is the vacuum angle of incidence to the normal. In most cases we will follow the usual optics convention where angles of incidence are specified to the normal.

The exponents in the y oscillation factors have been put in a trigonometric form that enables them to be fit to boundary conditions that are independent of x and that apply in planes of constant z, i.e. our solutions are appropriate to a Bragg geometry in which the y-z plane is the plane of incidence (See fig. II-1-1).

The P case is somewhat more interesting than the S case, and is discussed in somewhat less detail by Born and Wolf (1975, p.54). For this reason we will briefly describe the steps by which the solutions for the fields in P polarization are put into characteristic matrix form.

As is shown by Born and Wolf, the amplitudes U and V satisfy the ordinary differential equations

$$\frac{d^2 U}{dz^2} - \frac{d(\ln \epsilon(z))}{dz} \frac{dU}{dz} + k_0^2 (\epsilon(z) - \sin^2 \theta) U = 0 \quad (\text{II-1-4})$$

CHARACTERISTIC MATRIX ANALYSIS OF X-RAY STRUCTURES

U.S. 
N.E.

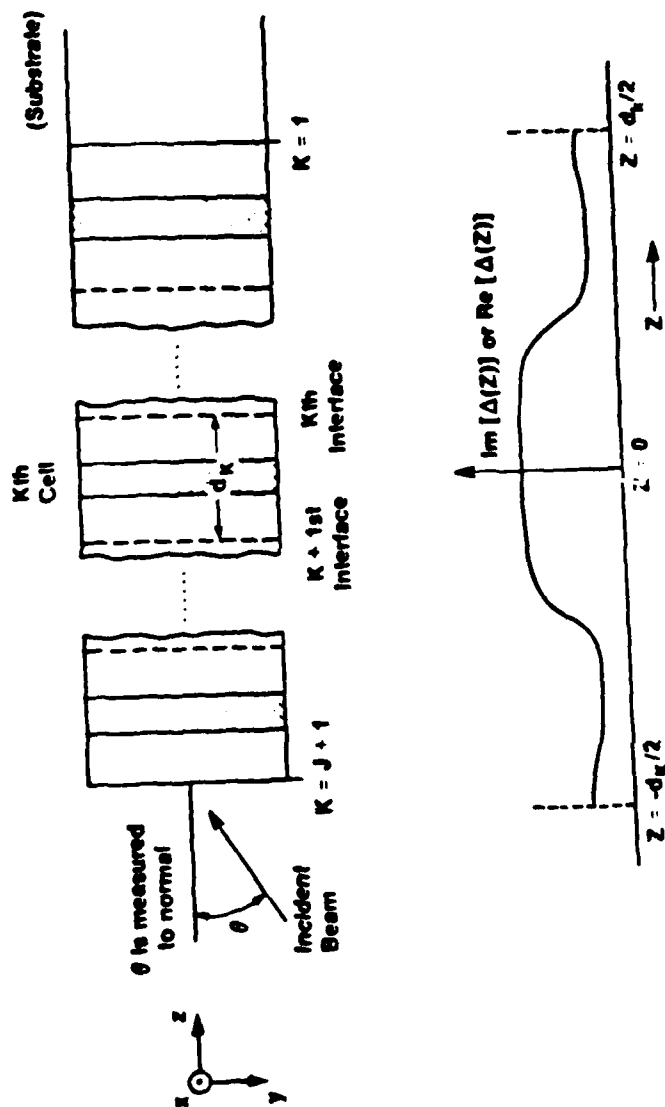


Figure 11-1-1

and

$$V = - \frac{i}{k_0 \epsilon(z)} \frac{dU}{dz} \quad (\text{II-1-5})$$

in the P case.

We consider next the unit cell of an x-ray multilayer reflector that extends from $z=z_1$ to $z=z_2$ (with $z_1 < z_2$). As indicated in fig. II-1-1 we will define the direction of increasing z to be towards the substrate from the incident side. Let $U_1(z), V_1(z); U_2(z), V_2(z)$ be two sets of solutions for the transverse fields H_x and E_y that satisfy

$$\begin{aligned} U_1(z_1) &= 0, & V_1(z_1) &= 1 \\ U_2(z_1) &= 1, & V_2(z_1) &= 0 \end{aligned} \quad (\text{II-1-6})$$

Then following well-known procedures for linear ordinary differential equations, we have the following unique relation connecting general fields at z_2 with those at z_1 :

$$\begin{pmatrix} -E_y(z_2) \\ H_x(z_2) \end{pmatrix} = \begin{pmatrix} V_1(z_2) & V_2(z_2) \\ U_1(z_2) & U_2(z_2) \end{pmatrix} \begin{pmatrix} -E_y(z_1) \\ H_x(z_1) \end{pmatrix} \quad (\text{II-1-7})$$

(The minus signs in the field vectors are a result of the definitions in eq. II-1-1). This linear relation obtains because eqs. II-1-4,5 are homogeneous.

The determinant of the above matrix must be one according to the same mathematical arguments as are used in the S case by Born and Wolf (1975, p.56). (Note that their supplemental physical arguments concerning conservation of energy cannot be applied in the case of an absorbing structure).

Since the determinant is unity we can write the following inverse to eq. II-1-7:

$$\begin{pmatrix} -E_y(z_1) \\ H_x(z_1) \end{pmatrix} = \begin{pmatrix} U_2(z_2) & -V_2(z_2) \\ -U_1(z_2) & V_1(z_2) \end{pmatrix} \begin{pmatrix} -E_y(z_2) \\ H_x(z_2) \end{pmatrix} \quad (\text{II-1-8})$$

or, in more usual form:

$$\begin{pmatrix} E_y(z_1) \\ H_x(z_1) \end{pmatrix} = \begin{pmatrix} U_2(z_2) & V_2(z_2) \\ U_1(z_2) & V_1(z_2) \end{pmatrix} \begin{pmatrix} E_y(z_2) \\ H_x(z_2) \end{pmatrix} \quad (\text{II-1-9})$$

This is what Born and Wolf call the characteristic matrix solution for the

fields in a stratified medium; in the case of a unit cell in an x-ray reflector it expresses the fields on the incident side of the cell in terms of those on the substrate side. In order to more conveniently treat reflection at non-normal angles of incidence we will refer to a slightly different matrix as the characteristic matrix (eq. II-1-14 below). In this way we will automatically incorporate in our equations certain well-known rules of thin-film optics that reduce the case of off-normal-incidence reflection to the normal incidence case (Baumeister, 1962).

We will subscript all quantities that appear on the right side of the characteristic matrix equation with the common subscript K . Thus the fields at the substrate interface of a particular cell in a multilayer will have the same subscripts as the structural parameters of the cell, while the subscripts of the fields at the incident interface will be larger by one.

Generally, we will use the indicial label K to refer to an arbitrary cell in a multilayer, and the label J to refer to the last or total number of cells. Thus, K is equal to 1 at the substrate and rises to $J+1$ at the upper interface (see fig. II-1-1). (Note that given the matrix inversion performed between eqs. II-1-7 and 8, we have chosen to have K increase in the direction of decreasing z .)

Eq. II-1-4 can easily be transformed into a Schrodinger equation by eliminating the dU/dz term. Since the Schrodinger equation can only be solved analytically in a few isolated cases (Williams, 1982), eq. II-1-4 cannot be solved analytically in the case of an arbitrary gradient.

However, in Appendix 1, we show how straightforward perturbation techniques can be used to solve eqs. II-1-4,5 under the assumption that the parameter Δ , defined by

$$\Delta(z) \equiv \frac{1}{2} (\epsilon(z) - 1) \quad (\text{II-1-10})$$

is small compared to one. Since Δ may be thought of as the unit decrement to the index of refraction, this perturbation solution is appropriate to the x-ray regime where the indices of refraction of all materials approach unity.

The cell structure is considered to be specified by the function $\Delta(z)$ in the range $z_1 \leq z \leq z_2$.

Without loss of generality we can position the $z=0$ origin at the midpoint of the cell. We then specify the cell thickness in terms of a dimensionless Bragg detuning parameter ϕ :

$$\begin{aligned} \phi &\equiv \pi \pi - k_0 \cos \theta (z_2 - z_1) & (\text{II-1-11}) \\ &= \pi \pi - k_0 \cos \theta d \end{aligned}$$

with d the cell thickness.

In eq. II-1-11, m is the order of diffraction. Under the approximations to which we will work (see below), a resonance in m th order may unambiguously be defined as the situation in which Φ is small.

A single unit cell can be treated with a perturbation approach because the interaction of the single cell with the incident x-ray beam must be weak.

We will generally be interested in multilayers operating sufficiently near resonance that the reflectivity of the total structure is significantly higher than the reflectivity of the individual cells. For this reason it will generally not be appropriate to treat the entire structure using a perturbation approach.

As an alternative, we could, of course, obtain the characteristic matrix solution for the entire structure by multiplying the matrix solutions for the individual cells together. This standard procedure is based on the continuity of the transverse field components across the cell interfaces. Such a procedure may be thought of as a numerical integration of eqs. II-1-4,5 with the thickness of each unit cell serving as the step size (thus the requirement that the change introduced by each unit cell be small).

Rather than multiplying the individual cell matrices together to find the overall solution, we will, instead, derive from the individual cell solution a difference equation that propagates the amplitude reflectivity from cell to cell. The known (and usually negligible) reflectivity of the substrate then serves as a boundary condition from which to determine the reflectivity of the entire structure.

The derivations of the matrix solution and difference equation are presented in Appendices 1 and 2; before presenting these results we will first characterize more precisely the approximations used.

In terms of our notation, the usual theories of x-ray diffraction generally include only first order terms in the decrement Δ and the detuning parameter Φ . Neglect of high orders in Δ is generally well justified in the x-ray regime.

Neglect of higher orders in Φ is justified when the structure is periodic and operating near resonance (near enough that the reflectivity of the overall structure is significantly higher than that of the individual cell).

This may be seen by the following argument. The number of cells participating in the reflection can be at most of order $1/\Delta$ due to extinction of the beam. Here Δ may be considered to be an average of the decrement over typical values for the cell. (If extinction were due only to absorption, we could consider only the imaginary part of Δ here, but at shorter wavelengths, depletion by back reflection is also significant.)

Success in obtaining high reflectivity will depend on the total phase detuning in the stack of participating cells; this detuning will be of order Φ/Δ since Φ is essentially the detuning per cell. For operation near resonance, the total detuning cannot be large compared to one radian, so that in cases of greatest interest, $\Phi/\Delta \leq 1$. Given that $\Delta \ll 1$, an expansion that is first order in Φ as well as in Δ is adequate.

Higher order terms are necessary to treat two kinds of aperiodicities.

The first are aperiodicities of a stochastic nature; in such cases a random error in ϕ at one point in the structure might be canceled out by that at another, so that larger RMS detunings within the individual cells can be tolerated than is possible in the periodic case. Specifically, since we would expect the total RMS phase error from the J cells that participate in the reflection to be of order $\sqrt{J} [\langle \phi^2 \rangle]^{1/2}$, which is of order $[\langle \phi^2 \rangle / \Delta]^{1/2}$, we would expect that in the cases of greatest interest:

$$\phi^2 \lesssim \Delta \quad (\text{II-1-12})$$

In fact, we will see in sec. II-5 that if the expectation value of ϕ is equal to its unperturbed value (i.e. its value in the periodic case), the lowest order effect of random errors in ϕ on the reflectivity is through terms of order ϕ^2 .

The second kind of multilayer structure whose performance is strongly dependent on higher order terms is that which results when in-situ reflectance monitoring is used. In such multilayers the ϕ value for the K th pair of layers is intended to be that value which maximizes the reflectivity R_{K+1} of the entire stack of cells 1 ... K (see sec. II-4).

Determination of this ϕ value amounts to setting a derivative of intensity reflectance with respect to ϕ_K equal to zero. We will see in sec. II-4 that the lowest order terms in such a derivative are of order Δ (i.e. Δ^1 rather than Δ^0). Terms of order unity are missing because

the lowest order effect of a change in φ_K having magnitude $\delta\varphi_K$ is to multiply the reflected amplitude by $\exp(-2i\delta\varphi_K)$ leaving the intensity reflectance unchanged. To obtain terms of order Δ in a differentiation with respect to φ , terms of order $\varphi \cdot \Delta$ must be included initially.

In order to treat both kinds of aperiodicity, our analysis will include all orders in the parameter φ , and also terms of order $\varphi \cdot \Delta$.

As in the traditional x-ray diffraction theories, we will include only first order terms in Δ . Such an approximation breaks down at grazing angles of incidence. As the angle approaches the surface the path traversed through each cell increases for two reasons; first because the x-ray photons traverse the cell at more oblique angles, and second because the cell thicknesses have to be increased as the angle decreases in order to maintain a resonant reflection from the multilayer. These two factors imply a quadratic increase in extinction per layer with angle; therefore when

$$\left(\frac{\pi}{2} - \theta\right)^2 \lesssim |\Delta| \quad (\text{II-1-13})$$

a regime has been reached in which the beam has a strong interaction within one single cell, and our formalism is no longer valid.

Our formalism will depart from the common practice in x-ray diffraction theory in that we will include the trigonometrical factors that are necessary for the theory to be applied near normal incidence.

II-1-14

In the remainder of the text we will follow the standard practice of using primes and double primes to denote real and imaginary parts, respectively.

Part C) Characteristic Matrix Solution for the X-Ray Regime

In Appendix 1 we show that subject to the approximations discussed above, the solution for the P polarization field amplitudes $U_{1,2}$, $V_{1,2}$ is

$$\begin{pmatrix} E_{k+1} \\ H_{k+1} \end{pmatrix} = \begin{pmatrix} (-1)^m \cos t_k - p_k & i(-1)^m \sin t_k + r_k \\ i(-1)^m \sin t_k - r_k & (-1)^m \cos t_k + p_k \end{pmatrix} \begin{pmatrix} E_k \\ H_k \end{pmatrix} \quad (\text{II-1-14})$$

where

$$r_k \equiv \frac{k_0 P(\theta)}{\cos \theta} \int_{\text{cell}} dz \Delta(z) \cos(2k_0 \cos \theta z)$$

$$p_k \equiv \frac{k_0 P(\theta)}{\cos \theta} \int_{\text{cell}} dz \Delta(z) \sin(2k_0 \cos \theta z) \quad t \equiv \phi_k - \mu_k$$

$$\mu_k \equiv \frac{k_0}{\cos \theta} \int_{\text{cell}} dz \Delta(z)$$

$$P(\theta) \equiv \begin{cases} \cos 2\theta & \text{P Polarization} \\ 1 & \text{S Polarization} \end{cases} \quad (\text{II-1-15})$$

Eq. II-1-14 represents a straightforward perturbation solution to eq. II-1-4; terms of order Δ^2 are neglected, and the vacuum (i.e. $\Delta = 0$) solution for U is substituted into all terms that are first order in Δ . Eq. II-1-4 then becomes a driven harmonic oscillator equation.

In eq. II-1-14, \mathcal{E} and \mathcal{H} are the field components that are normal to the k -vector in vacuum; from fig. II-1-2 we see that these are defined by

$$\begin{aligned}\mathcal{E} &= -E_y / \cos \theta \\ \mathcal{H} &= H_x\end{aligned}\tag{II-1-16}$$

(Again we note that θ is the vacuum angle of incidence). Thus if we follow the usual sign convention of thin-film optics in which the amplitude reflectivity ρ is real and positive if the reflected E_y is in phase with the incident E_y (for P polarization), we see from fig. II-1-2:

$$\begin{aligned}\mathcal{E} &= (1 + \rho) A \\ \mathcal{H} &= (1 - \rho) A\end{aligned}\tag{II-1-17}$$

where A is some K -dependent field amplitude.

We show in Appendix 1 that eq. II-1-14 is also valid for the case of S polarization (in which E is polarized along the x -axis) if we define

$$\mathcal{E} \equiv E_x\tag{II-1-18}$$

COORDINATE SYSTEM FOR CHARACTERISTIC MATRIX SOLUTION

UR
LLE

In all figures ρ is real and positive. Field vectors are shown as solid arrows, propagation directions as dotted arrows.

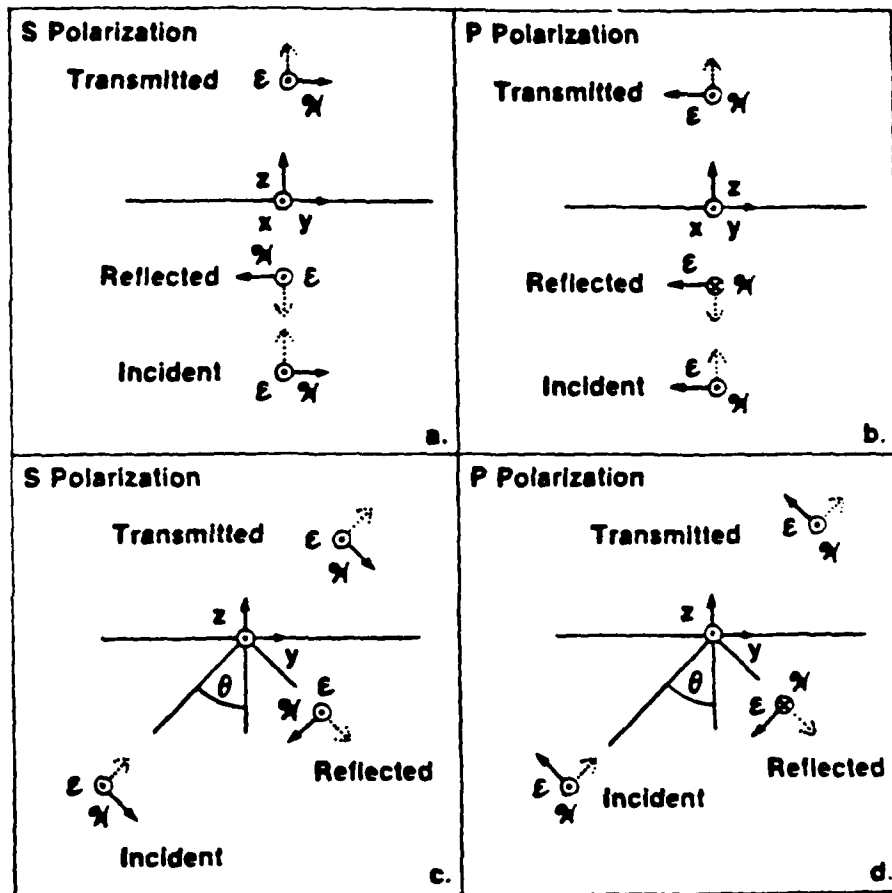
- Figure a shows S polarization at normal incidence.
- Figure b shows P polarization at normal incidence. The coordinate system of fig. a has been rotated 90° relative to the field vectors.
- Figure c shows S polarization at non-normal incidence.
- Figure d shows P polarization at non-normal incidence.

X348

Caption for
Figure II-1-2

COORDINATE SYSTEM FOR CHARACTERISTIC MATRIX SOLUTION

UPL
LLE



X347

Figure II-1-2

and

$$\mathcal{H} = H_y / \cos \theta \quad (\text{I-1-19})$$

Our use of a single matrix solution for both polarizations is analogous to the use of what Baumeister (1962) calls "effective" multilayer parameters; both amount to reduction procedures for simplifying off-normal incidence calculations.

Part D) Difference Equation for Amplitude Reflectance

As discussed in sec. II-1-B above, we choose to convert the matrix solution for the unit cell to a difference equation in ρ_k before proceeding to consider the reflectivity of the multilayer as a whole.

The derivation in Appendix 2 follows a well-known procedure, except that in the course of the derivation we make truncated expansions consistent with the approximations discussed in sec. II-1-B above.

In brief, eq. II-1-17 is substituted into eq. II-1-14, and the amplitude A is cancelled from the resulting pair of equations. Terms of order Δ^2 are then neglected.

The resulting equation that propagates the amplitude reflectivity ρ_k across the k th cell is:

$$\rho_{k+1} = e^{-2it_k} \rho_k + (-1)^m e^{-it_k} (ir_k - p_k) + (-1)^m e^{-it_k} (ir_k + p_k) \rho_k^2 \quad (\text{II-1-20})$$

Eq. II-1-20 is analogous to the well-known Airy recursion formula that is used to propagate the reflectivity from single-layer to single-layer in optical multilayers.

In fact, if we now employ a phenomenological Airy argument based on the usual summation of partial reflection and transmission components within the single-cell, we can physically interpret eq. II-1-20 by comparing it with the result of the Airy summation.

The Airy summation argument is summarized in fig. II-1-3; the phenomenological derivation of the partial reflection and transmission components has been omitted, but arguments that are essentially the same are

used in the Darwin-Prins theory of x-ray diffraction (see James, 1965, p.62). As shown in the figure, the first term on the right side of eq. II-1-20 represents a double transmission through cell K with an intermediate reflection from the stack of preceding cells K-1, K-2, ... 1. The second term represents a reflection from cell K back into the direction of the incident medium. The third term represents a multiple reflection process consisting of reflection from the preceding stack of cells, reflection back towards the substrate from cell K, and finally a second reflection from the preceding stack back into the direction of the incident medium. Higher order multiple reflections are of order Δ^2 and are neglected.

The comparison thus implies (as can be shown rigorously from the matrix solution of eq. II-1-14) that the reflectance of the Kth cell is $(-1)^m (i r_K - p_K) e^{-i t_K}$ from the incident side and $(-1)^m (i r_K + p_K) e^{-i t_K}$ from the substrate side, and that the transmittance of the cell is $-e^{-i t_K}$.

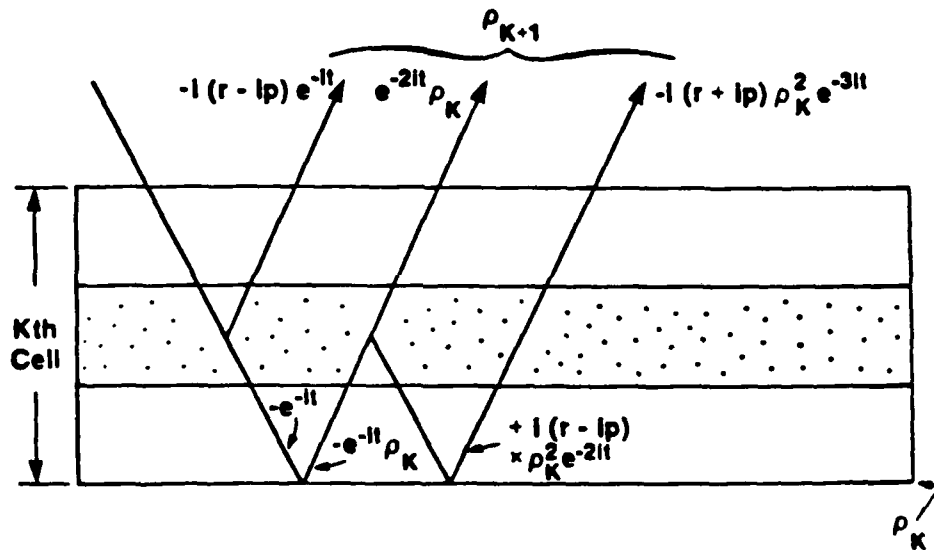
The analogy between eq. II-1-20 and the single-layer Airy formula can be formalized in another way if the cell is centrosymmetric, i.e. if it contains a central plane of symmetry. In this case the method of equivalent parameters can be employed (Herpin 1947, Knittl 1976). If the cell is centrosymmetric, the parameter p defined in eq. II-1-15 is zero, and eq. II-1-14 becomes, to first order in φ and Δ

$$\begin{pmatrix} \mathcal{E}_{K+1} \\ \mathcal{M}_{K+1} \end{pmatrix} = \begin{pmatrix} -1 & -i(t_K - r_K) \\ -i(t_K + r_K) & -1 \end{pmatrix} \begin{pmatrix} \mathcal{E}_K \\ \mathcal{M}_K \end{pmatrix}$$

(II-1-21)

PROPAGATION EQUATION FOR AMPLITUDE REFLECTANCE

UR
LLE



The amplitude recursion equation is:

$$\rho_{K+1} = e^{-2lt} \rho_K - (lr - lp) e^{-lt} - (lr + lp) e^{-3lt} \rho_K^2$$

X320

Figure 11-1-3

in the simplest case where $m=1$. If this matrix equation is compared to the usual (non x-ray) characteristic matrix solution for single homogeneous layers (Born and Wolf, 1975, p.58) with $\theta = 0$:

$$\begin{pmatrix} \mathcal{E}_{k+1} \\ \mathcal{H}_{k+1} \end{pmatrix} = \begin{pmatrix} \cos \beta_e & -\frac{i}{n_e} \sin \beta_e \\ -i n_e \sin \beta_e & \cos \beta_e \end{pmatrix} \begin{pmatrix} \mathcal{E}_k \\ \mathcal{H}_k \end{pmatrix} \quad (\text{II-1-22})$$

we see that the two matrices can be formally equated if we make the identifications

$$\begin{aligned} \beta_e &\equiv \pi + \delta \\ \delta &\equiv \sqrt{t^2 - r^2} \\ n_e &\equiv \sqrt{\frac{t+r}{t-r}} \end{aligned} \quad (\text{II-1-23})$$

n_e and β_e are known as the equivalent parameters of the unit cell. (n_e is the equivalent index and β_e the equivalent phase thickness of the cell). There is a straightforward analogy between the unit cell of an x-ray reflector and a single homogeneous layer that has an index of refraction

n_e and a phase thickness β_e . Similarly, a reflector with J cells corresponds to a stack of J equivalent layers, which is, in effect, a single layer having index n_e and phase thickness $J \beta_e$. This coalescence of the J equivalent layers into one is permissible because the internal equivalent layers have no interaction with one another (since their refractive indices are equal). The equivalent parameters can therefore be considered to incorporate implicitly the effect of multiple reflections within the structure.

Eq. II-1-20 is also analogous to the propagation equation that Rogelnik derives (1976) from standard coupled wave equations. This may be seen by setting

$$\begin{aligned} p_{K+1} - p_K &\approx \frac{dp}{dK} \cdot \Delta K + O\left(\frac{d^2 p}{dK^2}\right) \\ &= \frac{dp}{dK} + O\left(\frac{d^2 p}{dK^2}\right) \end{aligned} \quad (\text{II-1-24})$$

so as to obtain the differential equation

$$\frac{dp}{dK} = -2itp - (ir - p) - (ir + p)p^2 + O(\Delta^2) + O(\varphi \cdot \Delta) + O(\varphi^2) \quad (\text{II-1-25})$$

where we have indicated that the neglected term of order $\frac{d^2 \rho}{d K^2}$ is also of order φ^2 , $\varphi \cdot \Delta$, and Δ^2 . In treating stochastic problems, a difference equation has the important advantage over differential equations of having terms whose statistical properties can be determined quite easily; this is because the terms of the difference equation have a one-to-one correspondence with the properties of the individual cells.

Since the layer thicknesses are proportional to the order of diffraction m , the absorption is least in first order (for given wavelength and angle), and the first order reflectivity is therefore the largest.

Thus, although our formalism includes all orders of diffraction, our discussion will generally involve only the first order case.

Section II-2 - Defect-Free Multilayers

Part A) Reflectivity of Periodic Multilayers

The simplest case that can be treated with the formalism developed in the previous section is that of a perfectly periodic multilayer reflector. Periodic x-ray multilayers have been treated by several authors in recent years (Vinogradov and Zeldovich 1977, Lee 1981, and Underwood and Barbee 1981). Periodic x-ray multilayers are quite analogous in their diffracting properties to crystals cut in the Bragg geometry.

We will present brief derivations of the reflecting properties of periodic x-ray multilayers; the derivations will tend to be quite sketchy except where previous work has been extended.

As discussed in sec. II-1-B, periodic multilayers can be treated with an analysis that is first order in φ and Δ . Eq. II-1-20 becomes

$$\rho_{k+1} = \rho_k - 2it_k \rho_k - (ir_k - p_k) - (ir_k + p_k) \rho_k^2 \quad (\text{II-2-1})$$

The reflectivity of the periodic multilayer increases almost monotonically as more unit cells are added, until a steady-state regime is reached. In the steady-state regime, we can set

$$\rho_{k+1} = \rho_k = \rho \quad (\text{II-2-2})$$

so that eq. II-2-1 becomes a quadratic equation to be solved for q . The two solutions are

$$q = - \frac{s+t}{r-ip} \quad (\text{II-2-3})$$

where two roots result from the sign ambiguity in the quantity

$$s = \pm \sqrt{t^2 - r^2 - p^2} \quad (\text{II-2-4})$$

We now discuss the sign choice that must be made here. The sign choice that we establish will be applicable in most of the remaining calculations of the text. The few exceptions will be explicitly identified.

The parameter s has already appeared in eq. II-1-23; in eq. II-2-4 we make the ambiguity in sign explicit, and generalize the definition to include the non-centrosymmetric case.

In order for the equivalent phase parameter to imply exponential attenuation instead of exponential amplification, we must choose that root in eq. II-1-23 which causes the imaginary part of s to be positive. In the remainder of the text, the square roots that occur in expressions of the

form $\sqrt{a^2 - b^2}$ will by definition be chosen to be on the branch corresponding to positive imaginary parts.

We will now show that under this convention it is the upper sign rather than the lower sign that must be used in eq II-2-4 as well as in eq. II-1-23.

If we multiply the two possible solutions together (i.e. the two solutions corresponding to different evaluations of the sign ambiguity in eq. II-2-4), we find

$$\rho_1 \cdot \rho_2 = \left(\frac{\pm \sqrt{t^2 - r^2 - p^2} - t}{r - ip} \right) \cdot \left(\frac{\mp \sqrt{t^2 - r^2 - p^2} - t}{r - ip} \right) = \frac{r + ip}{r - ip} \quad (\text{II-2-5})$$

so that if we represent the true physical solution with an unsubscripted ρ :

$$\rho^2 = \left(\frac{\pm \delta - t}{r - ip} \right)^2 = \left(\frac{\pm \delta - t}{r - ip} \right) \left(\frac{r + ip}{r - ip} \cdot \frac{r - ip}{\mp \delta - t} \right) = - \frac{\delta + t}{\delta - t} \cdot \frac{r + ip}{r - ip} \quad (\text{II-2-6})$$

or

$$R^2 = |\rho^2|^2 = \frac{1 + \frac{2 \operatorname{Re}(t/\delta)}{1 + |t/\delta|^2}}{1 - \frac{2 \operatorname{Re}(t/\delta)}{1 + |t/\delta|^2}} \quad (\text{II-2-7})$$

In order to have $R < 1$, we require

$$\operatorname{Re} \left(\frac{t}{s} \right) = \frac{1}{|s|^2} \operatorname{Re} (ts^*) < 0 \quad (\text{II-2-8})$$

We will show later in this section that at the wavelength of peak reflectivity,

$$s = \pm id \quad (\text{II-2-9})$$

with $d > 0$ and with the upper and lower sign in eq. II-2-9 representing the same sign ambiguity as in eq. II-2-4.

Thus, from eq. II-1-15, we require at peak reflectivity

$$\mp \mu'' d < 0 \quad (\text{II-2-10})$$

for $R < 1$, with μ'' defined to be the imaginary part of the parameter μ (defined in eq. II-1-15).

II-2-5

Since all materials absorb in the x-ray regime, $\mu'' > 0$, so that in eqs. II-2-4,10 we must choose the upper sign when the multilayer operates at the Bragg condition.

Further, we will show later in this section that the imaginary part of δ can never change sign from its value at the Bragg condition. Therefore, we will always choose the root in the definition of δ to be the root with the positive imaginary part.

In this case we have

$$\rho = - \frac{\delta + t}{r - ip} = \frac{r + ip}{\delta - t} \quad (\text{II-2-11})$$

and also the useful result

$$\rho^2 = - \frac{r + ip}{r - ip} \frac{\delta + t}{\delta - t} \quad (\text{II-2-12})$$

(This is eq. II-2-6 with the ambiguity in the sign of δ now resolved).

In Appendix 3 we solve eq. II-2-1 in the case of periodic multilayers that do not contain sufficiently many layer pairs to reach the steady-state regime. The solution (integration of eq. II-1-25 with constant coefficients) is

$$\rho_J = \frac{\rho_\infty (1 - e^{2i\delta(J-1)})}{1 - \rho_\infty^2 \left(\frac{r-ip}{r+ip} \right) e^{2i\delta(J-1)}} \quad (\text{II-2-13})$$

where ρ_∞ is the steady-state reflectivity given by eq. II-2-11. When the multilayer is centrosymmetric (as in the bilayer case of fig. II-2-1),

$$\rho_J = \frac{\rho_\infty (1 - e^{2i\delta(J-1)})}{1 - \rho_\infty^2 e^{2i\delta(J-1)}} \quad (\text{II-2-14})$$

The resemblance of eq. II-2-14 to an Airy summation is readily understood in terms of the equivalent index analogy (sec. II-1-D).

The most important centrosymmetric case is that of the bilayer structure shown in fig. II-2-1. This figure incorporates the ideal assumptions of perfectly sharp interfaces. Under this assumption the structural parameters defined in eq. II-1-15 become

$$\begin{aligned} \rho_k &= 0 \\ r_k &= (\Delta_H - \Delta_L) \sin \beta_{H,k} \sec^2 \theta \\ \mu_k &= \pi \Delta_L + \beta_{H,k} (\Delta_H - \Delta_L) \sec^2 \theta \\ \rho_{H,k} &= k_0 \cos \theta d_{H,k} \end{aligned} \quad (\text{II-2-15})$$

STRUCTURE OF UNIT CELL IN A BILAYER REFLECTOR

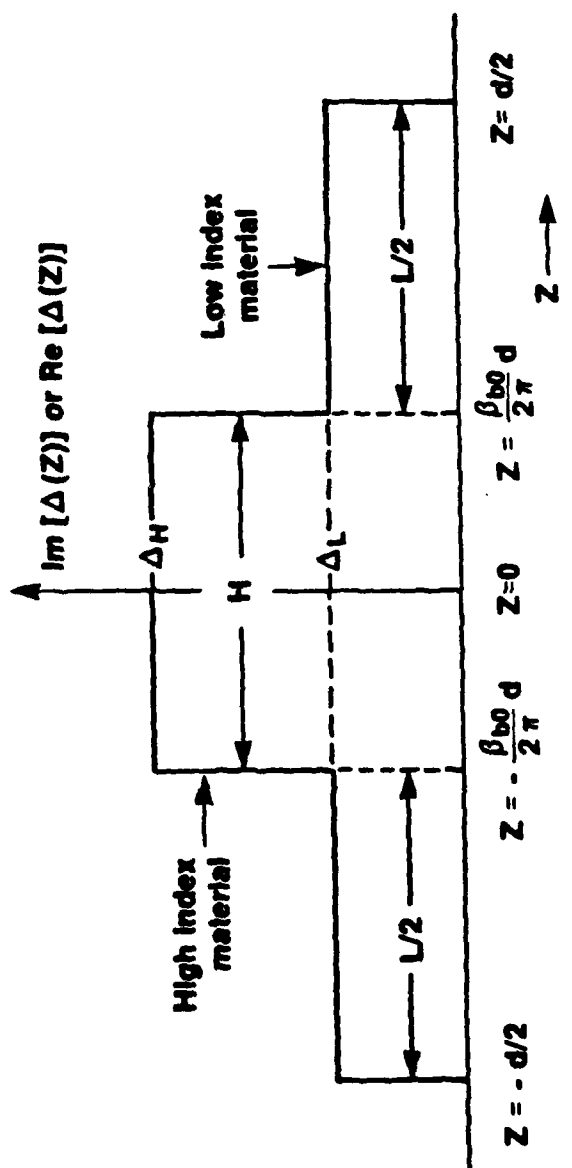


Figure 11-2-1

X203

The parameter $\beta_{H,K}$, the phase thickness of the high index layer, will be used so often that we will establish a convention in which the subscript H is made implicit. The symbol β_K will thus by definition be the phase thickness of the Kth high index layer.

The high index layer will be by definition that layer with the larger absorption; generally the real part of the decrement of the high index layer will also be larger in magnitude than the real decrement of the low index layer.

Part B) Structural Optimization of Periodic Multilayers

We now turn from the calculation of reflectivity to the associated optimization problem, i.e. the problem of determining the particular structure that optimizes the performance of a multilayer. Here we will mostly be concerned with maximizing the peak reflectivity of the structure. This would be particularly appropriate in such applications as the design of cavity mirrors for potential x-ray lasers; in other applications one might ultimately prefer more complicated criteria.

The reflectivity of a multilayer mirror operating near resonance can for practical purposes always be considered to be an increasing function of the number of layer pairs in the structure; thus in order to maximize the reflectivity one would want to deposit sufficiently many layer pairs that the multilayer operates in the steady-state regime. (In some cases the reflectivity is found to undergo very small oscillations about the steady-state reflectivity as the number of layer pairs approaches the regime where radiation no longer reaches the substrate).

Further, in many applications polarization effects can be neglected. This includes applications at normal incidence (x-ray laser mirrors, normal-incidence microscopy), grazing incidence applications (all high-energy applications), reflections taking place near 45 degrees (where the P reflectivity is zero), and most of the applications that involve synchrotron radiation (which is linearly polarized).

In such cases we maximize the reflectivity by maximizing the magnitude squared of eq. II-2-11.

We first consider the problem of choosing the optimum unit cell thickness for the multilayer, which from eq. II-1-11 is equivalent to finding an optimum value for the parameter ϕ .

The well-known requirement for maximizing the reflectivity of a dielectric multilayer (i.e. a multilayer with real $\Delta(z)$), is that the unit cell thickness be chosen in accordance with Bragg's law, as corrected for dispersion. By this criterion the optical thickness of the unit cell should be one half-wavelength, so that

$$\int_{\text{Period}} dz \operatorname{Re} (1 + \Delta(z)) \cos \theta(z) = \frac{\lambda}{2} \quad (\text{II-2-16})$$

Here $\theta(z)$ is the angle of refraction at a particular depth in the structure; this is defined by

$$(1 + \Delta(z)) \sin \theta(z) = \sin \theta \quad (\text{II-2-17})$$

Then

$$\int_{\text{Period}} dz (1 + \Delta'(z)) \cos \theta(z) = \int_{\text{Period}} dz \sqrt{1 + 2\Delta'(z) - \sin^2 \theta} \approx \int_{\text{Period}} dz \left(\cos \theta + \frac{\Delta'(z)}{\cos \theta} \right) \quad (\text{II-2-18})$$

so

$$\frac{\lambda}{2} = d \cos \theta + \int_{\text{Period}} dz \frac{\Delta'(z)}{\cos \theta} \quad (\text{II-2-19})$$

or from eq. II-1-11:

$$\varphi_{\text{optimum}} = \pi - \frac{2\pi d \cos \theta}{\lambda} = \frac{2\pi}{\lambda \cos \theta} \int_{\text{Period}} dz \Delta'(z) = \mu' \quad (\text{II-2-20})$$

This x-ray version of the dispersion-corrected Bragg's law does not correctly produce the position of maximum reflectivity in the case where Δ is complex. The appropriate condition in this case was first found in the

context of diffraction from centrosymmetric crystals by Miller (1935).

We will briefly present a simpler derivation that applies in the non-centrosymmetric case as well, and that provides physical insight into the origin of the absorption correction to Bragg's law.

Since $R = \rho \cdot \rho^*$, we can say that if

$$2 \cdot \text{Re} \left(\frac{1}{\rho} \frac{d\rho}{dv} \right) = \frac{1}{\rho} \frac{d\rho^*}{dv} + \frac{1}{\rho^*} \frac{d\rho}{dv} = \frac{1}{R} \cdot \frac{dR}{dv} = 0 \quad (\text{II-2-21})$$

where v is some structural parameter of the multilayer, then the reflectivity is maximized with respect to v . In this section we will use a dot to represent d/dv .

In the present case we optimize with respect to the parameter φ , so that $\dot{t} = 1$ to first order in φ according to eq. II-1-15. (As discussed above, in the case of periodic multilayers we need only work to within first order in the parameter φ , and can neglect terms of order $\varphi \cdot \Delta$.)

Also,

$$\dot{\gamma} = \dot{\rho} = \dot{\mu} = 0 + O(\varphi \cdot \Delta) \quad (\text{II-2-22})$$

II-2-13

so that

$$\dot{s} = \frac{t}{s} \quad (\text{II-2-23})$$

and

$$\dot{\rho} = - \frac{1 + \frac{t}{s}}{r - ip} = \frac{\rho}{s} \quad (\text{II-2-24})$$

Since

$$\operatorname{Re} \left(\frac{1}{s} \right) = \frac{\operatorname{Re}(s^*)}{|s|^2} = \frac{\operatorname{Re}(s)}{|s|^2} \quad (\text{II-2-25})$$

our condition for maximizing R is that

$$\operatorname{Re}(s) = 0 \quad (\text{II-2-26})$$

If we compare eq. II-1-23 with eq. II-2-26, we see that our correction to Bragg's law is a requirement that the real part of the equivalent phase thickness of the cell be π . The difference here from the usual requirement that the real part of the optical phase thickness be π is due to the presence of multiple reflections.

This may be seen by manipulating eq. II-2-11 to obtain

$$\delta = -t - \rho(r - ip) \quad (\text{II-2-27})$$

so that

$$\begin{aligned} e^{i\beta_0} &\cong -e^{i\delta} \cong -e^{-it} (1 - i\rho(r - ip)) \\ &\cong -e^{-it} + \rho(ir + p) \end{aligned} \quad (\text{II-2-28})$$

to within order Δ .

The term $-e^{-it}$ represents the phase oscillation involved in transmission through the cell. The term $+\rho(ir + p)$ also contributes to the overall phase oscillation across the cell (which is $e^{i\beta_0}$); this term represents a multiple reflection process consisting of transmission through the cell, reflection from all succeeding cells, and reflection back into the initial direction. (Higher-order multiple reflections are of order Δ^2). A phase change occurs during the multiple reflections, and if n is complex, the overall

oscillation of the field across the cell is shifted.

For brevity's sake we have described the calculation of this effect as a correction for absorption; however we note that the imaginary part of Δ causes a shift in the position of peak reflectivity through its effect on the phase of ρ , rather than by any extinction mechanism (see below).

We can convert the resonance condition of eq. II-2-26 to a computationally more useful form as follows. The requirement that $\text{Re}(\delta) = 0$ can only be satisfied if δ^2 is a negative real number. We show in Appendix 4 that when φ is chosen to make δ^2 real, δ^2 is automatically made negative. This implies a result stated above, that the imaginary part of δ can never change sign from its sign at the Bragg condition. Such a sign change would require the existence of a φ value at which δ^2 was both real and positive.

For $\text{Im}(\delta^2)$ to be zero, we must have from eq. II-2-4

$$t't'' = r'r'' + p'p'' \quad (\text{II-2-29})$$

or

$$\varphi_{\text{opt}} = \mu' - \frac{r'r'' + p'p''}{\mu''} \quad (\text{II-2-30})$$

To first order in Δ , we can evaluate eq. II-1-15 (the defining equations for the parameters in our solution for φ_{opt}) at $\theta_B \equiv \arccos(\lambda/2d)$.

In terms of a wavelength or θ -spacing shift away from the uncorrected Bragg value defined by $2d \cos \theta_B = \lambda$, we can set

$$\varphi_{opt} = \pi \frac{\Delta \lambda}{\lambda} = -\pi \frac{\Delta d}{d} \quad (\text{II-2-31})$$

To convert the phase shift to an angular shift, we have from eq. II-1-11

$$\varphi_{opt} = - \frac{\pi \Delta (\cos \theta)}{\cos \theta_B} \quad (\text{II-2-32})$$

where

$$\theta_B \equiv \arccos(\lambda/2d) \quad (\text{II-2-33})$$

We can set

$$\frac{\Delta(\cos \theta)}{\cos \theta_B} = \frac{-\Delta \theta \sin \theta_B - \frac{\Delta \theta^2}{2} \cos \theta_B}{\cos \theta_B} \quad (\text{II-2-34})$$

Terms of order $\Delta\theta^2 \cos \theta_0$ have been included in eq. II-2-34 because the linear term becomes very small near normal incidence.

Solving for $\Delta\theta$ gives

$$\Delta\theta = \sqrt{\tan^2 \theta_0 + \frac{2\varphi_{opt}}{\pi}} - \tan \theta_0 \quad (\text{II-2-35})$$

which has physical solutions so long as the radicand is non-negative, or, to a good approximation, so long as $\theta_0 \gg \sqrt{\frac{2|\varphi_{opt}|}{\pi}}$. At $\theta_0 = \sqrt{\frac{2|\varphi_{opt}|}{\pi}}$, the true angle of maximum reflectivity θ is at 0° .

Away from the normal incidence regime (i.e. $\theta_0 \gg \sqrt{\frac{2|\varphi_{opt}|}{\pi}}$),

$$\Delta\theta = \frac{\varphi_{opt}}{\pi \tan \theta_0} = \frac{\mu'}{\pi \tan \theta_0} - \frac{r'r'' + p'p''}{\mu'' \pi \tan \theta_0} \quad (\text{II-2-36})$$

In eq. II-2-36 the first term on the right is the dispersion correction and the second is the absorption correction.

We show in Appendix 5 that the absorption correction must always be smaller than the dispersion correction except in regions of very strong anomalous dispersion, but there are many cases in which the two are comparable in magnitude.

In fig. II-2-2 we show plotted the ratio of absorption correction to net correction in a particular example; specifically, the ratio plotted is

$$\frac{\theta_2 - \theta_1}{\theta_s - \theta_1} \quad (\text{II-2-37})$$

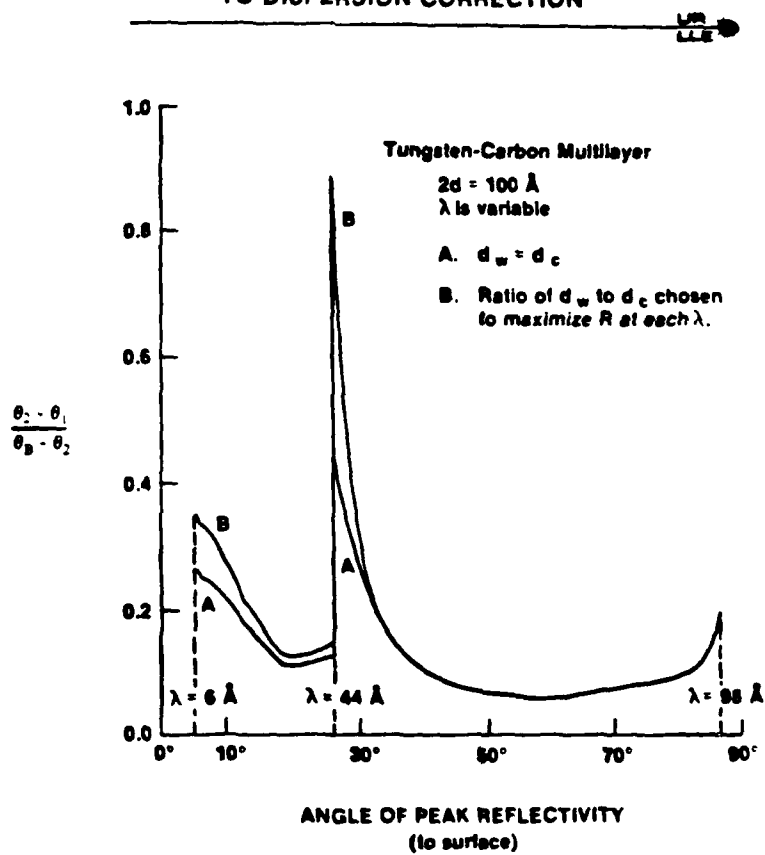
with θ_2 the true Bragg angle as corrected for both absorption and dispersion, and θ_1 the Bragg angle as corrected by eq. II-2-20 for dispersion only. This example exhibits the commonest case in which the absorption and dispersion corrections are in opposite directions. (Note that in this figure the incidence angle is measured relative to the surface.)

Fig. II-2-2 shows three regimes in which the relative effect of absorption is fairly large.

First, near normal incidence, eq. II-1-11 shows that the correspondence between angular shifts and shifts in phase thickness becomes strongly non-linear due to the cosine factor. In the normal incidence regime, a relatively small absorption correction to the phase thickness can therefore cause a large decrease in the total angular shift. Both the angular absorption correction and the angular dispersion correction become large in absolute terms as the angle of incidence approaches 0° .

The plot shows two other regions at which the relative importance of the absorption correction becomes strong; at wavelengths just above the carbon-K edge, and at short wavelengths. In each case the absorption correction becomes strong because multiple reflections become strong, and multiple reflections are strong precisely where the absorption imposes a

COMPARISON OF ABSORPTION CORRECTION
TO DISPERSION CORRECTION



2360

Figure II-2-2

weaker limit on the reflectivity. (In a moment we will consider the limiting case where the absorption goes to zero).

This is why the term "absorption correction" must not be taken too literally; as discussed above, the imaginary part of Δ shifts the resonance angle through the mechanism of phase changes that occur during multiple reflections, rather than by any mechanism involving extinction of the fields.

In the limit of zero absorption, the steady-state reflectivity of the structure approaches unity throughout the high reflectance zone (often called the stop-band). According to the above analysis, in the limit of low absorption the reflectivity approaches closest to one at an angle quite far from the center of the stop-band, because with low absorption multiple reflections become quite strong, which in turn causes the ratio defined in eq. II-2-37 to become quite large. However with very low absorption the reflectivity at θ_1 departs only slightly further from unity than the reflectivity at θ_2 , and indeed the reflectivity throughout the stopband is almost constant.

In contrast, in the soft x-ray regime where absorption is fairly substantial, peak reflectivities generally do not approach very close to one and the absorption correction manifests itself as a distinct shift in the position of peak reflectivity (see fig. II-2-3).

REFLECTANCE OF W/C MULTILAYER - UNPOLARIZED LIGHT

UVR
LLE

$d_W = 7.79 \text{ \AA}$ $d_C = 28.57 \text{ \AA}$
 Number of layer pairs = 1000
 Wavelength = 67.60 \AA
 Order of diffraction is 1

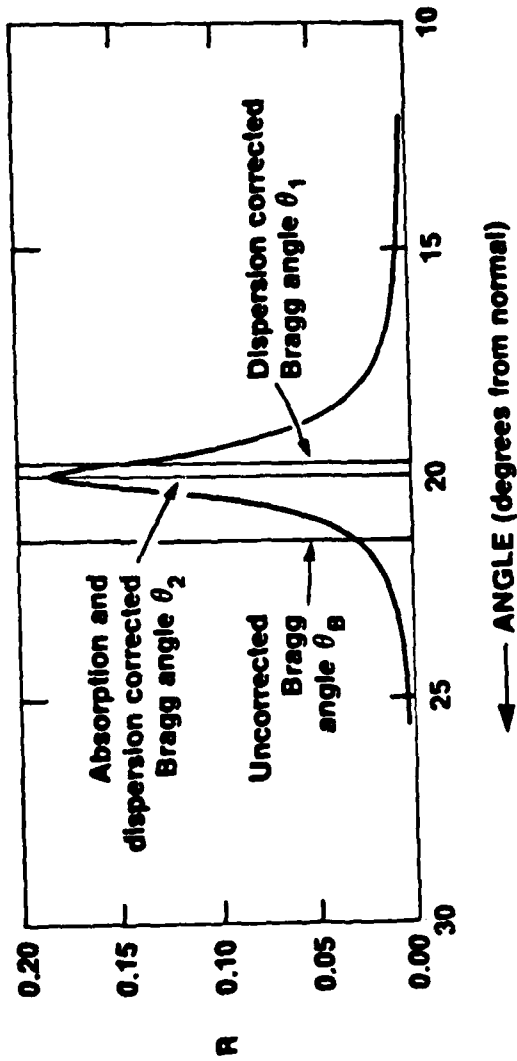


Figure II-2-3

X344

Once the cell thickness of the structure is chosen so as to optimize the reflectivity, one may wish to optimize the structure in other degrees of freedom; for example in the usual case of a bilayer reflector one would like to optimize the ratio in thickness of the two types of layers.

In order to maximize the reflectivity at the Bragg angle, (which we will refer to as maximization of peak reflectivity), we use the steady-state version of eq. II-2-1

$$-2it\rho - (ir-p) - (ir+p)\rho^2 = 0 \quad (\text{II-2-38})$$

Dividing by ρ and differentiating with respect to some secondary structural parameter (any parameter other than ϕ) we obtain

$$2i + (\dot{r} - ip)\rho + (\dot{r} + ip)\frac{1}{\rho} + (r - ip)\dot{\rho} - (r + ip)\frac{\dot{\rho}}{\rho^2} = 0 \quad (\text{II-2-39})$$

From eq. II-2-11 we have

$$(\gamma - i\rho)\dot{e} - (\gamma + i\rho)\frac{\dot{e}}{\rho^2} = \frac{\dot{e}}{\rho} (-(s+t) - (s-t)) = -2s\frac{\dot{e}}{\rho} \quad (\text{II-2-40})$$

To maximize the peak reflectivity we require that $\text{Re}(\frac{\dot{e}}{\rho})=0$; further, since we are operating at peak reflectivity, s is pure imaginary, so that $\text{Im}(2s\frac{\dot{e}}{\rho})=0$.

Thus if we take the imaginary part of eq. II-2-39 we obtain, using eq. II-2-11, the condition for maximizing the peak reflectivity

$$\text{Im} \left[2\dot{t} - \frac{\dot{\gamma} - i\dot{\rho}}{\gamma - i\rho} (s+t) + \frac{\dot{\gamma} + i\dot{\rho}}{\gamma + i\rho} (s-t) \right] = 0 \quad (\text{II-2-41})$$

If, as in the case of a bilayer reflector, the cell is centrosymmetric in such a way that \dot{p} is zero along with p , eq. II-2-41 achieves the simple form:

$$\text{Im} \left[\dot{t} - t \frac{\dot{\gamma}}{\gamma} \right] = 0 \quad (\text{II-2-42})$$

We now consider optimization with respect to the parameter β used in characterizing a bilayer reflector (eq. II-2-15). The terms of eq. II-2-41 are of order Δ , so that to obtain optimization accurate overall to first order in Δ , we need only differentiate with respect to β in "zeroth" order for our optimization.

For the same reason, we can consider optimization of β to yield an optimum ratio of high-index layer thickness to low-index layer thickness given by

$$g \equiv \frac{\beta}{\pi - \beta} = \frac{k_0 \cos \theta d_H}{k_0 \cos \theta_B (d_H + d_L) - k_0 \cos \theta d_H} \cong \frac{d_H}{d_L} \quad (\text{II-2-43})$$

Upon carrying out the differentiation in eq. II-2-42 we obtain the optimization condition first obtained by Vinogradov and Zeldovich (1977)

$$\tan \beta_{opt} = \beta_{opt} + \frac{\pi \Delta_L''}{\Delta_H'' - \Delta_L''} \quad (\text{II-2-44})$$

Eq. II-2-44 is valid for either polarization at any angle of incidence.

We mention that one should avoid being misled by the discussion following eq. 23b in Vinogradov and Zeldovich (1977), which might suggest that eq. II-2-44 can be treated as a primary optimization condition. Eq. II-2-44 is a secondary optimization condition that obtains only if the total cell thickness has also been optimized.

Eq. II-2-44 is a transcendental equation with no analytic solution, but in Appendix 6 we exhibit a fast numerical procedure that can be used to solve it. The initial analytic seed that is used in this procedure may well be accurate enough for most purposes.

In Appendix 7 we show that the peak reflectivity (i.e. the relectivity at the Bragg condition) is given by:

$$R_{\text{peak}} = \left[2\mu''^2 + r'^2 + p'^2 - r''^2 - p''^2 \right. \\ \left. - 2 \sqrt{\mu''^4 - (r'r'' + p'p'')^2 + \mu''^2(r'^2 + p'^2 - r''^2 - p''^2)} \right] \\ \times \left[|r|^2 + |p|^2 + 2(r'p'' - r''p') \right]^{-1}$$

(II-2-45)

Part C) Optimum Materials Choices

Eq. II-2-45 in conjunction with the fast algorithm of Appendix 6 makes it possible to very rapidly calculate the maximum reflectivity obtainable from a given pair of materials reflecting at a particular x-ray wavelength.

It therefore becomes possible to have a computer program search efficiently through all possible pairs of multilayer materials and so determine the optimum reflectivity attainable at the particular wavelength under consideration.

Fig. II-2-4 and table II-2-1 show the results of such a materials search at each of 125 wavelengths in the soft x-ray region from 6.2Å to 124Å. Δ_H and Δ_L were calculated using atomic scattering factors compiled by Henke et al. (1982).

The calculated reflectivities of the optimum materials pairs are shown plotted in red. For comparison, fig. II-2-5 shows the reflectivity obtainable from the usual materials choice of tungsten and carbon. The reflectivity of the new materials combinations are surprisingly high, particularly at the longer wavelengths. In general the high reflectivities are a consequence of atomic resonances; the anomalous dispersion in the spectral vicinities of such resonances cause layers made with the elements to yield high reflectivities, primarily because their unit decrements have anomalously small imaginary parts.

Fig. II-2-4 also shows plotted in green the optimum fraction of the unit cell thickness that should be occupied by the high index layer.

Figure II-2-4 (color illustration) is bound
at the back of the text.

Optimum X-Ray Multilayer Parameters

MINIMUM 2 ALLOWED IS 5

WAVE- LENGTH	R	N	GAMMA	ELEMENT - H	ELEMENT - L
		(AT) (NORMAL) (INCIDENCE)	(DH) (-----) (DH + DL)		
124.00	.8447	9.9	.3568	RHODIUM	SILICON
121.04	.7932	15.4	.3627	RHODIUM	STRONTIUM
118.15	.7992	15.8	.3785	RHODIUM	STRONTIUM
115.33	.7897	16.8	.3850	RHODIUM	STRONTIUM
112.58	.7758	18.0	.3862	RHODIUM	STRONTIUM
109.89	.7667	19.1	.3869	RHODIUM	STRONTIUM
107.27	.7505	19.9	.3785	RUTHENIUM	STRONTIUM
104.71	.7392	20.9	.3800	RUTHENIUM	STRONTIUM
102.21	.7280	21.9	.3814	RUTHENIUM	STRONTIUM
99.77	.7171	23.0	.3829	RUTHENIUM	STRONTIUM
97.39	.7165	23.6	.3899	SILVER	STRONTIUM
95.06	.7176	24.8	.4049	SILVER	STRONTIUM
92.79	.6966	26.4	.4099	SILVER	STRONTIUM
90.58	.6693	27.7	.4205	SILVER	STRONTIUM
88.42	.6313	29.1	.4344	SILVER	STRONTIUM
86.31	.6218	42.6	.3573	RUTHENIUM	BORON
84.25	.6210	45.4	.3503	RUTHENIUM	BORON
82.23	.6201	48.2	.3456	RUTHENIUM	BORON
80.27	.6208	51.3	.3388	RUTHENIUM	BORON
78.36	.6239	54.5	.3320	RUTHENIUM	BORON
76.49	.6287	57.7	.3261	RUTHENIUM	BORON
74.66	.6341	60.9	.3204	RUTHENIUM	BORON
72.88	.6414	63.8	.3148	RUTHENIUM	BORON
71.14	.6504	66.2	.3100	RUTHENIUM	BORON
69.44	.6774	79.9	.3797	LANTHUNUM	BORON
67.78	.7211	75.3	.3905	LANTHUNUM	BORON
66.16	.8200	52.4	.4033	LANTHUNUM	BORON
64.59	.5446	99.7	.4933	CALCIUM	LANTHUNUM
63.04	.5097	108.6	.4924	LANTHUNUM	CALCIUM
61.54	.4932	73.8	.3703	RUTHENIUM	CALCIUM
60.07	.4879	78.6	.3668	RUTHENIUM	CALCIUM
58.64	.4827	83.6	.3634	RUTHENIUM	CALCIUM
57.24	.4778	89.0	.3598	RUTHENIUM	CALCIUM
55.87	.4732	94.8	.3563	RUTHENIUM	CALCIUM
54.54	.4676	101.4	.3521	RUTHENIUM	CALCIUM
53.23	.4687	161.0	.3011	RUTHENIUM	CARBON
51.96	.4707	172.1	.2958	RUTHENIUM	CARBON
50.72	.4797	155.5	.2204	COBALT	CARBON
49.51	.4943	176.9	.2623	CHROMIUM	CARBON
48.33	.5109	183.2	.2610	CHROMIUM	CARBON
47.18	.5291	188.5	.2596	CHROMIUM	CARBON

Table II-2-1

II-2-29

MINIMUM 2 ALLOWED IS 5

WAVE- LENGTH	R	W	GAMMA	ELEMENT - R	ELEMENT - L
		(AT) (NORMAL) (INCIDENCE)	(DE) (-----) (DE + DL)		
46.05	.5530	191.5	.2581	CHROMIUM	CARBON
44.95	.5830	189.3	.2568	CHROMIUM	CARBON
43.88	.6625	158.3	.2556	CHROMIUM	CARBON
42.83	.4987	157.2	.3122	CHROMIUM	CALCIUM
41.81	.5072	163.9	.3126	CHROMIUM	CALCIUM
40.81	.5159	170.6	.3129	CHROMIUM	CALCIUM
39.84	.5256	177.5	.3134	CHROMIUM	CALCIUM
38.89	.5358	183.8	.3137	CHROMIUM	CALCIUM
37.96	.5489	188.9	.3141	CHROMIUM	CALCIUM
37.05	.5663	191.6	.3145	CHROMIUM	CALCIUM
36.17	.5924	188.9	.3149	CHROMIUM	CALCIUM
35.30	.4174	164.9	.3257	COBALT	SCANDIUM
34.46	.4302	171.0	.3260	COBALT	SCANDIUM
33.64	.4458	176.3	.3263	COBALT	SCANDIUM
32.84	.4645	180.1	.3267	COBALT	SCANDIUM
32.05	.4904	180.2	.3271	COBALT	SCANDIUM
31.29	.5392	198.7	.3790	CHROMIUM	SCANDIUM
30.54	.3595	181.5	.3653	NICKEL	BARIUM
29.81	.3708	198.1	.3596	NICKEL	TITANIUM
29.10	.3969	200.5	.3599	NICKEL	TITANIUM
28.41	.5022	144.4	.4967	CHROMIUM	CADMIUM
27.73	.5053	184.3	.3745	COBALT	TITANIUM
27.07	.3960	274.1	.3485	NICKEL	MAGNESIUM
26.42	.4058	291.0	.3473	NICKEL	MAGNESIUM
25.79	.4153	308.9	.3462	NICKEL	MAGNESIUM
25.17	.4254	328.1	.3451	NICKEL	MAGNESIUM
24.57	.4750	209.3	.3992	NICKEL	VANADIUM
23.99	.4443	370.2	.3429	NICKEL	MAGNESIUM
23.41	.4537	393.6	.3418	NICKEL	MAGNESIUM
22.85	.4625	418.3	.3409	NICKEL	MAGNESIUM
22.31	.4978	216.3	.4319	NICKEL	TELLURIUM
21.78	.7359	250.8	.4003	TELLURIUM	MAGNESIUM
21.26	.4885	504.9	.3377	NICKEL	MAGNESIUM
20.75	.5824	522.0	.4019	CHROMIUM	MAGNESIUM
20.25	.5038	575.0	.3356	NICKEL	MAGNESIUM
19.77	.5109	614.5	.3346	NICKEL	MAGNESIUM
19.30	.5173	657.9	.3336	NICKEL	MAGNESIUM
18.84	.5236	707.6	.3322	NICKEL	MAGNESIUM
18.39	.5291	761.8	.3308	NICKEL	MAGNESIUM
17.95	.5321	820.4	.3302	NICKEL	MAGNESIUM
17.52	.6007	800.3	.3609	IRON	MAGNESIUM
17.10	.5338	969.6	.3286	NICKEL	MAGNESIUM
16.69	.5320	1061.5	.3276	NICKEL	MAGNESIUM
16.30	.5295	1126.9	.3140	COPPER	MAGNESIUM
15.91	.6136	1244.9	.3971	BARIUM	MAGNESIUM
15.53	.5446	986.2	.1821	RHENIUM	MAGNESIUM
15.16	.5549	1046.9	.1807	RHENIUM	MAGNESIUM
14.79	.5648	1111.2	.1795	RHENIUM	MAGNESIUM
14.44	.5743	1179.1	.1782	RHENIUM	MAGNESIUM
14.10	.5839	1251.4	.1770	RHENIUM	MAGNESIUM
13.76	.5935	1328.6	.1757	RHENIUM	MAGNESIUM
13.43	.6027	1410.4	.1745	RHENIUM	MAGNESIUM
13.11	.6117	1496.3	.1734	RHENIUM	MAGNESIUM
12.80	.6208	1587.6	.1722	RHENIUM	MAGNESIUM

Table II-2-1
(continued)

II-2-30

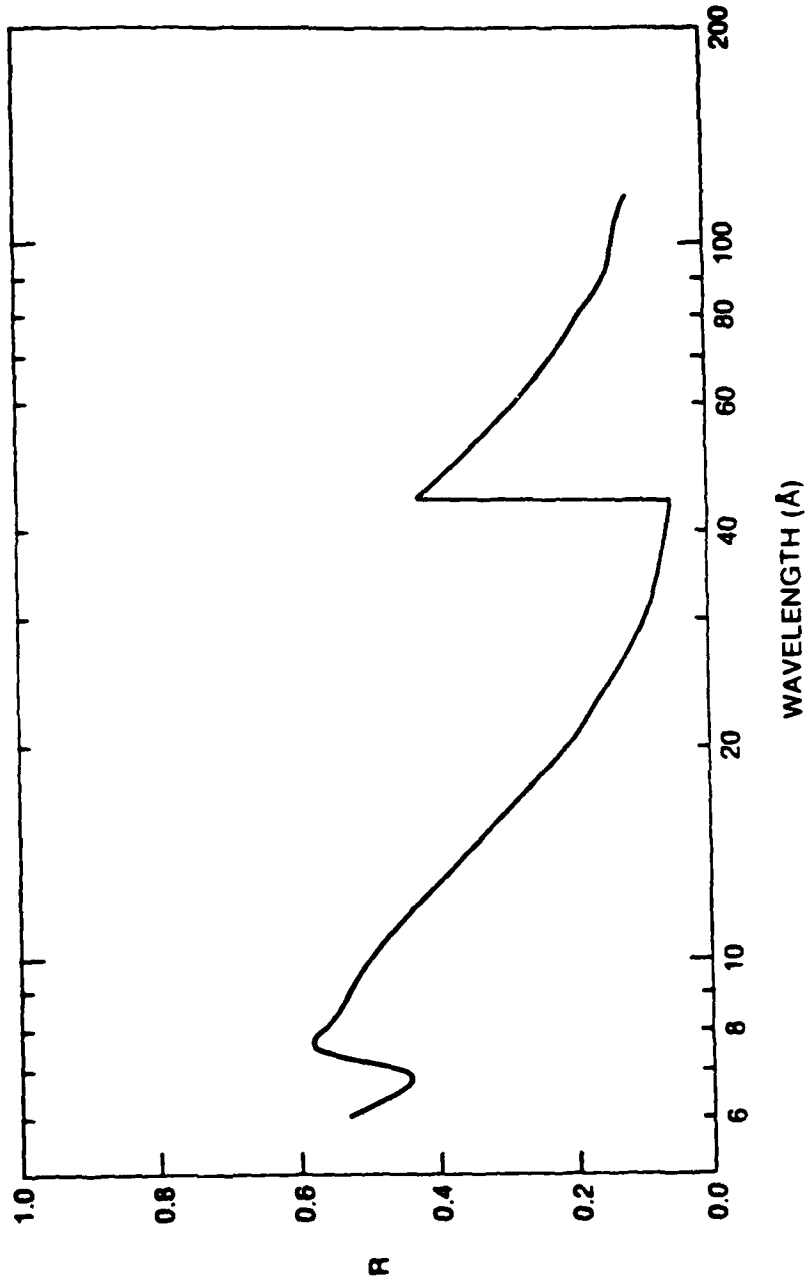
MINIMUM Z ALLOWED IS 5

WAVE- LENGTH	R	N (AT) (NORMAL) (INCIDENCE)	GAMMA (DE) (-----) (DE + DL)	ELEMENT - H	ELEMENT - L
12.49	.6298	1685.1	.1711	RHENIUM	MAGNESIUM
12.19	.6386	1787.5	.1700	RHENIUM	MAGNESIUM
11.90	.6475	1895.0	.1690	RHENIUM	MAGNESIUM
11.62	.6565	2010.0	.1680	RHENIUM	MAGNESIUM
11.34	.6650	2132.0	.1671	RHENIUM	MAGNESIUM
11.07	.6731	2260.9	.1661	RHENIUM	MAGNESIUM
10.81	.6816	2398.4	.1651	RHENIUM	MAGNESIUM
10.55	.6896	2543.6	.1642	RHENIUM	MAGNESIUM
10.30	.6978	2695.9	.1632	RHENIUM	MAGNESIUM
10.05	.7059	2854.0	.1623	RHENIUM	MAGNESIUM
9.81	.7148	3008.6	.1614	RHENIUM	MAGNESIUM
9.58	.7652	5512.9	.4435	BORON	MAGNESIUM
9.35	.6502	2747.2	.1900	RHENIUM	BORON
9.13	.6581	2932.2	.1888	RHENIUM	BORON
8.91	.6659	3134.8	.1875	RHENIUM	BORON
8.70	.6733	3352.0	.1863	RHENIUM	BORON
8.49	.6802	3584.7	.1852	RHENIUM	BORON
8.29	.6869	3840.5	.1840	RHENIUM	BORON
8.09	.6941	3472.8	.1934	RHENIUM	ALUMINUM
7.89	.6991	4427.4	.1815	RHENIUM	BORON
7.71	.7077	4862.6	.2011	RUTHENIUM	BORON
7.52	.7166	5156.5	.2003	RUTHENIUM	BORON
7.34	.7252	5469.1	.1996	RUTHENIUM	BORON
7.17	.7338	5802.7	.1988	RUTHENIUM	BORON
7.00	.7420	6157.1	.1981	RUTHENIUM	BORON
6.83	.7500	6535.3	.1973	RUTHENIUM	BORON
6.67	.7578	6941.6	.1965	RUTHENIUM	BORON
6.51	.7652	7374.8	.1958	RUTHENIUM	BORON
6.35	.7724	7836.9	.1950	RUTHENIUM	BORON
6.20	.7795	8327.8	.1943	RUTHENIUM	BORON

Table II-2-1
(Continued)

REFLECTIVITY ATTAINABLE FROM TUNGSTEN-
CARBON MULTILAYERS

U.S.  L.I.E.



X343

Figure II-2-5

Adjacent pairs of dotted lines in the figure demarcate the regions in which some one pair of materials has proved to be optimum; atomic resonances cause the curves to be highly discontinuous across these lines. Fig. II-2-4 shows plotted in blue the bench-mark value N that the number of layer pairs J should exceed in order to approach the steady-state regime. N is calculated at normal incidence; the number of layer pairs required scales as $\cos^2 \theta$ for fixed λ (see sec. II-3). In order to have the layers remain of practical thickness (say at least a few Angstroms), it is desirable to go to reflection angles away from normal incidence if the wavelength falls below about 30\AA . Even for wavelengths as long as 50\AA , we would expect the reflectivities to be degraded significantly from the displayed values at angles near normal incidence (see chapter III).

There are of course many other qualifications to be made about the results of this optimization study. The optical constants are presumably less reliable in the regions of strong anomalous dispersion that commonly occur in the elemental selections of table II-2-1; this is particularly true in the case of elements that are somewhat esoteric. In fact, optimization searches such as this will tend automatically to have a statistical bias in favor of erroneous data points in which the error happens to result in a higher calculated performance.

Further, no effort was made to assess the individual suitability or joint compatibility of the chosen materials in terms of either layer or interfacial quality and stability; even freedom from chemical reactivity was not considered. The only requirements on the elements examined were that they be non-radioactive and have melting points greater than 270°C (that of

bismuth). In addition beryllium was excluded for its toxicity; unlike other toxic elements, beryllium would have been frequently selected by the search program had it been included, due to its low atomic number.

However, most of the materials selections in table II-2-1 seem at least to be fairly reasonable, with the exception of two fairly common selections for the low index layers, calcium and strontium, which might be difficult to fabricate in thin high quality layers of the kind required in x-ray multilayers (Spiller 1982a).

In summary, the results of this materials search should be treated as suggestive until the materials selections can actually be tried. For this reason most of the text will deal with the more common materials choice of tungsten and carbon.

We have also carried out a multilayer materials search using a modified optimization program that seeks to maximize integrated reflectivity (or collection solid angle), rather than peak reflectivity. In the revised program we have modified the output routines in order to have printed out a number of possible materials pairs for each wavelength.

An abbreviated tabulation of these new results is given in Appendix 16.

Section II-3 - Scaling of Multilayer Reflection Properties

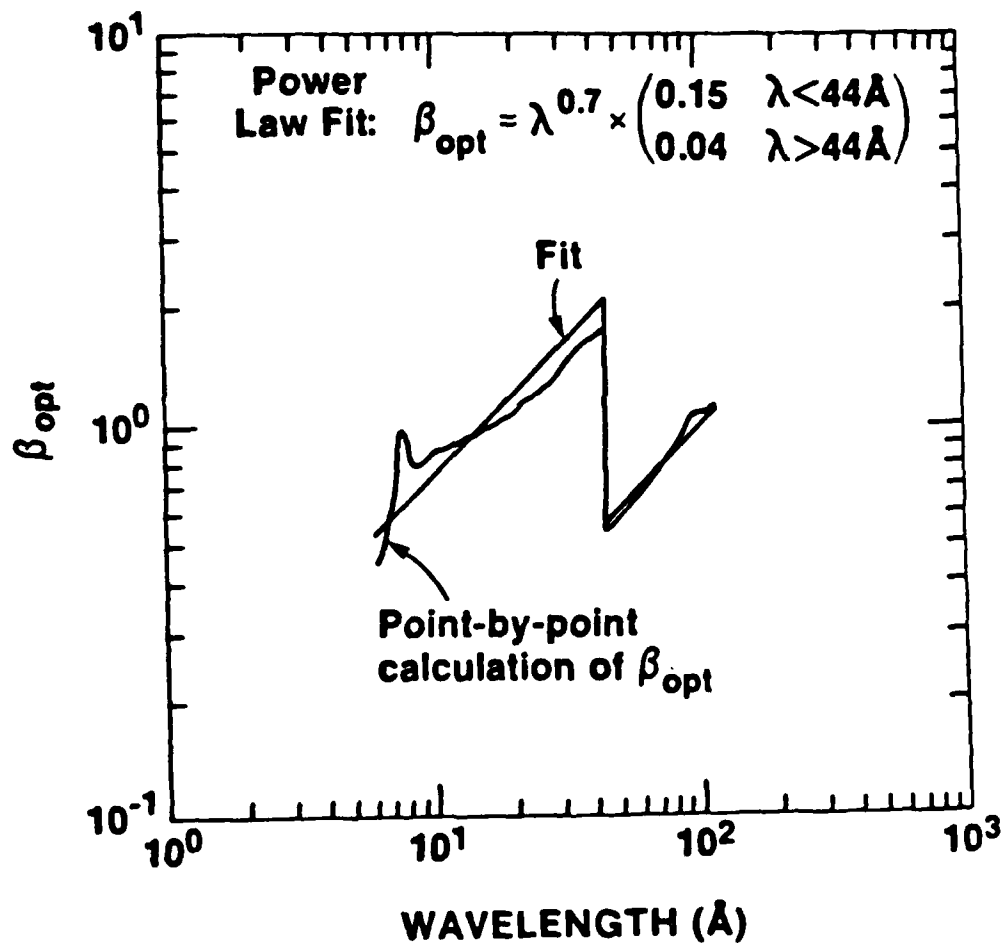
In this section we consider the approximate angular and spectral scaling of the reflection properties of tungsten-carbon multilayers. Our intention will be to determine simple dependencies that will be accurate to within a factor of two or so throughout the soft x-ray region.

Fig. II-2-5 shows the maximum reflectivity attainable from tungsten and carbon as a function of wavelength. The results are for S polarization; in the case of P polarization the reflectivity of an individual unit cell, and so, approximately, the reflectivity of the entire structure, is reduced by a factor $\cos^2 2\theta$ (see eqs. II-1-15 and II-3-1).

Fig. II-3-1 shows the β values used to obtain the reflectivities in fig. II-2-5. (Fig II-3-1 is essentially a plot of the solution to eq. II-2-44 based on the data in (Henke, et al. 1982)). The optimum thicknesses of the high index tungsten layers become small in regions of low absorption, i.e. β is small at short wavelengths and at wavelengths just above the carbon-K edge. In fact, Spiller (1976) has shown that, in principle, unit reflectivities can be obtained in the limit of no absorption in the low index layers (but with finite absorption in the high index material) if the high index layers are made infinitely thin.

SCALING OF OPTIMUM THICKNESS RATIO PARAMETER (Tungsten-Carbon Multilayer)

UR
LLE



X346

Figure 11-3-1

The reflectivity of the tungsten-carbon combination is usually fairly small. When the reflectivity is small, the fourth term on the right-hand side of eq. II-2-1 is small because it represents the effect of multiple reflections. When eq. II-2-1 is linearized by neglecting this term, it has the steady-state solution: $\rho \approx -\tau/2t$, or

$$R = \frac{|\tau|^2}{4((\phi - \mu')^2 + \mu''^2)} \quad (\text{II-3-1})$$

This Lorentzian intensity profile was first found by Henke (1982a). If we neglect the ρ_∞^2 term in the denominator of our solution for multilayer reflectivity outside the steady-state regime (eq. II-2-14), we obtain another result of Henke's (1982b):

$$\rho_{j+1} = \rho_\infty (1 - e^{-2is(j-1)}) \quad (\text{II-3-2})$$

From these approximate expressions we can derive simplified formulas for multilayer properties, whose wavelength and angular scaling is then relatively easy to determine.

For example from eq. II-3-1 we see that the FWHM of the reflection profile in radian units is approximately

$$\Delta\phi_{\text{FWHM}} \approx 2\mu'' \quad (\text{II-3-3})$$

II-3-4

Also, according to eq. II-3-2 the number of layer pairs N required for eq. II-2-14 to approach the Darwin-Prins limit of eq. II-2-11 is approximately $(S'')^{-1}$. Further, since eq. II-3-2 applies under the condition that ρ_∞ is small, from eq. II-3-1 we see that the parameter r can be considered to be small compared to the parameter t , to the extent that eq. II-3-1 is applicable. In that case, the number of layer pairs N required in the multilayers is given approximately by

$$N \approx \left[\text{Im} \sqrt{(\varphi - \mu)^2 - \tau^2} \right]^{-1} \\ \approx 1/\mu'' \quad (\text{II-3-4})$$

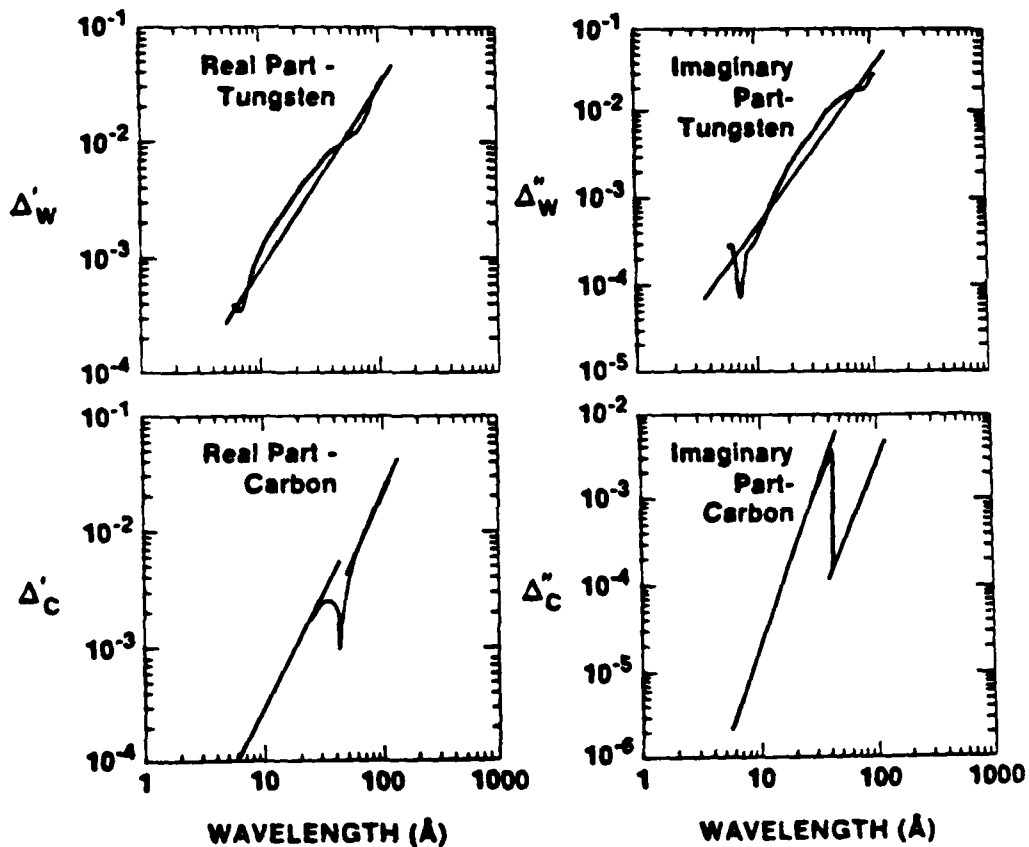
We can determine the approximate wavelength scaling of the optical constants of tungsten and carbon from the semilog plots of figs. II-3-2, which are based on a preliminary version of the data in (Henke, et al. 1982).

We find

$$\begin{aligned} (6\text{\AA} < \lambda < 114\text{\AA}) \quad \Delta_w &\approx ([2.7 \times 10^{-5}] \lambda_{(\text{\AA})}^{1.5}) + i([6.6 \times 10^{-6}] \lambda_{(\text{\AA})}^{1.85}) \\ (6\text{\AA} < \lambda < 44\text{\AA}) \quad \Delta_c &\approx ([2.8 \times 10^{-6}] \lambda_{(\text{\AA})}^2) + i([2.0 \times 10^{-7}] \lambda_{(\text{\AA})}^4) \\ (44\text{\AA} < \lambda < 114\text{\AA}) \quad \Delta_c &\approx ([6.1 \times 10^{-7}] \lambda_{(\text{\AA})}^{3.15}) + i([4.0 \times 10^{-10}] \lambda_{(\text{\AA})}^{3.4}) \end{aligned}$$

(II-3-5)

WAVELENGTH SCALING OF UNIT DECREMENT - TUNGSTEN AND CARBON



$\rho_C = 2.0 \text{ gm/cm}^3$
 $\rho_W = 15.0 \text{ gm/cm}^3$

Results are from a preliminary version of a compilation
 by Henke (1982a).

The first quantity dependent on these indices that we will consider is the optimum thickness ratio β . Since $\text{Im}(\Delta_c)$ tends to be small compared to $\text{Im}(\Delta_w)$, we can consider β_{opt} to be less than or of order unity, and to a rough approximation, can set

$$\tan \beta_{opt} \approx \beta_{opt} + \frac{\beta_{opt}^3}{3} \quad (\text{II-3-6})$$

Eq. II-2-44 then becomes for a tungsten-carbon multilayer:

$$\frac{\pi \Delta_c''}{\Delta_w'' - \Delta_c''} = \tan \beta_{opt} - \beta_{opt} \approx \frac{\beta_{opt}^3}{3} \quad (\text{I-3-7})$$

Then

$$\beta_{opt} = \sqrt[3]{\frac{3\pi \Delta_c''}{\Delta_w'' - \Delta_c''}} \quad (\text{I-3-8})$$

and for $\lambda < 44\text{\AA}$, we have from eq. II-3-5

$$\beta_{opt} \approx \sqrt[3]{\frac{2.86 \times 10^{-3} \lambda^{2.1}}{1 - 3 \times 10^{-4} \lambda^{2.1}}} \quad (\text{II-3-9})$$

II-3-7

Now, to a fair approximation, we can set the λ that occurs in the denominator of eq. II-3-9 equal to an "average" wavelength within the range of validity of the equation. If we use as an average the geometric mean of the range extrema, $\bar{\lambda} = \sqrt{6 \cdot 44} = 15\text{\AA}$, we have from eq. II-3-9

$$\beta_{opt} \approx 0.15 \lambda^{0.7} \quad (\text{II-3-10})$$

In a similar way, we find that for $\lambda > 44\text{\AA}$:

$$\beta_{opt} \approx 0.09 \lambda^{0.5} \quad (\text{II-3-11})$$

However, it turns out that because of the approximations made in arriving at the $\lambda > 44\text{\AA}$ result, it is more accurate to renormalize the exponent in this scaling law to correspond to the exponent of the short wavelength scaling law of eq. II-3-10; this equalization of exponents also has the advantage of leading to a simpler result.

Using $\bar{\lambda} = \sqrt{44 \cdot 114} = 70\text{\AA}$,

$$\beta_{opt} = 0.09 \lambda^{0.7} (\bar{\lambda})^{-0.2} = 0.04 \lambda^{0.7} \quad (\text{II-3-12})$$

Thus, our overall result for the range $6\text{\AA} < \lambda < 114\text{\AA}$ is

$$\beta_{opt} \approx \lambda^{0.7} \times \begin{bmatrix} 0.15 & (\lambda < 44\text{\AA}) \\ 0.04 & (\lambda > 44\text{\AA}) \end{bmatrix} \quad (\text{II-3-13})$$

This power-law fit is plotted in fig. II-3-1. As the figure shows, the dependence of β_{opt} on λ is not very strong. For many purposes, it is sufficiently accurate to take $\beta_{opt} \approx 1$.

With this approximation, we now consider the approximate scaling of the multilayer resolution and required number of layer pairs N . We first consider the dependence of these two quantities on d -spacing.

If we take $\beta_{opt} = 1$, we have from eq. II-2-15

$$\begin{aligned}\mu' &= [\pi \Delta_c'' + 1 \cdot (\Delta_w'' - \Delta_c'')] \cdot \sec^2 \theta \\ &\approx \Delta_w'' \sec^2 \theta \approx 6.6 \times 10^{-6} \lambda^{1.85} \sec^2 \theta\end{aligned}\quad (\text{II-3-14})$$

Taking $\bar{\lambda} = \sqrt{6 \cdot 114} = 30\text{\AA}$, we can, to a fairly good approximation, set

$$\begin{aligned}\mu' &\approx 6.6 \times 10^{-6} \lambda^2 (\bar{\lambda}^{-0.85}) \sec^2 \theta \\ &= 4.0 \times 10^{-6} \lambda^2 \sec^2 \theta\end{aligned}\quad (\text{II-3-15})$$

We note that eq. II-3-15 essentially states that the spatially averaged imaginary part of the index of refraction scales as λ^2 . Thus, the well-known scaling law for the hard x-ray regime, which states that the absorption coefficient $\kappa = \frac{4\pi\Delta''}{\lambda}$ scales as λ^3 , is not applicable in the soft x-ray regime. The results in (Henke, et al., 1982) indicate that the imaginary parts of the refractive indices of most materials scale very roughly as λ^2 in the soft x-ray regime.

Now if we denote the FWHM resolution of the multilayer in phase units as $\delta\phi_{FWHM}$, we have after incorporating the approximately quadratic wavelength scaling into eq II-3-3

$$\delta\phi_{FWHM} \cong 2\mu'' = 8.0 \times 10^{-6} \lambda^2 \sec^2 \theta = 8.0 \times 10^{-6} (2d_{(\text{\AA})})^2 \quad (\text{II-3-16})$$

Since

$$d\phi = \frac{2\pi d \cos \theta}{\lambda^2} d\lambda = \pi \frac{d\lambda}{\lambda} \quad (\text{II-3-17})$$

we have that the spectral resolution scales as

$$\frac{\delta\lambda_{FWHM}}{\lambda} = \frac{\delta\phi_{FWHM}}{\pi} = 2.5 \times 10^{-6} (2d_{(\text{\AA})})^2 \quad (\text{II-3-18})$$

From eq. II-3-4, the number of layer pairs N required to achieve maximum reflectivity is given by

$$N \cong (\mu'')^{-1} \cong \frac{2.5 \times 10^5}{(2d_{(\text{\AA})})^2} \quad (\text{II-3-19})$$

Thus, $\delta\lambda/\lambda$ and N are approximately independent of λ and θ for a given d . In general, properties of multilayer reflection tend to depend more strongly on the spacing d than on λ or θ .

We now consider the scaling of the angular resolution $\delta\theta_{FWHM}$ whose relation to $\delta\varphi_{FWHM}$ is

$$\delta\varphi_{FWHM} = \frac{2\pi d}{\lambda} \sin\theta \delta\theta_{FWHM} \quad (\text{II-3-20})$$

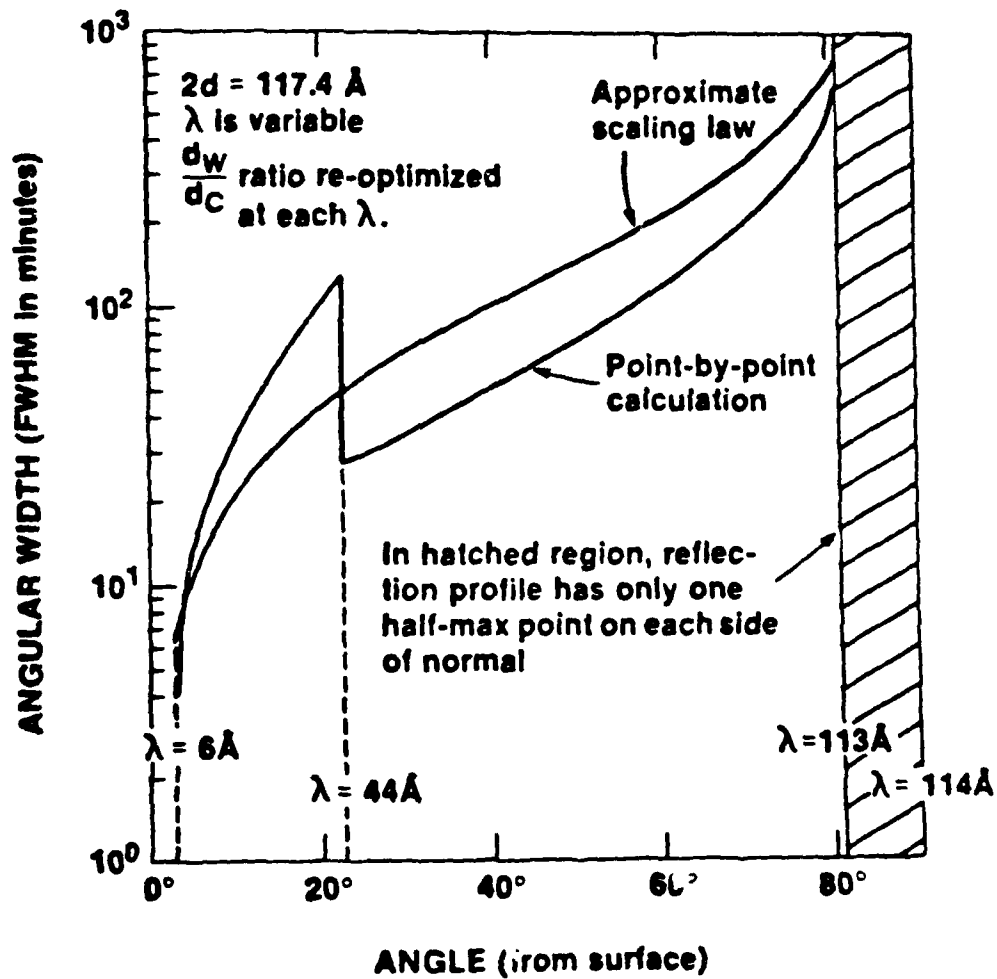
If $\beta_{opt} \approx 1$, we can use eq. II-3-16

$$\delta\theta_{FWHM} \approx 2.5 \times 10^{-6} \frac{(2d_{(\text{\AA})})^2}{\tan\theta} \quad (\text{in radians}) \quad (\text{II-3-21})$$

In crystallographic terminology, $\delta\theta_{FWHM}$ is essentially a rocking-curve width, and the scaling of rocking curve width with θ given by eq. II-3-21 is similar to the dependence one would expect to find in crystals. (Compare, for example, fig. 13 in (Burek, 1976) with fig. II-3-3 of this work. The point-by-point calculation in fig. II-3-3 is a numerical solution for the angular FWHM of the magnitude squared of eq. II-2-11.)

ANGULAR WIDTH OF REFLECTION PROFILE VERSUS ANGLE OF INCIDENCE (Tungsten-Carbon Multilayer)

UR
LLE



X349

Figure 11-3-3

AD-A136 306

DEVELOPMENT OF X-RAY LASER MEDIA MEASUREMENT OF GAIN
AND DEVELOPMENT OF C..(U) ROCHESTER UNIV N Y LAB FOR
LASER ENERGETICS J FORSYTH FEB 83

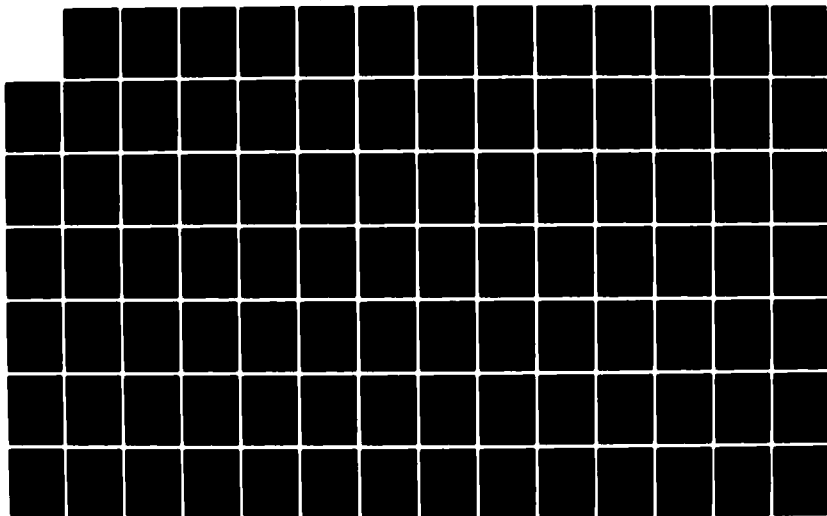
2/3

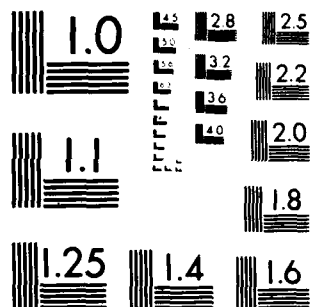
UNCLASSIFIED

AFOSR-TR-83-1136-VOL-2 AFOSR-81-0059

F/G 14/2

NL





MICROCOPY RESOLUTION TEST CHART
NATIONAL BUREAU OF STANDARDS-1963-A

However, crystals are available only with fixed 2d-spacings; the set of crystal 2d-spacings available in the soft x-ray regime is particularly limited. It is therefore of interest to consider the effect of a variation in 2d-spacing with wavelength held constant; this structural variation represents a degree of freedom not allowed in crystalline reflection.

By setting in eq.I-3-21

$$2d = \frac{\lambda}{\cos \theta_\theta} \quad (\text{II-3-22})$$

we have

$$\delta \theta_{FWHM} \cong 5.1 \times 10^{-6} \frac{\lambda^2 (\text{\AA})}{\sin 2\theta_\theta} \quad (\text{II-3-23})$$

This scaling law implies a large acceptance angle in the limits $\theta \Rightarrow 0^\circ$ and $\theta \Rightarrow 90^\circ$. (Eq. II-3-23 has a singularity at the limit points; our theory does not apply in the grazing regime, and eq. II-3-23 must be modified to apply in the normal incidence regime).

The large acceptance angles at the two extremes can be explained physically by the following arguments. (In fact, we will see that a certain symmetry exists between the two regions).

First, in the grazing regime, eq. II-1-11 implies a linear relationship between the wavelength and the angle ξ to the surface ($\xi \approx 90^\circ - \theta$). If we set for the grazing regime

$$\frac{\delta \lambda}{\lambda} = \frac{2d \sin \theta}{\lambda} \delta \theta = \tan \theta \delta \theta \approx \frac{\delta \xi}{\xi} \quad (\text{I-3-24})$$

then the linearity is reflected explicitly in the relation

$$\frac{\delta \lambda}{\lambda} = \frac{\delta \xi}{\xi} \quad (\text{I-3-25})$$

Further, the width of the high-reflectivity stopband in phase units is of order N^{-1} ; this is because N is the number of layer pairs participating in the reflection process. Thus the resolution of the multilayer is governed by the familiar rule

$$\frac{\delta \lambda}{\lambda} \sim \frac{1}{N} \quad (\text{I-3-26})$$

so that

$$\frac{\delta \xi}{\xi} \sim \frac{1}{N} \quad (\text{I-3-27})$$

The absorption within each cell is given by the product of the absorption coefficient with the path length through the cell, so that the scaling of the absorption per cell with angle must be of the form

$$\frac{4\pi\Delta''}{\lambda} \cdot \frac{d}{\cos\theta} \sim \frac{\Delta''}{\cos^2\theta} \sim \frac{\Delta''}{\xi^2} \quad (\text{II-3-28})$$

Here Δ'' represents the spatially averaged imaginary part of the index of refraction.

Since the absorption per cell is approximately the reciprocal of the number of effective layer pairs N ,

$$N \sim \frac{\xi^2}{\Delta''} \quad (\text{II-3-29})$$

and so we have

$$\frac{d\lambda}{\lambda} \sim \frac{d\xi}{\xi} \sim \frac{\Delta''}{\xi^2} \quad (\text{II-3-30})$$

Therefore $\delta\lambda/\lambda$ and $\delta\xi_{FWHM}$ both rise as $\xi \rightarrow 0$, but $\delta\lambda/\lambda$ rises more rapidly.

As discussed in sec. II-1-B, our formalism is invalid if

$$\xi \leq |\sqrt{\Delta}| \quad (\text{II-3-31})$$

In the near-grazing regime where our formalism is still valid, the dominant factor in the scaling of multilayer reflection properties is the quadratic dependence of the absorption per cell on ξ . The dependence is quadratic because as ξ is decreased, the photon path becomes more oblique, and also d must be increased.

While N depends quadratically on angle in the regime near grazing incidence, it becomes almost independent of angle as the normal incidence regime is approached, because the paths traversed through the layers become insensitive to angular variations.

For $\theta \leq 45^\circ$, we can therefore set

$$\frac{1}{N} \sim \Delta'' \quad (\text{II-3-32})$$

Similarly, in the normal incidence regime the linear dependence of λ on θ disappears; from eq. II-1-11

$$\frac{\delta\lambda}{\lambda} \sim \frac{\delta(\cos \theta)}{\cos \theta} \sim \tan \theta \delta\theta \quad (\text{II-3-33})$$

assuming that we are outside the regime very near normal incidence (i.e. outside the regime $\theta \lesssim \sqrt{\mu''}$). For $\theta \lesssim 45^\circ$ we can set $\tan \theta \sim \theta$ so that

$$\frac{\delta\lambda}{\lambda} \sim \theta \delta\theta \quad (\text{II-3-34})$$

Using

$$\frac{\delta\lambda}{\lambda} \sim \frac{1}{N} \sim \Delta'' \quad (\text{II-3-35})$$

we therefore have

$$\delta\theta \sim \frac{\Delta''}{\theta} \quad (\text{II-3-36})$$

which is the limiting form of eq. II-3-23.

Thus, the near-independence of path length on angle near the normal incidence regime implies a slower change in phase thickness with angle of incidence, leading to the large $\delta\theta_{FWHM}$ predicted by eq. II-3-23 or eq. II-3-36.

Within the normal incidence regime itself, i.e. when $\theta \leq \sqrt{\mu''}$ so that eq. II-3-33 no longer holds, we can set

$$\frac{\delta\lambda}{\lambda} \sim \frac{\delta(\cos\theta)}{\cos\theta} \sim (\delta\theta)^2 \quad (\text{I-3-37})$$

so that

$$\delta\theta \sim \sqrt{\Delta''} \quad (\text{I-3-38})$$

or more specifically

$$\begin{aligned} \delta\theta_{FWHM} &\cong 2 \sqrt{\frac{\delta\lambda_{FWHM}}{\lambda}} \cong 2 \sqrt{\frac{\delta\varphi_{FWHM}}{\pi}} \cong 2 \sqrt{\frac{2\mu''}{\pi}} \cong 3.1 \times 10^{-3} \lambda_{(\text{\AA})} \quad (\text{radians}) \\ &\cong 0.18 \lambda_{(\text{\AA})} \quad (\text{degrees}) \end{aligned}$$

(I-3-39)

Thus, collection angles of order 15° can be obtained at wavelengths around 100\AA . Multilayers may therefore make it possible to achieve the high resolutions that are potentially possible at x-ray wavelengths given large numerical apertures; for this purpose Lovas et al. (1982) have constructed an x-ray microscope based on a Schwartzchild configuration that is presently undergoing testing at the Brookhaven storage ring.

At shorter x-ray wavelengths, the λ^2 factor in the numerator of eq. II-3-23 in effect precludes single-substrate reflecting devices from having large collection angles. Further, the necessity of having layer thicknesses of at least a few angstroms precludes operation in the normal incidence regime; in order to obtain fields of view that are as large as possible it is therefore necessary to operate at quite small angles to the substrate surfaces (typically of order a few degrees or so). A device designed along these lines will be discussed in chapter III.

Section II-4 - Non-Periodic Multilayer Designs

In the optical regime, the familiar quarterwave stack is the most common reflective coating, but more complicated designs are often used.

In addition to periodic designs based on a thickness ratio other than quarterwave, such non-quarterwave multilayer designs include structures that are not periodic.

Non-periodic designs are resorted to for a variety of reasons, such as to increase bandwidth over the quarterwave value, or to introduce relative phase changes between different polarizations. We will restrict ourselves to the question of whether or not aperiodic x-ray multilayer designs can be used to reduce the effect of absorption and so increase the reflectivity.

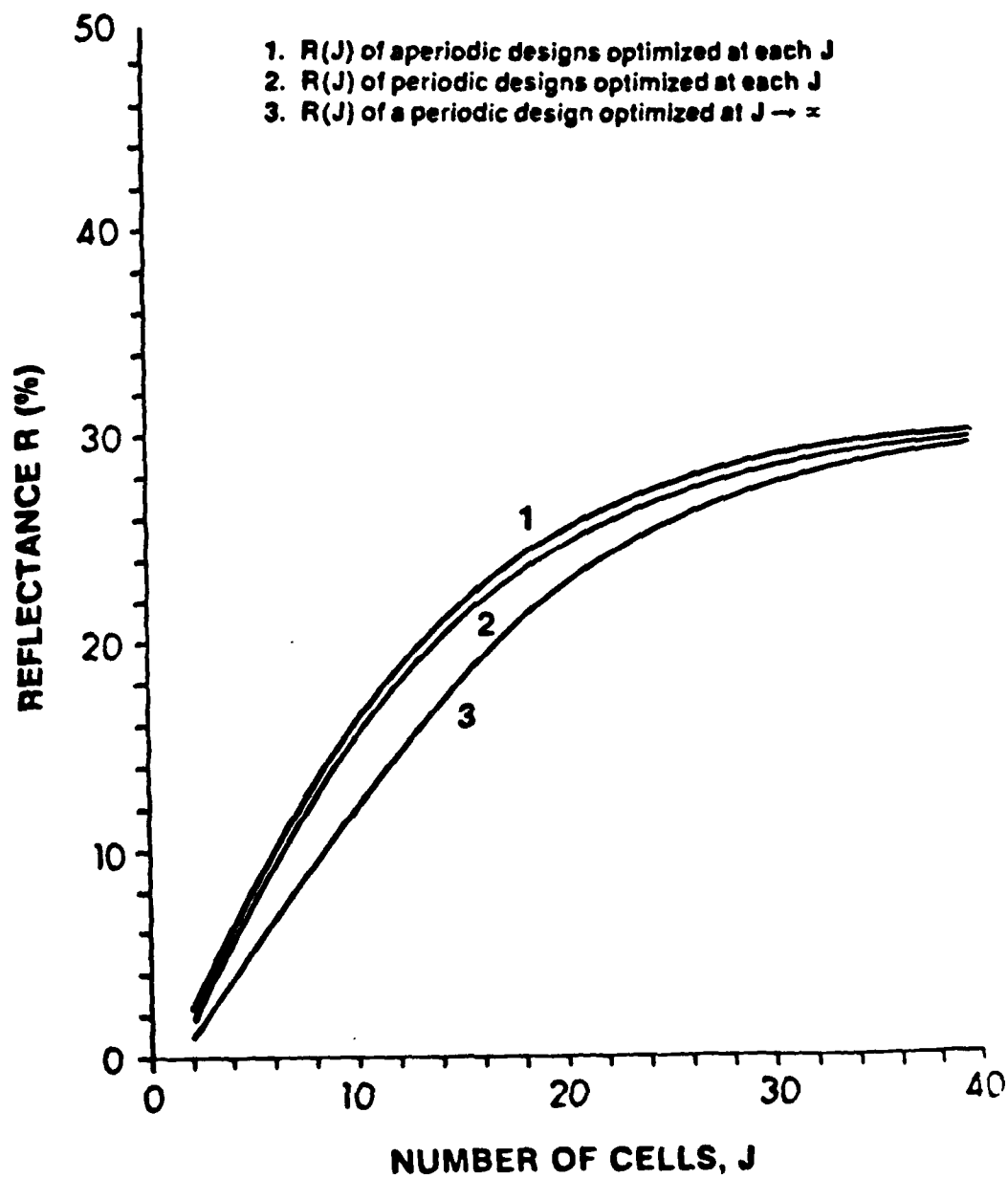
Other design objectives will be left for future research; however we note that in the soft x-ray regime there is a fixed budget of layers that are permitted in a design due to absorption, and often this fixed number of layers is inadequate to produce a high reflectivity at a single wavelength even in the absence of other design constraints. Techniques for modifying periodic designs that require large increases in the number of layers used might not be appropriate in the x-ray regime.

Carniglia and Apfel (1980) have developed aperiodic multilayer designs that yield higher reflectivity in the presence of absorption than can periodic multilayers containing the same number of layers. We will consider whether such gains are possible in the x-ray regime.

Our first result in this connection is obtained in Appendix 8. There we apply our difference equation in the case of a periodic reflector that has been optimized according to the formulas of sec. II-2-B, and prove that if the reflector contains a sufficient number of layer pairs, its reflectivity will be an extremum with respect to an arbitrary variation in structure (the variation used need not leave the structure periodic). A periodic multilayer coating having an optimized structure therefore provides at least a local extremum in the reflectivity.

Limited numerical studies suggest that this local extremum reflectivity is in fact a global maximum. Our most detailed set of numerical results is shown graphically in fig. II-4-1. Curve 1 shows attainable reflectivity versus number of layer pairs when all $2J$ layer thicknesses are treated as independent degrees of freedom. Curve 2 shows reflectivity versus J when the reflector is periodic; in this curve the two degrees of freedom in the basic period are reoptimized at each J value. Curve 3 shows the reflectivity of a periodic multilayer that has been optimized as discussed in sec. II-2-B to have maximum reflectivity in the steady-state limit. All curves are obtained using the non x-ray characteristic matrix solution of eq. II-2-22 with a canned optimization routine.

COMPARISON OF OPTIMIZATION SCHEMES



In the steady-state limit all three curves converge. Even when the number of layer pairs is somewhat less than $1/\text{Im}(\hat{S})$, the highest reflectivity that can be obtained from an aperiodic design is not very much larger than that obtained from an optimized periodic design. However, though the difference in R between the periodic and aperiodic designs is small, the set of parameters β_k, φ_k in the multilayers of curve 1 are in general quite different from the constant values for these parameters in curve 3, even in the limit of $J \rightarrow \infty$ (but not in the joint limit $J \rightarrow \infty, K \rightarrow \infty$).

One would like to test these conclusions as comprehensively as possible, but multi-dimensional optimization is very expensive.

Carniglia and Apfel have solved a simplified version of the $2J$ -dimensional optimization problem for visible HR reflectors. They show how to calculate the particular thicknesses for the top pair of layers in a bilayer stack that will maximize the total reflectivity of the multilayer, given that the preceding layer pairs have already been optimized in this way.

They hypothesize that such a two-by-two optimization is fully general; in other words that no increase in total reflectivity can be obtained by simultaneously changing the thicknesses of any preceding layers when a given pair of layers is being optimized using their algorithm.

Carniglia and Apfel's mathematical calculations are not applicable in the x-ray regime since they assume that in the preceding stack of layer pairs, $(1-R) \ll 1$.

Nonetheless, their basic concept is of interest in the x-ray regime because mirrors made by the in-situ reflectance monitoring (ISRM) technique discussed in Chapter I will have a related property. If, during a deposition session like that shown in fig. 9 of Spiller (1982b), one cuts off the depositions of successive high index layers at successive reflectance maxima, the ϕ value for each layer pair will automatically be optimized under an optimization scheme like Carniglia and Apfel's. The thickness ratio parameters β_k may be chosen by a different criterion, but the total thickness with which each pair of layers is terminated will be the thickness which maximizes the total reflectivity of the entire stack.

In Appendix 9 it is shown that in the x-ray regime the optimum ϕ_k , given an amplitude reflectance ρ_k from the stack of preceeding layers, satisfies the condition:

$$\text{Im} \left\{ \Delta_N \left[1 + \frac{P(\theta)}{2} \left(\rho_k e^{i\mu_k} e^{-2i\phi_k} + 1/\rho_k e^{i\mu_k} e^{-2i\phi_k} \right) \right] \right\} = 0 \quad (\text{II-4-1})$$

In Appendix 9 we show that the solution for ϕ_k is

$$\phi_k = \frac{1}{2} \left\{ \mu'_k + f(V_p, \mathcal{R}, V_N) - \arcsin \left[\sqrt{\frac{4\mathcal{R}}{1 + \mathcal{R}^2 - 2\mathcal{R} \cos(V_N)}} \frac{\sin V_N}{|P(\theta)|} \right] \right\}$$

$$\text{where } \mathcal{R} = |\rho_k|^2 e^{-2\mu_k''}$$

$$\rho_k = |\rho_k| e^{iV_p} \quad (\text{II-4-2})$$

$$\Delta_N = |\Delta_N| e^{iV_N}$$

$$f(V_1, G, V_2) = V_2 - \arctan \left[\frac{1+G}{1-G} \tan V_2 \right]$$

Here, as in sec. II-2-B, we will assume that the beam can be treated as linearly (S) polarized. The qualitative conclusions drawn in this section apply also in the case of unpolarized radiation. The key results in eqs. II-4-1,2,8 and 9 apply to both polarizations.

The optical constants used in eqs. II-4-1,2 are those of the ISRM monitoring wavelength, which might be different from those at which the coating is used, for example if the coating is meant to operate near normal incidence.

As K becomes large, the multilayer produced by ISRM becomes periodic, with ρ_n approaching the Darwin-Prins solution; in lowest order eq. II-4-1 becomes in S polarization

$$\text{Im} \left\{ \Delta_n \left[1 + \frac{is}{(\Delta_n - \Delta_l)} - \frac{t}{(\Delta_n - \Delta_l) \tan \beta_n} \right] \right\} = 0 \quad (\text{II-4-3})$$

If we now make the rough approximation that

$$\Delta_l \cong 0, \quad \Delta_n - \Delta_l \cong \Delta_n \quad (\text{II-4-4})$$

we get

$$(\Delta_n'' - \Delta_l'') + s' + \frac{\pi \Delta_l'' + \beta (\Delta_n'' - \Delta_l'')}{\tan \beta} = 0 \quad (\text{II-4-5})$$

This yields the correct Bragg condition

$$s' = 0 \quad (\text{II-4-6})$$

given that the optimization condition on β of sec. II-2-B is also satisfied, so that the sum of the first and last terms in eq. II-4-5 vanish.

However, $\Delta_L \approx 0$ is only a rough approximation, so that in general the Bragg condition will not be satisfied under the two-by-two optimization produced with ISRM.

Thus, in the x-ray regime the hypothesis of Carniglia and Apfel does not hold, and a 2x2 optimization scheme based on an L-H unit cell does not yield a fully optimized reflector; as a non-optimality in the Bragg condition the error may be considered to be equivalent to a small shift in λ or θ . As a small λ or θ shift, this non-optimality is not in itself crucial since it can be compensated for by an intentional small shift between the monitoring λ or θ and the λ or θ of the coating's intended application.

However, a similar problem arises when we consider a two-by-two optimization scheme for the β_k .

In general the β_k in an ISRM multilayer could be chosen in a variety of ways. For example, all β_k could be set equal to the β of an optimized periodic multilayer.

Alternatively, one could terminate deposition of the low index layers at reflectance minima. This turns out to produce β_n values that are numerically quite close to optimum.

Finally, one could choose each β_n in accordance with a 2x2 optimization scheme, choosing each β_n successively to maximize the reflectance of the stack of cells 1 ... K, as suggested by the discussion in (Spiller, 1976).

As shown in Appendix 9, each β_n under such an optimization scheme is given by

$$\beta_n = \frac{1}{2} \left\{ \pi + \arcsin \left[\frac{1/|P(\theta)|}{\sqrt{|\Delta_n - \Delta_L|^2 (1 + R^2 - 2R \cos(2V_q))}} \right] \times \right. \\ \left. (2\Delta_L \sqrt{R} + P(\theta) \sqrt{|\Delta_n|^2 (1 + R^2 - 2R \cos(V_n))} A) \right] + f(V_q, R, V_q) \right\}$$

where $A \equiv \sin(f(V_q, R, V_n))$,

$$\Delta_n - \Delta_L \equiv |\Delta_n - \Delta_L| e^{iV_q} \quad (\text{I-4-8})$$

which is the solution to the condition

$$\text{Im} \left\{ \Delta_1 + \frac{\Delta_n p(\theta)}{2} \left(\rho_n + \frac{1}{\rho_n} \right) - \frac{p(\theta)}{2} (\Delta_n - \Delta_1) \left(\rho_n e^{-2i\beta_n} + \frac{1}{\rho_n e^{-2i\beta_n}} \right) \right\} = 0 \quad (\text{II-4-9})$$

In the steady-state regime, eq. II-4-9 becomes in lowest order (for S polarization)

$$\text{Im} \left\{ \Delta_1 + \frac{\Delta_n}{\Delta_n - \Delta_1} \left(iS + \frac{t}{\tan \beta} \right) - \left(\frac{t}{\tan \beta} - iS \right) \right\} = 0 \quad (\text{II-4-10})$$

As before, this will not be consistent with the results of sec. II-2-B, unless we make the crude approximation $\Delta_1 \cong 0$. Thus, except to a rough approximation, the 2x2 optimization scheme converges to a non-optimal value of β as well as a non-optimal value of φ .

We can see an analogy with the periodic case by adding eq. II-4-3 to eq. II-4-10. We obtain in lowest order:

$$-S' + (\Delta_n'' - \Delta_1'') - \frac{\pi \Delta_1'' + \beta_n (\Delta_n'' - \Delta_1'')}{\tan \beta_n} = 0 \quad (\text{II-4-11})$$

Here it has not been assumed that $\Delta \approx 0$.

We showed above that under an ISRM scheme, non-negligible absorption and refraction in the low index layer cause the first term in the above condition to be non-zero. The sum of the second and third terms in the above condition cannot then be zero; and since such a cancellation is also the requirement for an optimized β , we can consider the non-satisfaction of the Bragg condition to have in turn prevented the 2x2 optimization scheme from converging to the correct thickness ratio.

This is similar to the situation we found when treating the optimization of periodic multilayers in sec. II-2-B, where we noted that our condition for optimizing β in a periodic multilayer applies only if the generalized Bragg condition $\text{Re}(\xi)=0$ is satisfied.

In the usual case that absorption and dispersion in the low index layer is small, the numerical consequences of these non-optimality is only moderate, since the accuracy of eq. II-4-4 increases as the index decrement in the low index layer goes to zero. A 67.6\AA , $\theta = 0^\circ$ reflector with $J=200$ would have a reflectance of .19 if designed by the 2x2 procedure, compared with a .22 reflectance from the optimum periodic design, for a $\Delta R/R$ of 15%.

Further, the β_K values and the monitoring conditions can be chosen in such a way as to compensate for this reflectivity loss. For example, if the monitoring and application wavelengths were the same one could introduce a shift between the monitoring angle and the application angle that would cancel the difference between eq. II-4-2 and eq. II-2-30; one could then choose the β_K under one of the alternative schemes described above.

II-4-11

The main advantage of the ISRM technique lies in its potential for strongly reducing the effect of random thickness errors, rather than in its use as a method for selecting the target thicknesses.

Section II-5 - Effect of Accumulating Random Thickness Errors on Multilayer Reflectivity

Part A) Introduction

X-ray multilayers must contain a large number of layer pairs since the reflectivity of individual layers is very small. The magnitude of uncorrected thickness errors in the multilayers must therefore be kept to a small fraction of a layer thickness in order to prevent a large cumulative dephasing from developing between the top and bottom of the stack. Because the layers themselves are only of order ten angstroms in thickness, the tolerance on random errors in the layers is extremely tight.

The two fabrication methods described in Chapter I can be regarded as alternative approaches to solving this problem.

Barbee's vacuum sputtering technique (Barbee, 1982) achieves precise control of the layer thicknesses through the use of sophisticated deposition procedures and apparatus; these include use of a magnetron sputtering source to prevent high energy ion bombardment of the substrate surface, precise control of the deposition voltage, and use of a multi-angle preparatory pre-deposition onto the substrate surface.

The second fabrication method is Spiller's in-situ reflectance monitoring technique (ISRM), which serves to eliminate the accumulation of dephasing from any thickness errors that may be present. The intensity of

the ISRM probe shows an interference oscillation as the thickness of the top layer increases; this oscillation is essentially determined by the absolute difference in phase between the upper surface of the top layer and the stack of preceding layers. The maxima in the peak intensities occur when the double-pass phase thickness of the upper pair of layers is approximately one wavelength; the precise single-pass phase thickness that is required is given by eq. II-4-2.

Eq. II-4-2 obtains even when the reflectivity ρ_n of the preceding stack is non-optimal due to thickness errors. Under ISRM, the target thickness for the upper layer of the final unit cell (aimed at by monitoring the ISRM probe intensity), is that thickness given by eq. II-4-2 which puts the top interface of the layer into phase with the preceding layers, thereby compensating in large part for any errors in those layers.

Multilayers of the first kind are subject to what we will call accumulating thickness errors, while those fabricated by ISRM are subject to what we will call non-accumulating thickness errors. We will analyze the effect of accumulating errors in part B, and will discuss our solution in part C. Non-accumulating errors will be discussed in sec. II-6.

Part B) Analysis of Accumulating Thickness Errors

Thickness errors of an accumulating type have been treated theoretically by Shellan et al. (1978), and have also been discussed briefly by Baumeister (1981). Shellan presents explicit closed-form solutions for the reflectivity, but some of his approximations are not appropriate to the x-ray case.

Shellan treats non-absorbing multilayers using coupled wave equations that contain perturbation terms to represent the effect of thickness errors. Shellan's coupled wave equations are of a form that apply to dielectric structures operating at the dielectric Bragg condition. The advantage here is more than the avoidance of complex indices of refraction; if the nominal phase thickness of the unit cell is both pure real and equal to π , the coupled wave solutions simplify considerably.

Shellan's analysis assumes a small coupling constant per cell, as is necessary when a large number of layers must participate in the reflection; in this feature his analysis is appropriate to the x-ray regime. In the limit that the perturbation terms are small, Shellan solves rigorously for the expectation value of the reflectance. He also obtains an expression for the reflectivity in the presence of larger errors, in the case of structures which contain sufficiently few layers that their overall reflectivity is small compared to one; to do this he uses what he calls an 'undepleted incident wave' approximation. In the context of x-ray diffraction, such structures might be said to be operating in the 'Fourier transform regime'.

X-ray reflectors necessarily have a small coupling constant because the x-ray indices of refraction of all materials are close to one. However, in the x-ray case a significant fraction of the coupling between the structure and the radiation field is due to absorption. Also, while the reflectivity of x-ray multilayers can be quite severely limited by absorption (leading to a situation where a relatively small number of layers participate in the reflection process), it is nonetheless usually a poor approximation to apply the undepleted incident wave approximation to x-ray multilayers.

It is also of particular interest in the x-ray case to be able to consider operation off the Bragg condition, since x-ray multilayers have very narrow bandwidths.

Another consideration in the x-ray case is that while present technology permits the fabrication of multilayers having $2d$ spacings of 100\AA and structures of fairly good quality, the soft x-ray spectrum can be considered to extend to normal incidence wavelengths that are shorter than this by an order of magnitude; in addition some experiments have been carried out in higher orders, which are in a sense equivalent to still shorter $2d$ -spacings. We will see below that the tolerance on accumulating thickness errors has an approximately quadratic scaling with $2d$ -spacing.

We therefore consider it desirable to be able to analyze the effect of thickness errors that are large enough in comparison with the layer thicknesses to substantially degrade the reflectivity; in this case a perturbation treatment is inappropriate.

For these reasons we have developed a new approach to treat the effect of random thickness errors on multilayer reflection. Our approach renders the problem of thickness errors tractable by using an approximation that applies rigorously in both the limit of large errors and the limit of small errors. The approximation also tends to be quite accurate in the intermediate region.

Our analysis is based on a decomposition of the amplitude reflectivity into what are essentially coherent and incoherent parts (see eq. II-5-10 below).

Our key approximation is to neglect cubic and higher powers of the incoherent reflectivity. It is essentially this approximation that allows steady-state solutions for the overall reflectivity to be found analytically (see eqs. II-5-35 and 41).

With further approximations we find solutions for the reflectivity outside the steady-state regime (this analysis is carried out in Appendix 10; the results are shown in eqs. II-5-42 and 45).

While we use a number of approximations in the derivation, it is the neglect of higher order powers in the incoherent reflectivity that is the key approximation in two senses. First, this is the approximation to which our results are numerically most sensitive. Second, the other approximations that we use are akin to our key approximation in that they allow our results to be correct in both the limits of large and small thickness errors. However, the other approximations generally relate to specific algebraic equations arising in the derivation.

We will use a particular x-ray multilayer as an example while presenting our analysis, namely a tungsten-carbon multilayer reflecting 67.6\AA radiation ($B-K_{\alpha}$) at normal incidence. The layer thicknesses in the absence of thickness errors, $d_w = 7.6\text{\AA}$, $d_c = 26.5\text{\AA}$, are chosen in accordance with the optimization conditions of sec. II-2-B. In our examples we will generally take $J = 200$, which is a sufficiently large number of layer pairs to place the structure in the steady-state regime.

Following Shellan, we have tested the accuracy of our method using a Monte Carlo simulation, in which a computer program is used to generate a large number of simulated multilayer stacks containing random errors, and to compare their mean reflectivity with the analytical prediction.

We have found that the analysis gives accurate results over a full range of RMS error heights, so long as the undegraded reflectance of the structure under consideration does not approach too closely to one.

We will calculate the mean reflectivity of multilayers that contain uncorrelated errors in the thicknesses d_k of the different cells. We will assume that the nominal multilayer structure is periodic, and that the statistical properties of the errors are the same in all layers. If d is the mean thickness, then let

$$d_k \equiv d + \Delta d_k \quad (\text{I-5-1})$$

where

$$\langle \Delta d_k \rangle = 0 \quad (\text{I-5-2})$$

$$\langle (\Delta d_k)^2 \rangle \equiv \sigma^2$$

We will treat the variance σ as a known quantity. If each cell consists of an L layer and an H layer, each of which has independent errors with variances $\langle \Delta L^2 \rangle$ and $\langle \Delta H^2 \rangle$, then due to the independence, $\sigma^2 = \langle \Delta L^2 \rangle + \langle \Delta H^2 \rangle$, and

$$\begin{aligned} \langle \Delta \phi_k^2 \rangle &= \frac{4\pi^2}{\lambda^2} \cos^2 \theta (\langle \Delta L^2 \rangle + \langle \Delta H^2 \rangle) \\ &= \frac{4\pi^2 \sigma^2}{\lambda^2} \cos^2 \theta \end{aligned} \quad (\text{I-5-3})$$

where from eq. II-1-11

$$\begin{aligned}\varphi_k &\equiv \langle \varphi \rangle + \Delta \varphi_k = \pi - \frac{2\pi d}{\lambda} \cos \theta + \Delta \varphi_k \\ &= \langle \varphi \rangle + \frac{2\pi \Delta d_k}{\lambda} \cos \theta \quad (\text{II-5-4})\end{aligned}$$

With these definitions eq. II-1-20 becomes in first order

$$\rho_{k+1} = e^{-2i\langle \varphi \rangle} e^{-2i\Delta \varphi_k} \rho_k - (i\tau - p) - (i\tau + p) \rho_k^2 \quad (\text{II-5-5})$$

We note that in eq. II-5-5, τ , p , and μ are treated as independent of φ ; this approximation is accurate to within terms of order $\varphi \cdot \Delta$. As discussed in sec. II-1-B, we can neglect terms of order $\varphi \cdot \Delta$ and Δ^2 in analyzing stochastic problems like the present one, but we must retain high orders in the parameter φ .

The fact that we can directly incorporate eq. II-5-4 into eq. II-5-5 is due to an advantage of the difference equation formalism; namely that the formalism directly incorporates the physical properties of the individual cells.

The fact that our equations use the properties of the different cells explicitly has another useful consequence. Because ρ_k is determined by the properties of the cells $K-1$, $K-2$, ..., but not by those of cell K

(see sec. II-1-B), we can write for arbitrary functions f and g ,

$$\langle f(\Delta \varphi_k) g(\varphi_k) \rangle = \langle f(\Delta \varphi_k) \rangle \langle g(\varphi_k) \rangle$$

(II-5-6)

and in particular,

$$\langle e^{-2i\Delta \varphi_k \varphi_k} \rangle = \langle e^{-2i\Delta \varphi_k} \rangle \langle \varphi_k \rangle$$

(II-5-7)

The first expectation value in eq. II-5-7 is the characteristic function of the variable $-2\Delta \varphi_k$ (Papoulis, 1965, p.159). Any probability distribution with known characteristic function can be used in the analysis to follow. For simplicity we will assume Gaussian statistics; as we will see, the final results are very insensitive to the exact choice of distribution function.

Then using

$$\langle e^{-2i\Delta \varphi_k} \rangle = e^{-2\langle \Delta \varphi^2 \rangle} \quad (II-5-8)$$

which holds for a Gaussian random variable with zero mean, we take the

expectation value of eq. II-5-5, and get

$$\langle p_{n+1} \rangle = e^{-2i\langle t \rangle} e^{-2\langle \Delta q^2 \rangle} \langle p_n \rangle - (ir+p) - (ir+p) \langle p_n^2 \rangle$$

(II-5-9)

Now, we define the variable \tilde{p} through the relation

$$p_n = \langle p_n \rangle + \tilde{p}_n$$

(II-5-10)

\tilde{p} therefore represents the random or non-deterministic part of the reflectivity. Since the phase of \tilde{p} is completely random, we may also regard it as the incoherent component of the reflected beam.

Since

$$\begin{aligned} \langle p_n^2 \rangle &= \langle \langle p_n \rangle^2 + 2\langle p_n \rangle \tilde{p}_n + \tilde{p}_n^2 \rangle \\ &= \langle p_n \rangle^2 + \langle \tilde{p}_n^2 \rangle \end{aligned}$$

(II-5-11)

eq. II-5-9 becomes

$$\begin{aligned} \langle p_{n+1} \rangle &= e^{-2i\langle t \rangle} e^{-2\langle \Delta q^2 \rangle} \langle p_n \rangle - (ir-p) \\ &\quad - (ir+p) \langle p_n \rangle^2 - (ir+p) \langle \bar{p}_n^2 \rangle \end{aligned} \quad (\text{II-5-12})$$

In order to solve this equation, we must obtain $\langle \bar{p}_n^2 \rangle$.
Subtracting eq. II-5-12 from eq. II-5-5,

$$\begin{aligned} \bar{p}_{n+1} &= \left[e^{-2i\langle t \rangle} e^{-2i\Delta q_n} - e^{-2i\langle t \rangle} e^{-2\langle \Delta q^2 \rangle} \right] \langle p_n \rangle \\ &\quad + e^{-2i\langle t \rangle} e^{-2i\Delta q_n} \bar{p}_n \\ &\quad - 2(ir+p) \langle p_n \rangle \bar{p}_n \\ &\quad - (ir+p) (\bar{p}_n^2 - \langle \bar{p}_n^2 \rangle) \end{aligned} \quad (\text{II-5-13})$$

Next we square eq. II-5-13, neglecting terms of order $q \cdot \Delta$ and Δ .

We find

$$\begin{aligned} \bar{p}_{n+1}^2 &= \left[e^{-4i\langle t \rangle} e^{-4i\Delta q_n} + e^{-4i\langle t \rangle} e^{-4\langle \Delta q^2 \rangle} \right. \\ &\quad \left. - 2e^{-4i\langle t \rangle} e^{-2i\Delta q_n} e^{-2\langle \Delta q^2 \rangle} \right] \langle p_n \rangle^2 \end{aligned}$$

(continued on next page)

$$\begin{aligned}
 & + e^{-4i\langle t \rangle} e^{-4\langle \Delta q^2 \rangle} \bar{p}_k^2 \\
 & + 2 \left[e^{-2i\langle t \rangle} e^{-2i\Delta q_k} \right] \left[e^{-2i\langle t \rangle} e^{-2i\Delta q_k} - e^{-2i\langle t \rangle} e^{-2\langle \Delta q^2 \rangle} \right] \langle p_k \rangle \bar{p}_k \\
 & - 4(i\tau + p) \langle p_k \rangle \bar{p}_k^2 - 2(i\tau + p) (\bar{p}_k^3 - \bar{p}_k \langle \bar{p}_k^2 \rangle)
 \end{aligned}$$

(II-5-14, continued)

Defining

$$\bar{s}_k \equiv -\langle t \rangle - (\tau - ip) \langle p_k \rangle \quad (\text{II-5-15})$$

we can combine the second and the second to last terms on the right of eq. II-5-14 to obtain

$$\begin{aligned}
 \bar{p}_{k+1}^2 &= \left[e^{-4i\langle t \rangle} e^{-4i\Delta q_k} + e^{-4i\langle t \rangle} e^{-4\langle \Delta q^2 \rangle} - 2e^{-4i\langle t \rangle} e^{-2\langle \Delta q^2 \rangle} e^{-2i\Delta q_k} \right] \langle p_k \rangle^2 \\
 & + 2 \left[e^{-4i\langle t \rangle} e^{-4i\Delta q_k} - e^{-4i\langle t \rangle} e^{-2i\Delta q_k} e^{-2\langle \Delta q^2 \rangle} \right] \langle p_k \rangle \bar{p}_k \\
 & + e^{+4i\bar{s}_k} e^{-4\langle \Delta q^2 \rangle} \bar{p}_k^2 - 2(i\tau + p) (\bar{p}_k^3 - \bar{p}_k \langle \bar{p}_k^2 \rangle)
 \end{aligned}$$

(II-5-16)

The error in this substitution is of order $q \cdot \Delta$.

Taking expectation values, and using $\langle \bar{p} \rangle = 0$, we get:

$$\begin{aligned} \langle \bar{p}_{n+1}^2 \rangle = & \left[e^{-4i\langle t \rangle} e^{-i\langle \Delta q^2 \rangle} + e^{-4i\langle t \rangle} e^{-4i\langle \Delta q^2 \rangle} - 2e^{-4i\langle t \rangle} e^{-4i\langle \Delta q^2 \rangle} \right] \langle p_n \rangle \\ & + e^{-4i\langle t \rangle} e^{-i\langle \Delta q^2 \rangle} \langle \bar{p}_n^2 \rangle - 2(ir + p) \langle \bar{p}_n^2 \rangle \end{aligned} \quad (\text{II-5-17})$$

We will first find steady-state solutions to eqs. II-5-12,17. In order to operate in the steady-state limit, a multilayer must contain a number of layers sufficient to extinguish the incident beam before it reaches the substrate. In addition, the statistical properties of the thickness errors must be independent of K . In general, extinction may result from a combination of absorption, dephasing due to detuning from Bragg resonance, dephasing due to thickness errors, and depletion by back-reflection.

In the soft x-ray regime, absorption is a somewhat more important extinction mechanism than depletion by back-reflection, so that, following the discussion of sec. II-3, we may consider a multilayer to operate in the steady-state regime if

$$J \geq (\mu'')^{-1} \quad (\text{II-5-18})$$

Following the discussion of sec. II-1-B, we can consider the total phase error contained within the structure of a multilayer operating in the steady-state limit to be of order $(\langle \Delta q^2 \rangle / \mu'')^{1/2}$, assuming that

the thickness errors accumulate in a random walk fashion.

When $\langle \Delta \phi^2 \rangle \ll \mu''$, the errors may be treated as a small perturbation on the ideal periodic structure, and may be considered to cause only a small drop in reflectivity. (This will be shown more rigorously below).

On the other hand, if $\langle \Delta \phi^2 \rangle \gg \mu''$, the errors cause a substantial drop in reflectivity, and can no longer simply be treated as a perturbation.

In the soft x-ray regime, the condition $\langle \Delta \phi^2 \rangle \ll \mu''$ is considerably more restrictive than the condition $\langle \Delta \phi^2 \rangle \ll 1$. When $\langle \Delta \phi^2 \rangle$ approaches one, the different layer pairs can no longer interact coherently and the reflectivity becomes very small, assuming that the structure has a small coupling constant. (In our 67.6Å example with $\langle \Delta \phi^2 \rangle$ set to 1, the Monte Carlo simulation program described below shows that $R = 0.0027$). The assumption $\langle \Delta \phi^2 \rangle \ll 1$ is therefore an assumption that the structure maintains some resonant reflectivity; it is a generalization of a standard assumption in crystal diffraction theory, which in our notation states that $\phi \ll 1$.

In the analysis that follows, we will not need to assume that $\langle \Delta \phi^2 \rangle \ll \mu''$, but will assume that $\langle \Delta \phi^2 \rangle \ll 1$, or more specifically that terms of order $\Delta \phi^3$ are negligible. If in cases of greatest interest, $\langle \Delta \phi^2 \rangle \sim \mu''$, then terms of order $\Delta \phi^3$ are numerically comparable to terms of order $\phi \cdot \Delta$.

The distinction should be born in mind when following the discussion in (Shellan, 1978), whose perturbation treatment in essence makes the assumption that $\langle \Delta \varphi^2 \rangle \ll |\mu|$.

We should note that the above arguments are somewhat oversimplified in that they only consider extinction of the beam due to error-induced dephasing and absorption. We will see below how these criteria are generalized.

Neglecting terms of order $\Delta \varphi^3$, we can set

$$\begin{aligned} \langle e^{i\Delta \varphi_n} \rangle &\cong \langle 1 + i\Delta \varphi_n - \frac{\Delta \varphi_n^2}{2} \rangle \\ &= 1 - \frac{\langle \Delta \varphi^2 \rangle}{2} \end{aligned} \quad (1-5-19)$$

independent of the probability distribution satisfied by the random errors.

Eq. II-5-17 then becomes (neglecting terms of order $\varphi \cdot \Delta$ and Δ^2):

$$\begin{aligned} \langle \tilde{\rho}_{n+1}^2 \rangle &= -4 \langle \Delta \varphi^2 \rangle \langle \rho_n^2 \rangle + (1 + 4i\tilde{\gamma} - 8 \langle \Delta \varphi^2 \rangle) \langle \tilde{\rho}_n^2 \rangle \\ &\quad - 2(i\tilde{\gamma} + \rho) \langle \tilde{\rho}_n^3 \rangle \end{aligned} \quad (1-5-20)$$

The key approximation used in the present analysis is based on the double inequality

$$\langle |\tilde{\rho}|^2 \rangle < \langle |\rho|^2 \rangle < 1 \quad (\text{II-5-21})$$

The right hand inequality is fairly strong in the soft x-ray regime, where the absorption-limited reflectivity is typically of order 20%. The right hand inequality is particularly strong when $\langle \Delta \phi^2 \rangle \gg \mu''$, since the multilayer reflectivity is then severely degraded by the random thickness errors.

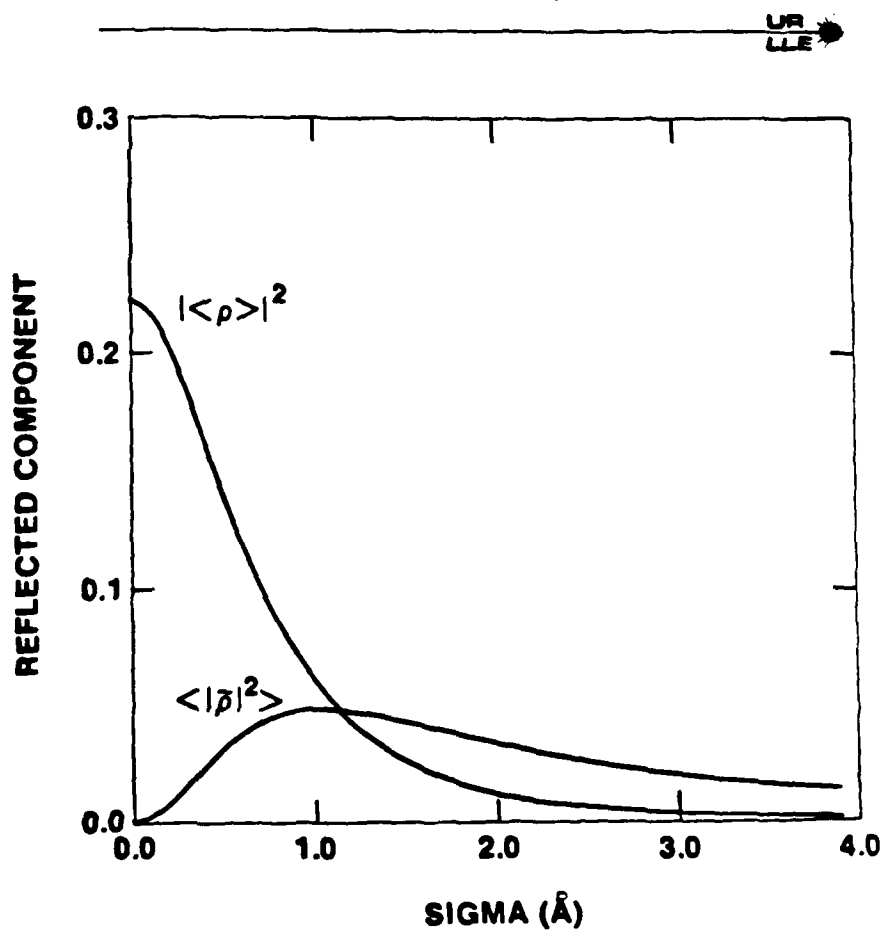
On the other hand, the left hand inequality becomes very strong when $\langle \Delta \phi^2 \rangle \ll \mu''$, since in the limit that the errors are small, $\langle \rho \rangle$ approaches ρ (see eq. II-5-10).

Since both inequalities are always in force to a certain extent, one can generally assume that $\langle |\tilde{\rho}|^2 \rangle$ is small compared to one (see fig. II-5-1 which shows $\langle |\tilde{\rho}|^2 \rangle$ plotted as a function of σ). We will therefore assume that terms which are cubic or higher in $\tilde{\rho}$ are completely negligible.

It is this neglect of cubic terms in $\tilde{\rho}$ that renders the problem of random thickness errors tractable over a broad range of error magnitudes.

These cubic terms are particularly small in the limits $\langle \Delta \phi^2 \rangle \ll \mu''$ or $\langle \Delta \phi^2 \rangle \gg \mu''$. Our analysis is therefore most sensitive to the approximations we have made at values of σ in the

DETERMINISTIC VERSUS NON-DETERMINISTIC COMPONENT OF REFLECTED BEAM



X357

Figure 11-5-1

intermediate region. In our 67.6Å example, $\langle \Delta \varphi^2 \rangle = \mu''$ at $\sigma = 1.22\text{Å}$; we will use $\sigma = 1\text{Å}$ when presenting numerical examples.

Our key approximation has been found to be quite accurate for multilayers operating in the soft x-ray regime, as the numerical examples presented below will show.

If we neglect terms of order $\tilde{\rho}^3$ in eq. II-5-20, we get

$$\langle \tilde{\rho}_{n+1}^2 \rangle = \langle |\tilde{\rho}_n|^2 \rangle + (4i\tilde{s}_n - 8\langle \Delta \varphi^2 \rangle) \langle |\tilde{\rho}_n|^2 \rangle - 4\langle \Delta \varphi^2 \rangle \langle \rho_n^2 \rangle$$

(II-5-22)

(At $\sigma = 1\text{Å}$ in our 67.6Å example, the neglected cubic terms have about 0.04 of the magnitude of the third term on the right in eq. II-5-22).

When radiation no longer reaches the substrate,

$$\langle \tilde{\rho}_{n+1}^2 \rangle = \langle \tilde{\rho}_n^2 \rangle = \langle \tilde{\rho}^2 \rangle \quad \text{so that eq. II-5-22 has the solution}$$

$$\langle \tilde{\rho}^2 \rangle = - \frac{\langle \Delta \varphi^2 \rangle \langle \rho \rangle}{-i\tilde{s} + 2\langle \Delta \varphi^2 \rangle} \quad (\text{II-5-23})$$

In the steady-state this solution can be substituted into the last term of eq. II-5-12, which then becomes

$$\begin{aligned} \langle \rho \rangle = & e^{-2i\langle t \rangle} e^{-2\langle \Delta \phi^2 \rangle} \langle \rho \rangle - (ir - p) \\ & - (ir + p) \langle \rho \rangle^2 \left(1 - \frac{\langle \Delta \phi^2 \rangle}{i\langle t \rangle + 2\langle \Delta \phi^2 \rangle + (ir + p)\langle \rho \rangle} \right) \end{aligned}$$

(II-5-24)

or, neglecting terms of order $\rho \cdot \Delta$ and ρ^4 ,

$$\begin{aligned} \langle \rho \rangle 2(i\langle t \rangle + \langle \Delta \phi^2 \rangle) = & - (ir - p) \\ & - (ir + p) \langle \rho \rangle^2 \left(1 - \frac{\langle \Delta \phi^2 \rangle}{i\langle t \rangle + 2\langle \Delta \phi^2 \rangle + (ir + p)\langle \rho \rangle} \right) \end{aligned}$$

(II-5-25)

This equation reduces to a cubic polynomial in $\langle \rho \rangle$.

We note that the substitution of eq. II-5-23 into the last term of eq. II-5-12 tends to be quite accurate in the soft x-ray regime, for three reasons. First, $|(ir + p)|$ is generally somewhat less than $|2i\langle t \rangle|$, so that our approximation is made in one of the less sensitive terms of eq. II-5-12. Second, the factor $\langle \tilde{\rho}^2 \rangle$ in the fourth

term is small compared to the factor $\langle \rho \rangle^2$ in the third term, except when $\langle \Delta \phi^2 \rangle \gg \mu''$, in which case both the third and fourth terms of the equation become small compared to the second term. In our 67.6 Å example the last term of eq. II-5-12 is 0.22 of the magnitude of the second term on the right-hand side at $\sigma = 1 \text{ Å}$. Finally, the cubic terms in $\bar{\rho}$ that are neglected in eq. II-5-23 tend to be quite small as discussed above.

Using similar approximations, eq. II-5-25 can now be converted from a cubic equation to a quadratic equation with very little loss in accuracy. In the soft x-ray regime $\langle \rho \rangle^2$ is fairly small even when the errors are small, making the second to last term of eq. II-5-12 small. The last term of eq. II-5-12 tends to be somewhat small for reasons discussed in the preceding paragraph. The steady-state solution of eq. II-5-12 when these two terms are neglected is

$$\langle \rho \rangle = \frac{[(r+ip)/2 \langle t \rangle]}{1 + \langle \Delta \phi^2 \rangle / i \langle t \rangle} \quad (\text{II-5-26})$$

(From this one can derive the expression

$$|\langle \rho \rangle|^2 = \frac{|r+ip|^2/4}{(\langle \rho \rangle - \mu')^2 + (\langle \Delta \phi^2 \rangle + \mu'')^2} \quad (\text{II-5-27})$$

which is quite useful for rough estimations). The argument used in deriving eq. II-2-26 can be considered to be somewhat analogous to Shellan's "undepleted incident wave" approximation.

Eq. II-5-26 is least accurate when $\langle \Delta \phi^2 \rangle \ll \mu''$, since the neglected second to last term of eq. II-5-12 can then approach the same order of magnitude as the second term.

Eq. II-5-26 can be normalized to give the correct $\sigma = 0$ value by re-writing it as

$$\langle p \rangle = \frac{p_0}{1 + \langle \Delta \phi^2 \rangle / it} \quad (\text{II-5-28})$$

where the numerator is the solution to eq. II-5-5 when $\sigma = 0$, namely eq. II-2-11.

The following considerations permit a further improvement in the accuracy of eq. II-5-26 when σ is small. If σ is small, the factor $\tilde{\delta}$ in the denominator of eq. II-5-23 can be set equal to δ (given by eq. II-2-27), since the left hand inequality in eq. II-5-21 becomes very strong, permitting neglect of terms of order $(\langle \Delta \phi^2 \rangle / \mu'')^2$. Eq. II-5-24 then becomes

$$\begin{aligned} \langle p \rangle (2i\langle \epsilon \rangle + 2\langle \Delta \phi^2 \rangle) &= -(ir-p) - (ir+p)\langle p \rangle^2 \\ &\quad - (ir+p)\langle p \rangle^2 - (ir+p) \frac{\langle \Delta \phi^2 \rangle}{i\delta} \langle p \rangle^2 \end{aligned} \quad (\text{II-5-29})$$

where we have set $-i\bar{s} + 2\langle\Delta\phi^2\rangle \approx -i\bar{s}$ in the last term, since we are for the moment considering $(\langle\Delta\phi^2\rangle/\mu'')^2$ to be small.

If we define $\Delta\rho \equiv \langle\rho\rangle - \rho_0$, and neglect terms of order $\langle\Delta\phi^2\rangle(\Delta\rho)$, eq. II-5-29 becomes

$$\Delta\rho 2i\langle t\rangle + 2\langle\Delta\phi^2\rangle\rho_0 = -2(ir+p)\rho_0\Delta\rho - (ir+p)\frac{\langle\Delta\phi^2\rangle}{i\bar{s}}\rho_0^2$$

(II-5-30)

which with the use of eq. II-2-11 reduces to

$$\langle\rho\rangle = \rho_0 \left(1 - i\langle\Delta\phi^2\rangle \left(\frac{\bar{s} - \langle t\rangle}{2\bar{s}^2} \right) \right)$$

(II-5-31)

(This may be regarded as a second-order perturbation solution to eq. II-5-9.) Writing

$$1 - i\left(\frac{\bar{s} - \langle t\rangle}{2\bar{s}^2}\right)\langle\Delta\phi^2\rangle \approx \frac{1}{1 + i\left(\frac{\bar{s} - \langle t\rangle}{2\bar{s}^2}\right)\langle\Delta\phi^2\rangle} + O\left(\left[\frac{\langle\Delta\phi^2\rangle}{\mu''}\right]\right)$$

(II-5-32)

we can rewrite eq. II-5-31 as

$$\langle \rho \rangle = \frac{\rho_0}{1 + i \left(\frac{\delta - \langle t \rangle}{2\delta^2} \right) \langle \Delta \phi^2 \rangle} \quad (\text{II-5-33})$$

so that it now has the correct limiting behavior when σ is small.

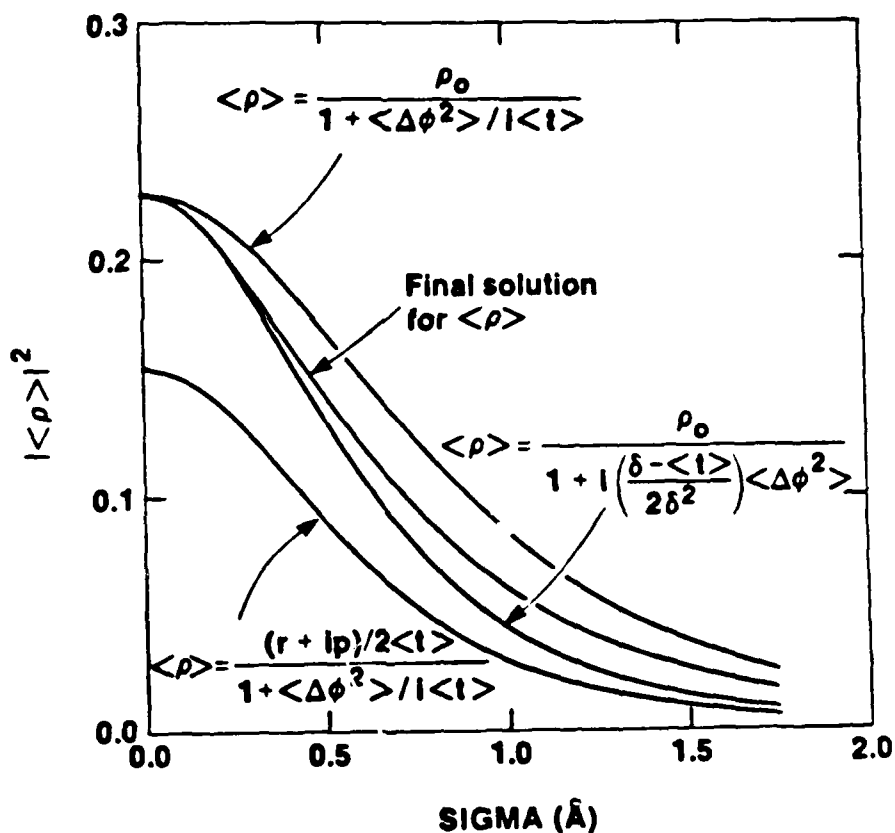
Eqs. II-5-26,33 are plotted in fig. II-5-2 for the case of our 67.6A example.

Substituting eq. II-5-33 into the last term of eq. II-5-25 (note that this last term is most significant at small σ , where eq. II-5-33 is designed to be most accurate), we obtain the quadratic

$$\begin{aligned} \langle \rho \rangle^2 (r - ip) \left(1 - \frac{\langle \Delta \phi^2 \rangle}{i \langle t \rangle + 2 \langle \Delta \phi^2 \rangle - \frac{i(\delta + \langle t \rangle)}{1 + i \left(\frac{\delta - \langle t \rangle}{2\delta^2} \right) \langle \Delta \phi^2 \rangle}} \right) \\ + 2 \langle \rho \rangle (\langle t \rangle - i \langle \Delta \phi^2 \rangle) + (r + ip) = 0 \end{aligned}$$

(II-5-34)

SUCCESSIVE APPROXIMATIONS FOR $\langle \rho \rangle$ TUNGSTEN-CARBON MULTILAYER

UR
LE

Plots are for a W/C multilayer reflecting 67.6 Å radiation at normal incidence. $d_w = 7.6 \text{ Å}$, $d_c = 26.5 \text{ Å}$.

X355

Figure II-5-2

whose solution, after manipulation, is found to be

$$\begin{aligned} \langle \rho \rangle = & - \left\{ \frac{\langle \Delta \phi^2 \rangle \left(2 - \left[\frac{\delta - \langle t \rangle}{2\delta^2} \right] [\langle t \rangle + 2i\langle \Delta \phi^2 \rangle] \right) - i\delta}{(r - ip) \left[\langle \Delta \phi^2 \rangle \left(1 - \left[\frac{\delta - \langle t \rangle}{2\delta^2} \right] [\langle t \rangle + i\langle \Delta \phi^2 \rangle] \right) - i\delta \right]} \right\} \\ & \times \left\{ (\langle t \rangle - i\langle \Delta \phi^2 \rangle) + \left[(\langle t \rangle - i\langle \Delta \phi^2 \rangle)^2 \right. \right. \\ & \left. \left. - \frac{(r^2 + p^2) \left[\langle \Delta \phi^2 \rangle \left(2 - \left[\frac{\delta - \langle t \rangle}{2\delta^2} \right] [\langle t \rangle + 2i\langle \Delta \phi^2 \rangle] \right) - i\delta \right]}{\langle \Delta \phi^2 \rangle \left(1 - \left[\frac{\delta - \langle t \rangle}{2\delta^2} \right] [\langle t \rangle + i\langle \Delta \phi^2 \rangle] \right) - i\delta} \right]^{\frac{1}{2}} \right\} \end{aligned}$$

(II-5-35)

This is our final solution for $\langle \rho \rangle$ in the steady-state regime; it is plotted in fig. II-5-2.

Since

$$\begin{aligned} \langle R \rangle &= \langle |\langle p \rangle|^2 + 2 \operatorname{Re}(\langle p \rangle \tilde{p}^*) + |\tilde{p}|^2 \rangle \\ &= |\langle p \rangle|^2 + \langle |\tilde{p}|^2 \rangle \end{aligned} \quad (\text{II-5-36})$$

we need to find $\langle |\tilde{p}|^2 \rangle$ in the steady-state in order to find $\langle R \rangle$.

Taking the magnitude squared of eq. II-5-13, and neglecting terms of order $\varphi \cdot \Delta$ and Δ^2 gives

$$\begin{aligned} |\tilde{p}_{n+1}|^2 &= |\tilde{p}_n|^2 - 4(\Delta \varphi_n^2 + \operatorname{Im}(\tilde{S}_n))|\tilde{p}_n|^2 + 4\Delta \varphi_n^2 |\tilde{p}_n|^2 + 4\Delta \varphi_n^2 |\langle p_n \rangle|^2 \\ &\quad + 8\Delta \varphi_n^2 \operatorname{Re}(\langle p_n \rangle^* \tilde{p}_n) + 8 \operatorname{Re}((\langle \Delta \varphi^2 \rangle - \Delta \varphi_n^2 - i\Delta \varphi_n) \langle p_n \rangle \tilde{p}_n^*) \\ &\quad - 2 \operatorname{Re}((ir+p)(|\tilde{p}_n|^2 \tilde{p}_n - \tilde{p}_n^* \langle \tilde{p}_n^2 \rangle)) \end{aligned}$$

(II-5-37)

We have neglected terms of order $(\Delta\phi^3)$, and have used eq. II-5-15.

The final term on the right of eq. II-5-37 is of order ϕ^3 , and we will neglect it for the reasons discussed above.

Taking expectation values:

$$\langle |\tilde{p}_{k+1}|^2 \rangle = \langle |\tilde{p}_k|^2 \rangle - 4\tilde{s}_k'' \langle |\tilde{p}_k|^2 \rangle + 4\langle \Delta\phi^2 \rangle |\langle \phi_k \rangle|^2$$

(II-5-38)

In the steady-state

$$\langle |\tilde{p}_{k+1}|^2 \rangle = \langle |\tilde{p}_k|^2 \rangle = \langle |\tilde{p}|^2 \rangle$$

(II-5-39)

so that

$$\langle |\tilde{p}|^2 \rangle = \frac{\langle \Delta\phi^2 \rangle}{\tilde{s}''} |\langle \phi \rangle|^2$$

(II-5-40)

The neglect of cubic terms is a poorer approximation here than it was in the steps between eqs. II-5-20 and 23, since in the latter case the cubic terms were neglected only in less sensitive terms of eq. II-5-12.

In our 67.6\AA example at $\sigma = 1\text{\AA}$, the $\bar{\rho}^3$ terms neglected in eq. II-5-37 total about 0.06 of the magnitude of the terms kept.

From eq. II-5-36 our steady-state solution for $\langle R \rangle$ is thus

$$\langle R \rangle = \langle |\rho|^2 \rangle \left(1 + \frac{\langle \Delta \rho^2 \rangle}{\bar{\rho}^2} \right) \quad (\text{II-5-41})$$

with $\langle |\rho|^2 \rangle$ obtained from eq. II-5-35.

We now wish to determine $\langle R \rangle$ outside the steady-state regime, i.e. for the case of a multilayer containing sufficiently few layers that a significant portion of the incident beam is transmitted into the substrate.

The analysis for the finite-K regime is presented in Appendix 10. Using approximations that are similar in spirit to those used in the steady-state analysis, we find that the reflectivity of a multilayer containing J-1 cells is

$$\langle \rho_J \rangle = \frac{\langle \rho_m \rangle (1 - e^{2iD(J-1)})}{1 - \left(\frac{r-ip}{r+ip} \right) \left(\frac{-i\tilde{\delta}_m + \langle \Delta \phi^2 \rangle}{-i\tilde{\delta}_m + 2\langle \Delta \phi^2 \rangle} \right) \langle \rho_m \rangle^2 e^{2iD(J-1)}}$$

(II-5-42)

where

$$D \equiv \sqrt{-(i\langle t \rangle + \langle \Delta \phi^2 \rangle)^2 - (r^2 + p^2) \left(\frac{-i\tilde{\delta}_m + \langle \Delta \phi^2 \rangle}{-i\tilde{\delta}_m + 2\langle \Delta \phi^2 \rangle} \right)}$$

(II-5-43)

Here $\langle \rho_m \rangle$ is the steady-state solution of eq. II-5-35. The subscript on $\tilde{\delta}_m$ indicates that eq. II-5-15 is to be evaluated in the steady-state. In the special case of a bilayer reflector

$$\langle \rho_j \rangle = \frac{\langle \rho_m \rangle (1 - e^{2iD(J-1)})}{1 - e^{-2i\beta} \left(\frac{-i\tilde{\delta}_m + \langle \Delta \phi^2 \rangle}{-i\tilde{\delta}_m + 2\langle \Delta \phi^2 \rangle} \right) \langle \rho_m \rangle^2 e^{2iD(J-1)}} \quad (\text{II-5-44})$$

Our solution for $\langle |\tilde{\rho}_j|^2 \rangle$ outside the steady-state regime is

$$\begin{aligned} \langle |\tilde{\rho}_j|^2 \rangle &= \frac{2\langle \Delta \phi^2 \rangle |\langle \rho_j \rangle|^2}{|1 - e^{2i(J-1)D}|^2} \\ &\times \left[\frac{1 - e^{-4(J-1)\tilde{\delta}_j''}}{2\tilde{\delta}_j''} - \text{Re} \left(\frac{e^{2i(J-1)D} - e^{-4(J-1)\tilde{\delta}_j''}}{\tilde{\delta}_j'' + iD/2} \right) \right. \\ &\quad \left. + \frac{e^{-4(J-1)D''} - e^{-4(J-1)}}{2(\tilde{\delta}_j'' - D'')} \right] \end{aligned} \quad (\text{II-5-45})$$

Here $\tilde{\delta}_j$ is given by eq. II-5-15.

$\langle \rho_j \rangle$ is now given by eq. II-5-36.

In order to test the overall accuracy of the different approximations used in deriving our solution, we have written a Monte-Carlo program to directly simulate the effect of random thickness errors.

The reflectivities of the simulated stacks are computed using the characteristic matrix method. The exact (non x-ray) characteristic matrix solution of eq. II-1-22 is used, rather than the x-ray approximation of eq. II-1-14. A Gaussian random number generator is used to obtain the thickness errors.

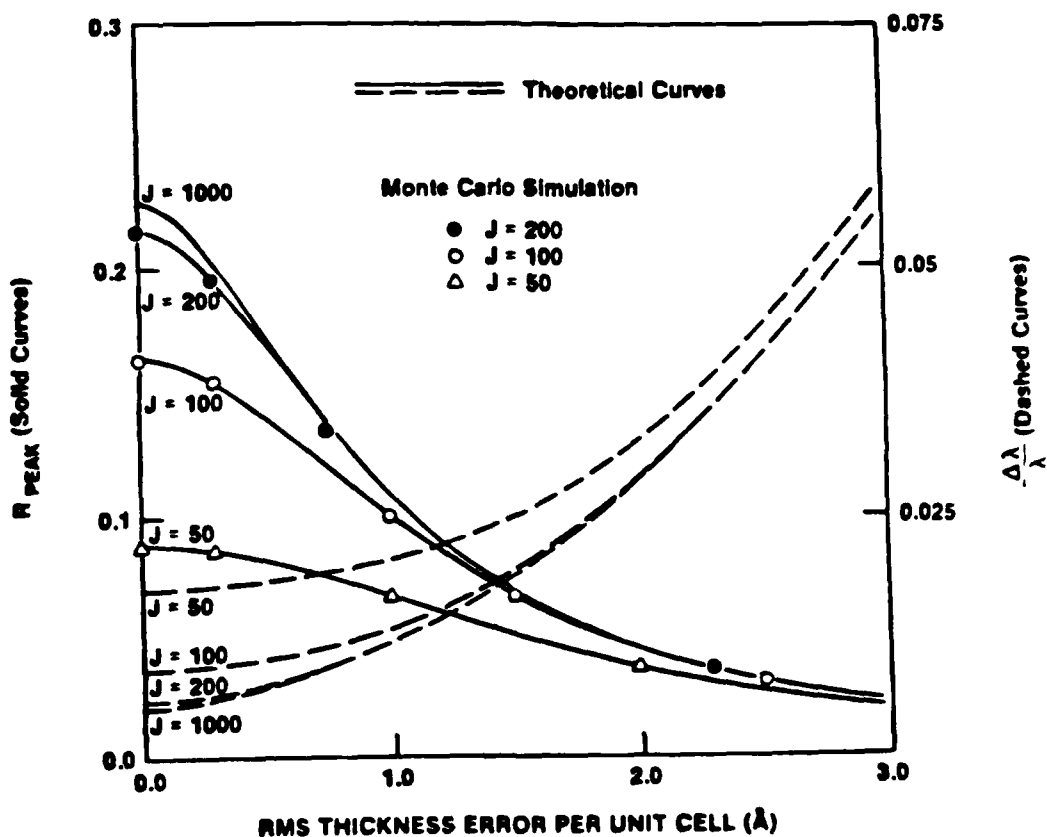
Fig. II-5-3 compares our solution to the Monte Carlo results. The tested values of σ include the parabolic portions of the curves in the small- σ perturbation regime, where $\Delta R/R \ll 1$, and extend into the large- σ regime where the drop in R from its undegraded value is quite substantial.

By varying the sample size and studying the observed scatter in the Monte Carlo results, we estimate the accuracy of the results due to the finite sample size (usually 2000 simulated stacks) to be about ± 0.0005 .

The theoretical curves for $\Delta\lambda/\lambda$ in fig. II-5-3 were obtained by numerically finding the half-max points of $\langle R_\mu \rangle$. This procedure implicitly makes the assumption that the half-width (in wavelength) of the expected reflectivity is equal to the expectation value of the half-width of reflectivity.

This is a reasonable assumption to make in order to obtain a rough idea of the behavior of $\Delta\lambda/\lambda$; further one can make arguments showing explicitly that the assumption should be accurate if σ is small. However it would be very expensive to test this assumption using a Monte Carlo

EFFECT OF RANDOM THICKNESS ERRORS ON MULTILAYER REFLECTIVITY



Plots are for a W/C multilayer reflecting 67.6 Å radiation
at normal incidence. $d_w = 7.6$ Å, $d_c = 26.5$ Å.

X276

Figure II-5-3

simulation; we have not done so, so the $\Delta\lambda/\lambda$ curves in fig. II-5-3 should only be regarded as approximate.

One would expect our solution for $\langle R_r \rangle$ to become less accurate as the undegraded reflectivity of the structure under consideration becomes large, because in that case neither inequality in eq. II-5-21 will hold strongly at intermediate values of σ .

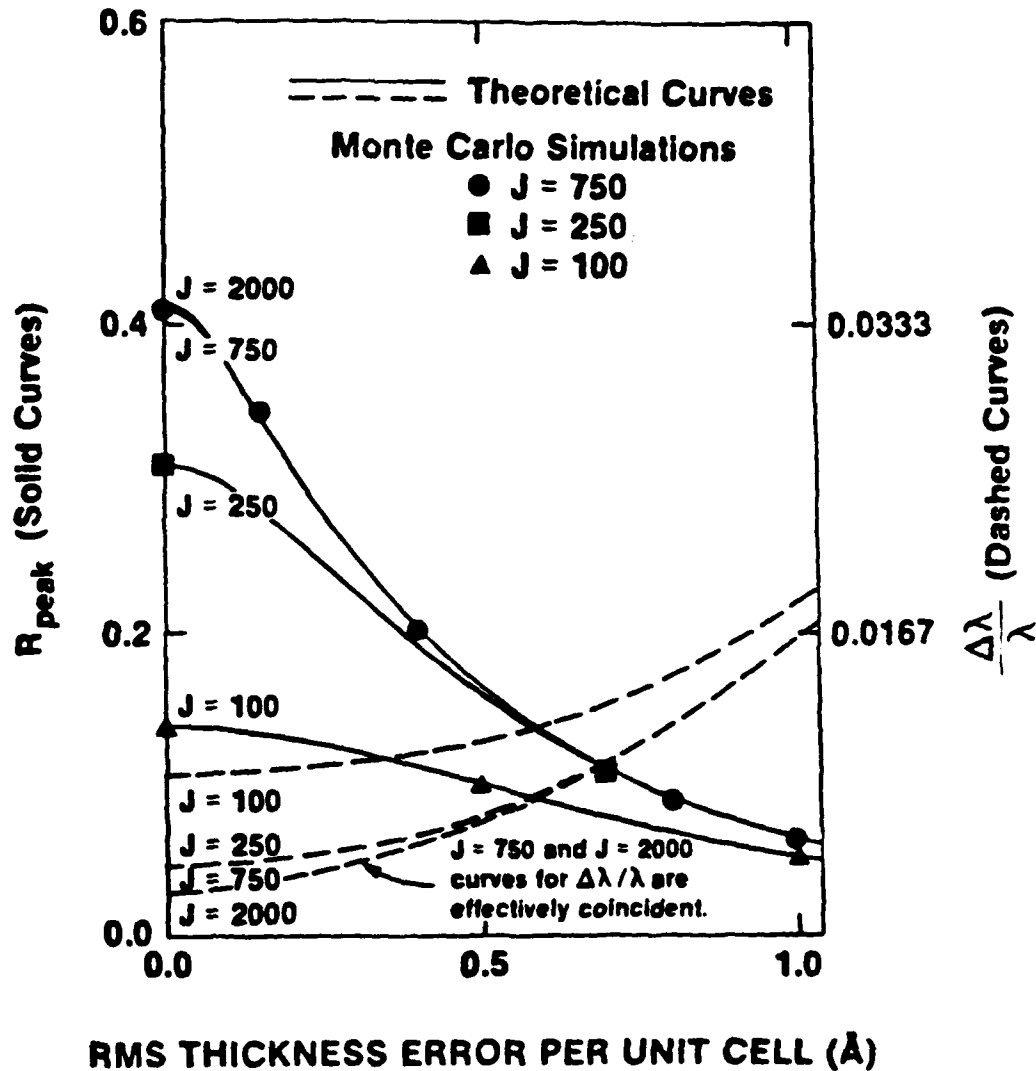
The 6Å to 125Å range covered by Henke's compilation of scattering factors (Henke, et al. 1982) might be considered to represent the full extent of the soft x-ray regime. According to fig. II-2-5, the largest soft x-ray reflectivities that can be attained with tungsten-carbon multilayers are at short wavelengths and at wavelengths just above the carbon-K edge.

Figs. II-5-4 and 5 compare our solution with the results of Monte Carlo simulations in each of these cases. The agreement is quite close; therefore our analysis can be expected to accurately model the effect of random thickness errors in tungsten-carbon multilayers operating at any wavelength in the soft x-ray region, since reflectivities in the region will not be significantly higher than in the two cases considered in figs. II-5-4,5.

The 6Å case cannot easily be simulated at normal incidence because the number of layer pairs required would be impractically large, making the cost in computer time prohibitive. On the other hand, the Monte Carlo program does not implement algorithms for off-normal incidence calculations.

EFFECT OF RANDOM THICKNESS ERRORS TUNGSTEN-CARBON MULTILAYER $\lambda = 44\text{\AA}$

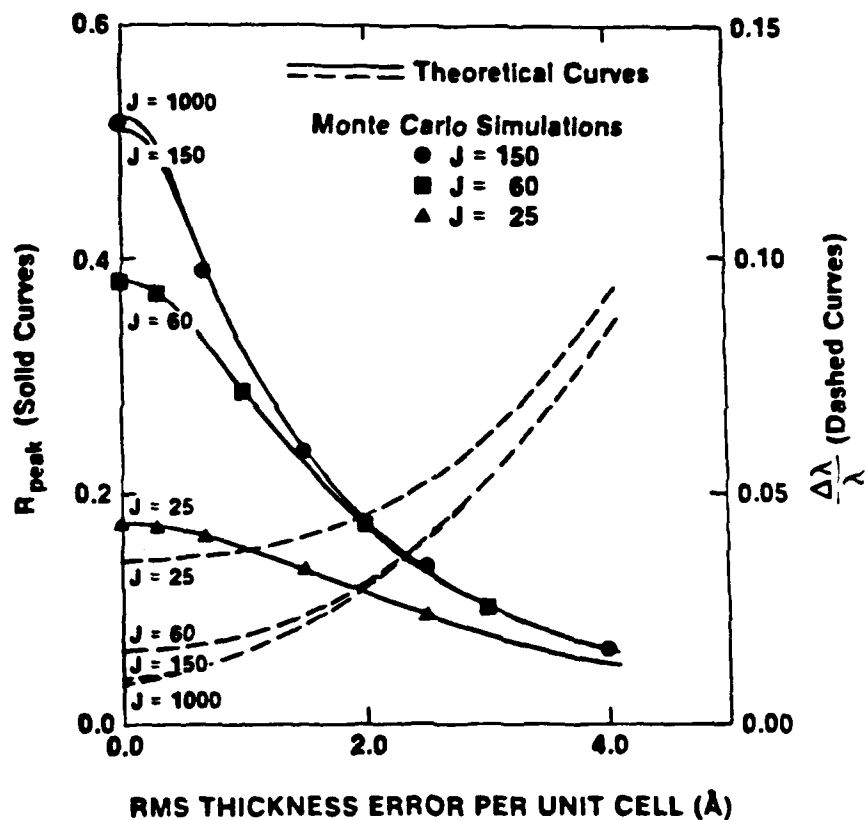
UR
LLE



Plots are for a Tungsten-Carbon multilayer reflecting 44Å radiation at normal incidence.
 $d_w = 3.7\text{\AA}$, $d_c = 18.4\text{\AA}$.

Figure 11-5-4

EFFECT OF RANDOM THICKNESS ERRORS TUNGSTEN-CARBON MULTILAYER $\lambda = 6\text{\AA}$



Plots are for a Tungsten-Carbon multilayer reflecting 6.0\AA radiation at 85° from the normal. $d_w = 5.2\text{\AA}$, $d_c = 32.3\text{\AA}$.

According to eq. II-2-15, the multilayer parameters τ , ρ , and μ scale as $\sec^2 \theta$. Thus, the effect of a non-normal angle of incidence can be simulated by multiplying Δ_L and Δ_H by this factor. In this way fig. II-5-4 simulates reflection of 6\AA radiation from a $2d=75\text{\AA}$ multilayer at an angle $\theta = \arccos(6\text{\AA} / 75\text{\AA}) = 85^\circ$.

The errors introduced with this technique are of order Δ^2 and $q \cdot \Delta$, and so belong to the class of approximations made in sec. II-1. Since these errors include none of the statistical approximations made in the present section, the Monte Carlo results can be considered to be a reasonable test of the statistical assumptions at $\lambda = 6\text{\AA}$.

(Of course, one can simply regard fig. II-5-4 as being based on an artificial example designed to test our result under conditions of high reflectivity).

Part C) Discussion of Solution

We now discuss the general behavior of our result.

From the approximate result of eq. II-5-27, we see that (to the extent that multiple reflections can be neglected), the dephasing $\langle \Delta \phi^2 \rangle$ has an effect on the reflectivity that is roughly similar to the effect of μ'' , i.e. that is similar to the effect of absorption.

In sec. II-2-C we saw that the bandwidth of an undegraded multilayer was of order $2\mu''$. The similarity between the effect of thickness errors and an increase in absorption therefore causes the dependence of $\Delta\lambda/\lambda$ on σ to be approximately parabolic (i.e. linear in $\langle \Delta \phi^2 \rangle$), as shown in figs. II-5-3,5.

In the large σ region where extinction is due primarily to dephasing resulting from thickness errors (i.e. in the region $\langle \Delta \phi^2 \rangle \gg \mu''$), the effective number of layers participating in the coherent reflection process is of order $\langle \Delta \phi^2 \rangle^{-1/2}$, because absorption imposes only a minor constraint on the number of layers involved. The coherent reflectivity in this region should therefore have the approximate form:

$$|\langle \rho \rangle|^2 \sim \left| \langle \Delta \phi^2 \rangle^{-1/2} (r+ip) \right|^2 = \frac{|r+ip|^2}{\langle \Delta \phi^2 \rangle} \quad (\text{II-5-46})$$

which is indeed the limiting behavior of eq. II-5-35.

Thus, the coherent part of the reflectivity $|\langle \rho \rangle|^2$ falls off approximately as σ^{-4} in the limit of large errors.

In this limit the incoherent component $\langle |\bar{\rho}|^2 \rangle$ falls off more slowly, as σ^{-2} (see fig. II-5-1). In the limit of very large errors (i.e. in the region $\langle \Delta \phi^2 \rangle \geq 1$, where our formalism is no longer valid), the incoherent reflectivity can be expected to enter a regime in which the reflections from the individual cells add purely incoherently; in this case the dependence on σ will be determined by the effect of the thickness errors on the reflectivity of individual unit cells.

However, in the regime of interest to us (where $\langle \Delta \phi^2 \rangle \ll 1$), the incoherent beam can be considered to be generated by "packets" of unit cells; the packets are groups of unit cells which have been displaced from their expected phase positions by the accumulation of thickness errors, with the number of unit cells within one packet (this number is $\sim (\langle \Delta \phi^2 \rangle)^{-1/2}$) being such that the cells in the packet still maintain strong coherent interaction with one another. (Thus, by definition the reflectivity of a packet is $\langle \rho \rangle$).

Since $(\tilde{S}'')^{-1}$ is the total number of layers in the structure, eq. II-5-40 represents the incoherent sum of the reflectivities of the packets; i.e. $\langle |\bar{\rho}|^2 \rangle$ is given by the number of packets in the structure multiplied by $|\langle \rho \rangle|^2$.

The incoherent reflectivity will be largest when there is an accumulation of about one radian of dephasing across the effective thickness of the multilayer, so that the size of a packet is comparable to the effective multilayer thickness; this occurs when

$$\langle \Delta \phi^2 \rangle \sim \mu'' \quad (\text{II-5-47})$$

If σ increases beyond this point, the incoherent reflectivity begins slowly to decrease, and the coherent reflectivity begins a very rapid decrease.

Therefore, using eq. II-3-15, we can establish the following tolerance on thickness errors that the multilayer must satisfy in order to have high overall reflectivity:

$$\langle \Delta \phi^2 \rangle \lesssim \mu'' \equiv 4 \times 10^{-6} (2d_{(A)})^2 \quad (\text{II-5-48})$$

or

$$\sigma_{(A)} \lesssim 3 \times 10^{-4} (2d_{(A)})^2 \quad (\text{II-5-49})$$

Thus, there is a variation in sensitivity to thickness errors amounting to approximately two orders of magnitude across the soft x-ray region.

From eq. II-5-43 above, we see that this same criterion can be used to characterize the effect of thickness errors on multilayers operating outside the steady-state regime, except that the fractional fall-off of the reflectivity with σ is slower when $J < (\mu'')^{-1}$; this is because the steady-state regime is reached more rapidly with large σ due to an increase in the imaginary part of the parameter D defined in eq. II-5-43.

II-5-40

D'' may be regarded as a generalized extinction parameter that incorporates the effect of absorption, dephasing due to detuning from the Bragg condition, and dephasing due to thickness errors.

Section II-6: Non-Accumulating Random Thickness Errors

Part A) Introduction

In section II-5 we have analyzed reflection from nominally periodic multilayers that contain accumulating thickness errors. In such multilayers, the target thicknesses for the layers are constant, pre-determined quantities, so any errors made in meeting these target thicknesses will accumulate randomly, resulting in a degradation of reflectivity through the accumulation of dephasing.

On the other hand, when x-ray multilayers are fabricated with ISRM, the target thickness for each high index layer becomes that thickness which will bring reflection from the layer into phase with reflection from the preceeding stack; thereby eliminating the accumulation of dephasing.

Spiller et al. (1980) have verified experimentally that ISRM substantially increases the number of layers that can successfully be fabricated in an x-ray multilayer. While the tolerance on thickness errors is considerably less severe when ISRM is introduced, it is still quite stringent (on an absolute scale) compared to the tolerances which govern optical multilayers.

In this section we analyze the effect of non-accumulating thickness errors. We will find that with this kind of error, the reflectivity loss is due to a degradation in the structure of individual unit cells. Because of this degradation the single-cell reflectivity is reduced by a

Debye-Waller factor; the effect of the errors will also turn out to be similar to that of interlayer diffusion.

In many ways the analysis of non-accumulating errors is a more difficult problem than that of accumulating thickness errors.

First, multilayers fabricated with ISRM are not periodic. Second, with ISRM there is a complicated interaction between a human operator and the multilayer's structure and reflectivity. Third, the wavelength and angle at which the coating is used may not be the same as the wavelength and angle at which the ISRM is performed (see sec. II-4).

Fourth, the error magnitudes of greatest interest in the present case are larger than those of interest in the case of accumulating errors. The a priori assumption of a Gaussian distribution is therefore less reasonable with non-accumulating errors, since the errors may not be small compared to the layer thicknesses. (For example, when the errors are large a Gaussian distribution will imply the existence of layers with negative thickness.) Further, in contrast to the accumulating case, in the present case the reflectivity loss is sensitive to the detailed shape of the probability distribution.

Finally, when ISRM is used we cannot make the usual kind of superposition to treat reflection of unpolarized radiation; the radiation can only be treated as polarized under certain special conditions.

It will only be possible to arrive at fully analytic solutions to the problem of non-accumulating errors under certain special conditions. Nonetheless, the complexity of the numerical computations that must be made in the general case will be reduced to a level similar to that

involved in carrying out the two-by-two optimization procedure described in sec. II-4 (eqs. II-1-20, 4-2, and 4-8).

In particular, the analysis will eliminate the need for expensive Monte Carlo simulations, which in the present case are particularly complicated for the reasons listed above. In the steady-state, the required computation reduces to the solution of at most two coupled algebraic equations, which can (to a fairly good approximation) be solved analytically.

We will use two methods to analyze the problem of non-accumulating errors. The first method will be mathematically quite rigorous as long as certain special conditions obtain. The second method will be more phenomenological, but can be expected to be applicable under a broader range of circumstances than the first method.

Despite the complexity of the problem, we will in each case try to keep the assumptions as simple as possible. The purpose of our analysis is to explore the kinds of behavior that may be encountered in practice, rather than to make strongly quantitative predictions; detailed modeling will be warranted as experimental work in the field becomes more extensive.

Each of our two methods will be based on a stronger version of the key approximation used in the accumulating case, namely that the parameter $\bar{\rho}$ defined in eq. II-5-10 is small compared to one. In the non-accumulating case we will show below that it is permissible to neglect quadratic as well as cubic powers of $\bar{\rho}$.

Since $\tilde{\rho} \ll 1$, it will be possible to set

$$\rho \approx \langle \rho \rangle \quad (\text{II-6-1})$$

(Clearly this is not a good approximation for the first few layers.) We will find that in this one feature the problem of non-accumulating thickness errors is simpler to analyze than that of accumulating thickness errors.

Both methods of analysis will assume for simplicity that the thickness errors obey Gaussian statistics that are independent of K . The analysis can without significant modification be applied to more complicated distributions. Such distributions might, for example, keep the layer thicknesses always positive, or make the RMS errors inversely proportional to the ISRM signal modulation.

Both methods of analysis will assume that a set of target β_n parameters have been obtained in some way (for example, by one of the methods discussed in sec. II-4). We note that even though β_n is nominally the phase thickness of the high index layer, β_n can, as shown in eq. II-2-43, be regarded merely as a division parameter. As such, it can be considered to determine the desired thickness of the low index layer, rather than that of the high index layer, via the relation $\beta_{l,n} \equiv \pi - \beta_{n,n} \equiv \pi - \beta_n$. The reflectivity will be much less sensitive to the thickness ratio than to the total cell

thickness $\pi - \phi_n$.

The final ϕ_n value for each cell will, in the absence of errors in the Kth high index layer, automatically satisfy eq. II-4-2 due to the use of the ISRM technique; this will be true independent of any errors in the preceding layers.

The first, more rigorous analysis will make the following two assumptions in addition to those made above.

First, it will assume that errors occur only when fabricating the low index layers (L layers). This is reasonable because in many cases the oscillations that the ISRM signal will undergo when the L layers are being deposited will be considerably weaker than the oscillations that occur when the high index layers (H layers) are being deposited; this will in turn lead to smaller errors during the H depositions. The L layer signal oscillations will be particularly weak when multilayers having 2 δ -spacings considerably shorter than the carbon-K edge are fabricated, and it is in such short spacing multilayers that thickness errors have their greatest effect. However, we should note that in many cases one might choose the ISRM wavelength to be one which causes a strong contrast during L depositions (Spiller, 1982b).

Another factor that will tend to reduce the magnitude of the errors made in fabricating H layers is that their depositions will be truncated at reflectance maxima; these are comparatively well-defined positions on the ISRM trace.

Depending on the algorithm used to determine the β_s , the desired L truncations may not be as easy for the operator to relate to the ISRM trace, resulting in larger errors during L depositions.

In addition to assuming that the high index errors are negligible, the first method of analysis will assume that the ISRM probe beam can be treated as polarized. This will be strictly valid only if the probe angle is near grazing incidence, near 45° incidence, or near normal incidence. (As a practical matter it is doubtful that the probe θ can be made less than 15° or so).

The second method of analysis will not need to assume either a polarized probe beam or to assume negligible errors in the R layers; it will, however, be less accurate and less rigorous than the first method.

Part B) First method of analysis

If there are no errors in the H layers, we can write the phase thickness of the Kth low index layer as

$$\beta_{L,K} = \beta_{L,K,0} + \xi_K$$

(II-6-2)

$$\langle \xi^2 \rangle = \frac{4\pi^2 \cos^2 \theta}{\lambda^2} \sigma^2$$

where $\xi_K \equiv 2\pi/\lambda \cos \theta f_K$, and the thickness error f_K is a random variable with mean σ that is assumed to obey Gaussian statistics that are independent of K. $\beta_{L,K,0}$ is the desired phase thickness of the Kth low index layer.

We note that eq. II-6-2 will not obtain if there are errors in the H layers, since an error in the K-1st H layer will cause a ξ term with subscript K-1 to be present in $\beta_{L,K}$, due to the automatic error compensation achieved with ISRM.

In the remainder of this section, we will for simplicity's sake suppress the K subscript on all multilayer parameters.

At this point we also introduce the following quantities:

$$\bar{\Delta}_H \equiv \Delta_H \sec^2 \theta$$

$$\bar{\Delta}_L \equiv \Delta_L \sec^2 \theta$$

$$\bar{q} \equiv \bar{\Delta}_H - \bar{\Delta}_L$$

$$\bar{n}_H \equiv 1 + \bar{\Delta}_H$$

$$\bar{n}_L \equiv 1 + \bar{\Delta}_L$$

(II-6-3)

On the grounds that $\tilde{\rho}$ is small, we now set $\rho \equiv \langle \rho \rangle$ in eq. II-4-2 (and so we also set

$$\langle \mathcal{R} \rangle \equiv \langle R e^{-2\mu''} \rangle \equiv |\langle \rho \rangle|^2 \langle e^{-2\mu''} \rangle \text{ and } V_{\rho} \equiv V_{\langle \rho \rangle}).$$

Under the assumption of no errors in the H layers, ϕ_n will still be given by eq. II-4-2 despite the presence of random errors in the L layers. Eq. II-4-2 will now depend on these errors only through the first μ' term and through the μ'' term in the parameter \mathcal{R} .

Since the distinction between R and \mathcal{R} is a higher order effect, the substitution

$$\mathcal{R} = |\langle \rho \rangle|^2 \langle e^{-2\mu''} \rangle \equiv |\langle \rho \rangle|^2 e^{-2\langle \mu'' \rangle} \quad (\text{II-6-4})$$

where $\langle \mu \rangle \equiv \pi \tilde{\Delta}_n - \beta_{i,0} \tilde{q}$, will not effect our result except to order $\phi \cdot \Delta \cdot \xi$.

Then from eq. II-4-2 we can set

$$\phi = \langle \phi \rangle + \xi \frac{\tilde{q}'}{2} + O(\phi \cdot \Delta \cdot \xi) \quad (\text{II-6-5})$$

where

$$\langle \phi \rangle = \frac{1}{2} \left\{ \langle \mu' \rangle + V_{\langle \rho \rangle} - \arctan \left(\frac{1 + |\langle \rho \rangle|^2 e^{-2\mu''}}{1 - |\langle \rho \rangle|^2 e^{-2\mu''}} \tan V_n \right) \right\}$$

(continued on next page)

$$- \arcsin \left(\frac{2 \sqrt{|\langle \rho \rangle|^2 e^{-2\langle \mu'' \rangle}} \sin V_n}{|P(\theta)| \sqrt{1 + |\langle \rho \rangle|^4 e^{-4\langle \mu'' \rangle} - 2|\langle \rho \rangle|^2 e^{-2\langle \mu'' \rangle} \cos 2V_n}} \right) \Bigg\}$$

(II-6-6, continued)

We note that if φ_0 is the the defect-free φ value for the Kth cell, $\langle \varphi \rangle \neq \varphi_0$.

$\langle \varphi \rangle$ must be scaled from the wavelength and angle of the coating's fabrication to the wavelength and angle of the coating's application, if the two are different (i.e. one must set

$$\langle \varphi_2 \rangle = \langle \varphi_1 \rangle \cdot (\lambda_1 \cos \theta_2) / (\lambda_2 \cos \theta_1)).$$

It will then also be necessary to propagate $\langle \rho \rangle$ using eq. II-1-20 in two separate sequences; the first under the fabrication conditions and the second under the application conditions, with the scaled values of $\langle \varphi \rangle$ used in the second sequence. Eq. II-6-5 will then still hold for the second sequence, but the error term of order $\varphi \cdot \Delta \cdot \xi$ will be different.

Next we determine $\langle \beta_n \rangle$ and $\langle t \rangle$. We have

$$\begin{aligned} \beta_n &= \pi - \varphi - \beta_L \\ &= (\pi - \langle \varphi \rangle - \beta_{L,0}) - \xi - \xi \frac{\tilde{q}'}{2} \\ &= \langle \beta_n \rangle - \xi - \xi \frac{\tilde{q}'}{2} \end{aligned} \quad (\text{II-6-7})$$

Similarly

$$\begin{aligned}
 t &\equiv \pi - \beta_L \bar{n}_L - \beta_H \bar{n}_H \\
 &= (\pi - \bar{n}_L \beta_{L,0} - \bar{n}_H \langle \beta_H \rangle) - \frac{\xi}{2} \bar{q}' - i \xi \bar{q}'' \\
 &\equiv \langle t \rangle - \frac{\xi}{2} \bar{q}' - i \xi \bar{q}'' \quad (\text{II-6-8})
 \end{aligned}$$

where again both $\langle t \rangle$ and $\langle \beta_H \rangle$ are ξ dependent.

In Appendix 9 we show that the propagation equation for ρ_n (eq. II-1-20) has the form

$$\begin{aligned}
 \rho_{n+1} &= e^{-2it_n} \rho_n \\
 &- i e^{-it_n} P(\theta) (\bar{\Delta}_H \sin \beta_H e^{-i\beta_L} + \bar{\Delta}_L \sin \beta_L e^{i\beta_H}) \\
 &- i e^{-3it_n} P(\theta) (\bar{\Delta}_H \sin \beta_H e^{i\beta_L} + \bar{\Delta}_L \sin \beta_L e^{-i\beta_H}) \rho_n^2
 \end{aligned} \quad (\text{II-6-9})$$

in the bilayer case. To derive eq. II-6-9 we have used the definitions in eq. II-1-15 to recalculate the quantities in eq. II-2-15 under a non-centrosymmetric geometry (L layer on substrate side, H layer on incident side), and have retained terms of order $\varphi \cdot \Delta$, which are neglected in eq. II-2-15.

Assuming Gaussian statistics, we have from eqs. II-6-8 and 5-6

$$\begin{aligned}
 \langle e^{-2it} \rangle &= e^{-2i\langle t \rangle} \langle e^{i\xi(\tilde{q}' - 2i\tilde{q}'')} \rangle \\
 &= e^{-2i\langle t \rangle} e^{-\frac{\langle \xi^2 \rangle}{2} (\tilde{q}'^2 - 4i\tilde{q}'\tilde{q}'' - 4\tilde{q}''^2)} \\
 &= e^{-2i\langle t \rangle} + O(\Delta^2)
 \end{aligned}
 \tag{II-6-10}$$

(Here we have used the same identity as is used in eq. II-5-8, which can be shown to hold even when the random variable in the exponent is multiplied by a complex coefficient).

We can now set the expectation value of the first term on the right of eq. II-6-9 equal to

$$e^{-2i\langle t \rangle} \langle \rho \rangle^2 \tag{II-6-11}$$

In order to calculate the expectation value of the remaining terms in the equation, we must determine the quantities:

$$\begin{aligned}
 &\langle \sin \beta_n e^{-i\beta_n} e^{-it} \rangle \\
 &\langle \sin \beta_n e^{i\beta_n} e^{-it} \rangle \\
 &\langle \sin \beta_n e^{i\beta_n} e^{-3it} \rangle \\
 &\langle \sin \beta_n e^{-i\beta_n} e^{-3it} \rangle
 \end{aligned}
 \tag{II-6-12}$$

II-6-12

Beginning with the first quantity in eq. II-6-12, we expand $\sin \beta_n$ into exponentials, and first calculate

$$\langle e^{i\beta_n} e^{-i\beta_L} e^{-it} \rangle \quad (\text{II-6-13})$$

Using eqs. II-6-2, 7, and 8, we can set

$$\beta_n - \beta_L - t = \langle \beta_n \rangle - \beta_{L,0} - \langle t \rangle - 2\xi - \xi i \tilde{q}'' \quad (\text{II-6-14})$$

so that under Gaussian statistics

$$\langle e^{i\beta_n} e^{-i\beta_L} e^{-it} \rangle = e^{i\langle \beta_n \rangle} e^{-i\beta_{L,0}} e^{-i\langle t \rangle} e^{-2\langle \xi^2 \rangle (1-i\tilde{q}'')} + O(\Delta^2) \quad (\text{II-6-15})$$

Through similar steps the remaining quantities in eq. II-6-12 are readily obtained. Neglecting quadratic and higher terms in \tilde{q} , and neglecting terms of order Δ^2 , we obtain for the expectation value of eq. II-6-9

$$\begin{aligned}
\langle p_{n+1} \rangle &= e^{-2i\langle t \rangle} \langle p_n \rangle \\
&- \frac{P(\theta)}{2} e^{-i\langle t \rangle} \left[\tilde{\Delta}_n e^{-i\beta_{1,0}} (e^{i\langle \beta_n \rangle} e^{-2\langle \zeta^2 \rangle} - e^{-i\langle \beta_n \rangle}) \right. \\
&\quad \left. + \tilde{\Delta}_1 e^{i\langle \beta_n \rangle} (e^{i\beta_{1,0}} - e^{-i\beta_{1,0}} e^{-2\langle \zeta^2 \rangle}) \right] \\
&- \frac{P(\theta)}{2} e^{-3i\langle t \rangle} \langle p_n \rangle^2 \left[\tilde{\Delta}_n e^{i\beta_{1,0}} (e^{i\langle \beta_n \rangle} - e^{-i\langle \beta_n \rangle} e^{-2\langle \zeta^2 \rangle}) \right. \\
&\quad \left. + \tilde{\Delta}_1 e^{-i\langle \beta_n \rangle} (e^{i\beta_{1,0}} e^{-2\langle \zeta^2 \rangle} - e^{-i\beta_{1,0}}) \right]
\end{aligned}$$

(II-6-16)

We can now propagate $\langle \rho \rangle$ through the stack using eqs. II-6-6, 7, 8 and 16. Since $\tilde{\rho} \ll 1$, we can set $\langle R \rangle = |\langle \rho \rangle|^2$ to obtain the intensity reflectance. This is as far as we can proceed towards a fully analytic solution outside the steady-state regime. In the steady-state regime, eqs. II-6-6 and 16 reduce to two coupled algebraic equations, which can be rapidly solved by an iterative procedure in which $\langle \varphi \rangle$, $\langle t \rangle$, and $\langle \beta_n \rangle$ are initially set equal to their defect-free values.

Part C) Second method of analysis

A comparison of eq. II-6-16 with eq. II-6-9 shows three ways in which non-accumulating errors manifest themselves: first, in the difference between the expectation values of the parameters φ , β_n , and t , and the defect-free values of these parameters; second, in the difference between φ and its expectation value; and third, in a direct way through the presence of the Debye-Waller factors $\exp(-2 \langle \xi^2 \rangle)$.

In our second analysis we will treat the first of these effects as negligible. In essence we will assume that the ISRM technique keeps the total phase thickness of each cell a constant; in other words, we assume that each H layer thickness is made by the ISRM technique to compensate for any OPD error present in the preceding L layer. (To within order $\xi \cdot \Delta$, we can also set the optical path difference equal to the physical path difference. After the expectation value is taken, the error in such a substitution will always be found to be of order $\Delta^2 \langle \xi^2 \rangle$).

With the second method of analysis we can treat the possibility of errors in the H layers as well. In order to do so, we go to a quasi-centrosymmetric decomposition in which the cell interfaces lie within the low index layers. (The decomposition reduces to that shown in fig. II-2-1 in the absence of errors). We define these fictitious interfaces to occur at the same physical heights above the substrate as would the midpoints of the low index layers in the absence of errors; thus the interfaces that divide the cells do not change positions in the presence of errors.

The errors do cause shifts in the the positions of the physical interfaces that separate the H and L layers. We will measure these shifts relative to the defect-free positions of the physical interfaces.

Finally, we will assume that these shifts of the physical layer interfaces can be treated as uncorrelated Gaussian random variables. This is suggested by the Debye-Waller factors in eq. II-6-16, which, as we will see, represent degradations in the reflectivity of individual interfaces due to displacements whose magnitudes have a Gaussian distribution. However, we should note that this assumption is not strictly consistent with the results of part B. For simplicity we will also neglect terms of order $\phi \cdot \Delta$ in our second analysis. The algebraic details of the derivation are given in Appendix 11.

There we show that

$$\begin{aligned} \langle p_{n+1} \rangle &= e^{-2it_0} \langle p_n \rangle \\ &\quad - \frac{\tilde{q}}{2} \left(e^{i\beta_{n,0}} e^{-2\langle \xi_n^2 \rangle} - e^{-i\beta_{n,0}} e^{-2\langle \xi_n^2 \rangle} \right) \\ &\quad - \frac{\tilde{q}}{2} \langle p_n \rangle^2 \left(e^{i\beta_{n,0}} e^{-2\langle \xi_n^2 \rangle} - e^{-i\beta_{n,0}} e^{-2\langle \xi_n^2 \rangle} \right) \end{aligned} \quad (\text{II-6-17})$$

where

$$\begin{aligned} \sqrt{\langle \xi_n^2 \rangle} &\equiv \frac{2\pi}{\lambda} \cos \theta \sigma_n \\ \sqrt{\langle \xi_l^2 \rangle} &\equiv \frac{2\pi}{\lambda} \cos \theta \sigma_l \end{aligned} \quad (\text{II-6-18})$$

Here σ_L and σ_H are the standard deviations of the errors in the L and H layers, and t_0 , $\beta_{n,0}$, and $\beta_{L,0}$ are the defect-free values of the parameters t , β_n , and β_L . Except for the non-centrosymmetric geometry and the non-zero errors in the H layers, our result is equivalent to eq. II-6-16 with the expectation values of the parameters φ , t , and β_n set equal to their defect-free values, and with terms of order $\varphi \cdot \Delta$ neglected.

We also find that, to an approximation, $\langle |\tilde{\rho}|^2 \rangle$ in the steady-state is given by

$$\begin{aligned} \langle |\tilde{\rho}|^2 \rangle = Q \left\{ 8 \langle \xi^2 \rangle |\langle \rho \rangle|^2 + e^{-2\langle \xi^2 \rangle} \times \right. \\ \left[\sinh 2\langle \xi^2 \rangle - 4 \cos \beta_{n,0} \langle \xi^2 \rangle \operatorname{Re}(\langle \rho \rangle) (1 + 2|\langle \rho \rangle|^2) \right. \\ \left. \left. + 2 \sinh 2\langle \xi^2 \rangle \cos 2\beta_{n,0} e^{-4\langle \xi^2 \rangle} \operatorname{Re}(\langle \rho \rangle^2) \right] \right\} \end{aligned}$$

(II-6-19)

where

$$Q = \frac{|\bar{q}|^2}{4(\mu_0'' - e^{-2\langle \xi^2 \rangle} \operatorname{Im}(\tau_0 \langle \rho \rangle))} \quad (\text{II-6-20})$$

(This assumes, for purposes of illustration, that $\xi_1 = \xi_n \equiv \xi$. See below). Thus,

$$\langle |\tilde{\rho}|^2 \rangle \sim \alpha \sim \Delta \ll 1 \quad (\text{II-6-21})$$

as assumed earlier. In our 67.6A standard example (see sec. II-5), with no errors in the H layers, $\langle |\tilde{\rho}|^2 \rangle$ reaches its largest value in the steady-state regime with $\sigma \geq 5\text{\AA}$; in this regime $\langle |\tilde{\rho}|^2 \rangle = 0.004$. The physical reason for the small size of $\langle |\tilde{\rho}|^2 \rangle$ is discussed below.

In the second analysis, the polarization of the ISRM probe enters indirectly via the defect-independent parameters φ_0 . These parameters are obtained by making a defect-free propagation of $\langle \rho \rangle$ using eq. II-6-9, with eq. II-4-2 (in S or P polarization) used to determine φ_0 .

The φ_0 parameters are polarization dependent, and so eq. II-4-2 will not apply to an unpolarized ISRM beam except under special conditions. However, since only the defect-free case need be considered at this point, it would be computationally quite rapid to determine the φ_0 values by numerical optimization.

As an alternative, since our approach in this second analysis is somewhat phenomenological, we will consider it adequate to determine each φ_0 value using a weighted average,

$$\varphi_{\text{unpol},0,n} \approx \frac{R_{n-1,S} \varphi_{S,0,n} + R_{n-1,P} \varphi_{P,0,n}}{R_{n-1,S} + R_{n-1,P}} \quad (\text{II-6-22})$$

with $\varphi_{s,0}$ and $\varphi_{p,0}$ given by eq. II-4-2 in each of the two polarizations. In the defect-free calculation φ_s and φ_p must be propagated using eq. II-6-17 in separate sequences, but in each sequence the $\varphi_{0,n}$ value used must be that given by eq. II-6-22.

If necessary the resulting φ_0 values can then be scaled to the wavelength and angle of the coating's application; $\langle \rho \rangle$ can then be re-propagated in each polarization, and the final intensity reflectances averaged.

Part D) Discussion

As in section II-5 we have used a Monte Carlo simulation to test the accuracy of our theoretical treatment. In order to be able to compare both methods of analysis, we have only considered cases that satisfy the restricted conditions under which our first method of analysis can be applied (see part A above).

Our Monte Carlo simulation program has no off-normal incidence capability, so we have used a normal incidence ISRM geometry in our simulations.

As discussed in sec. II-5-C, the non-normal incidence case can be reduced to the normal incidence case by using a $\sec^2 \theta$ scaling of Δ_{\parallel} and Δ_{\perp} , as long as the ISRM beam can be treated as polarized. (See part A above. The error involved in assuming a $\sec^2 \theta$ scaling should not involve the statistical kinds of approximations made in this section.)

However, we note that in the non-accumulating case, the unpolarized reflectivity can only be treated as the mean of the reflectivities of the orthogonal polarizations under the simple model of part C.

We have also chosen to have the Monte Carlo program prohibit layers with negative thickness; when the Gaussian random number generator forces such a thickness, the thickness is set to zero instead.

Our theory could model this restriction by using the appropriate non-Gaussian probability distribution for the errors, but we have intentionally left this discrepancy unresolved since the discrepancy is somewhat representative of the kind of oversimplification that modeling of this complex problem must necessarily have.

Fig. II-6-1 shows the expectation of R plotted over a range of values from zero to $\sim \langle d_L \rangle / 3$. (Even at $\sigma = \langle d_L \rangle / 3$, the fraction of layers under a Gaussian distribution that will have negative thickness is fairly small.) The solid curve is calculated by the method of part B, the dashed curve by the method of part C.

The Monte Carlo results in fig. II-6-1 have been obtained using the exact, non x-ray characteristic matrix solution of eq. II-1-22. The H layer truncations were determined by numerical solution for the reflectance maximum at each K value, in each simulated stack.

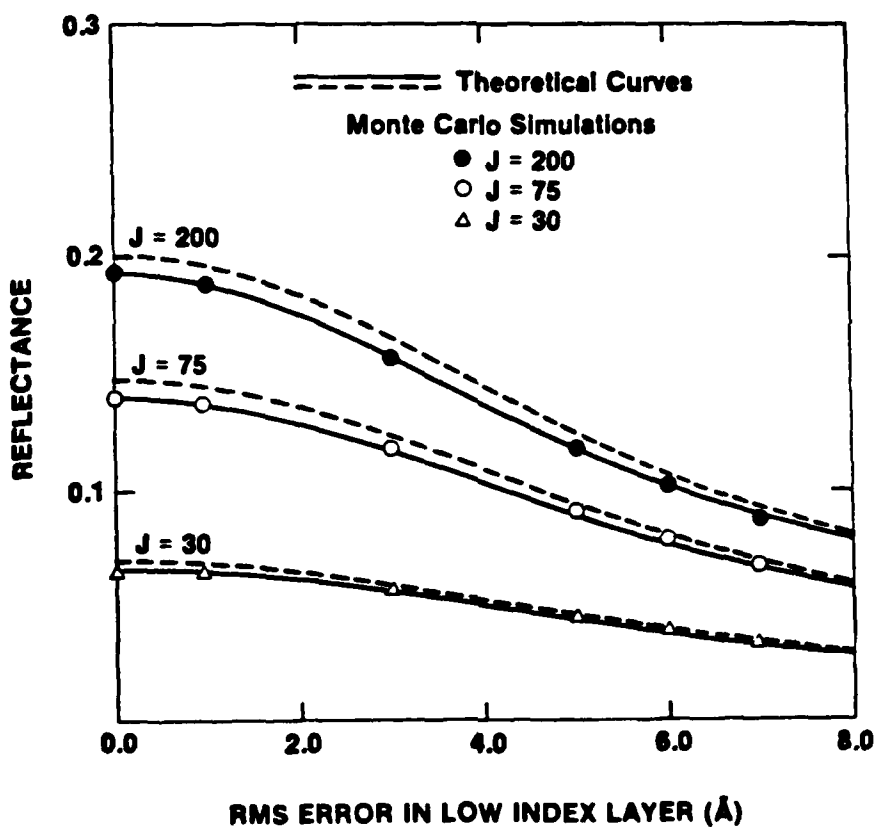
Prior to constructing the simulated stacks that contain thickness errors, the program constructs a defect-free stack that is optimized in a two-by-two fashion (see sec. II-4), with the optimization performed numerically. The purpose of this initial optimization is to obtain the defect-free β_K division parameters, which determine the target L layer truncations. As discussed above, our equations can be used with a set of β_K division parameters obtained by any method.

As discussed in part A, one could easily justify adopting a more complicated model for both the Monte Carlo simulation and the theoretical analysis, but in this preliminary work we have used only the minimal set of assumptions discussed above.

As the figure shows, the agreement between the two methods of analyses and the Monte Carlo simulations is quite good, with the first analysis being somewhat more accurate than the second. We estimate the error due to the finite sample size to be about $\pm .001$. The two theoretical calculations disagree at $\sigma = 0$ due to neglect of terms of

**EFFECT OF NON-ACCUMULATING
THICKNESS ERRORS
(Tungsten-Carbon Multilayer made with ISRM)**

UR
LE



Plots are for a W/C multilayer reflecting 67.6 Å radiation at normal incidence. $d_w = 7.6$ Å, $d_c = 26.5$ Å.

X369

Figure II-6-1

order $\varphi \cdot \Delta$ in the method of part C.

Both analyses depart somewhat from the simulations at large σ values, perhaps because of the positive layer thickness constraint that we have placed in the simulation program. We should mention at this point that at large σ values, the second method of analysis will not always track the more rigorous solution of eq. II-6-16 as closely as it does in our standard 67.6Å example; in fact it is even possible in some cases for the second solution to predict an increase in reflectivity as σ increases. This can occur only when the nominal H layer thickness is sufficiently small and σ sufficiently large that, under the simple model of part C, the H thickness can frequently become negative. The simple model can then also predict an increase in single-cell reflectivity as σ increases, without an increase in absorption, leading to an increased reflectivity for the stack as a whole.

In contrast to the similar situation that occurs with the L layers, it would not be valid to correct for this effect by going to a non-Gaussian distribution, since the effect is an artifact intrinsic to the system of cell decomposition that we use in our in our second method of analysis.

However, we have always found the second solution to be accurate in the region of small and moderate σ values.

We now proceed to discuss our solution in physical terms. In order to do so we take our less rigorous solution in eq. II-6-17, and let the total number of layers J (and therefore the relevant values of K) become sufficiently large that the multilayer operates in the steady-state regime and becomes periodic.

We also assume somewhat arbitrarily for purposes of discussion that the errors in the high and low index layers have equal RMS magnitudes.

We then obtain from eq. II-6-17

$$R \equiv |\langle \rho \rangle|^2 = \left| \frac{r_0 e^{-2\langle \xi^2 \rangle}}{\sqrt{t_0^2 - r_0^2 e^{-4\langle \xi^2 \rangle}} - t_0} \right|^2$$

(II-6-23)

(This may be regarded as an approximate analytic solution to the two coupled algebraic equations that our first method of analysis reduces to in the steady-state. We also note that it is not necessary to assume equal L and H errors in order to arrive at an analytic steady-state solution.)

Eq. II-6-23 is simply a standard Darwin-Prins solution (see eq. II-2-11) with the single cell reflectivity ir_0 degraded by a Debye-Waller factor.

To an extent the presence of a Debye-Waller factor is not surprising. In x-ray diffraction such factors result when the phase position of a scatterer is randomly displaced according to a Gaussian distribution (usually due to thermal motion, see James, 1965, p.193). The Debye-Waller factor may be regarded either as the Fourier transform of a Gaussian distribution, or as the expectation of a complex exponential whose amplitude obeys Gaussian statistics.

The central principle of x-ray diffraction states that when extinction can be ignored, the amplitude reflected from a sample will be the Fourier transform of the diffracting structure. (This is of course the basis by which x-ray diffraction is used to determine the structure of quasi-periodic objects.)

In the present case extinction and multiple reflections cannot be neglected except within individual unit cells; thus only the unit cell reflectivity in eq. II-6-23 is multiplied by a Debye-Waller factor.

However, there is a more subtle feature present in our result, in that eq. II-6-23 has the standard Darwin-Prins form. This implies that the total interaction of the different cells in the multilayer is no different from the interaction that the corresponding set of "averaged" cells would have in the absence of errors; this is true despite the presence of extinction and multiple reflections, which must be considered in the structure as a whole.

This point can be clarified by considering the similarity between non-accumulating thickness errors and interlayer diffusion. We will continue to consider only the simple case where the multilayer has equal L

and H layer errors (or diffusion profiles), is periodic, and operates in the steady-state. (We should also note that interlayer diffusion has been analyzed by Underwood and Barbee (1982); their treatment is discussed briefly in sec. IV-1).

According to eq. II-1-15, the parameters r and μ are essentially (truncated) Fourier transform components of the structural profile $\Delta(z)$.

If we model the diffusion process as a convolution of the sharp-interface $\Delta(z)$ function with some smoothening function, then r and μ will be multiplied by the appropriate Fourier transform components of the smoothening function. (Since r and μ are actually truncated Fourier components, the preceding argument is somewhat oversimplified, but in Appendix 12 we show that the result is still correct). Since μ is the DC component of the transform, it is unchanged by diffusion if the diffusion profile is correctly normalized. Thus, neither interlayer diffusion nor non-accumulating errors will change the (average) transmittance of the cell.

However, if the diffusion profile is the same normalized Gaussian function as the Gaussian probability distribution used in our analysis of non-accumulating errors, the diffusion will cause r to be multiplied by the same Debye-Waller factor that appears in eq. II-6-23.

Application of the Darwin-Prins solution of eq. II-2-11 to the diffusion problem then yields a solution identical to that in eq. II-6-23 for non-accumulating errors. The two solutions remain identical when generalized to allow for unequal RMS errors or diffusion profiles in the

L-H and H-L interfaces.

This identity of results implies that the randomly varying unit cells in the stack interact together in the same way as do a corresponding set of cells having an averaged (or diffused) structure.

This behavior is a consequence of the small magnitude of $\tilde{\rho}$. This can be seen by considering the step in the analysis where we take the expectation value of eq. II-6-9 while neglecting $\tilde{\rho}$; since $\tilde{\rho}$ is neglected $\langle \rho \rangle$ is propagated only by the averaged or expectation values of the cell structure. Under the simple model of part C, the averaging is represented by the Debye-Waller factors.

Thus, as long as the multilayer contains at least a few layers, it need not really be treated as a random structure except to the trivial extent of diffusing the cell structure. (This is only true within the simple model of part C, of course). In a sense the ISRM technique may be said to suppress the randomness by eliminating the accumulation of dephasing.

Physically, $\tilde{\rho}$ is small in the non-accumulating case because the components reflected from the different interfaces are uncorrelated with one another, and so, in fact, add together only incoherently.

Since incoherent reflection is inherently a weak process in the x-ray regime, the overall $\tilde{\rho}$ component is small; thus in eq. II-6-19 $\langle |\tilde{\rho}|^2 \rangle$ is of the order of the intensity reflectance of each cell multiplied by the total number of cells (rather than by the square of the total number of cells as would be the case with coherent reflection).

In contrast, in the case of accumulating errors the displacements are well-correlated from one interface to the next, with the correlation between displacements vanishing only between one "packet" and the next (see sec. II-5). The packet as a whole will radiate in a primarily incoherent way; however within the packet the cells interact coherently, making the overall incoherent reflectivity $\tilde{\rho}$ considerably larger than in the non-accumulating case.

In the accumulating case $\langle \rho \rangle$ and $\tilde{\rho}$ are therefore strongly interconnected, and so there is no simple, non-stochastic analogue for accumulating random thickness errors; in contrast, as we have seen there is a straightforward analogy between non-accumulating thickness errors and interlayer diffusion.

The scaling of accumulating and non-accumulating errors with $2d$ -spacing is also different. In order for the Debye-Waller factor to depart significantly from one

$$2 \left(\frac{2\pi}{\lambda} \cos \theta \sigma \right)^2 \geq \ln 2 \quad (\text{II-6-24})$$

or

$$\sigma \lesssim 0.1 \times (2d) \quad (\text{II-6-25})$$

II-6-28

This may be compared to the corresponding result in eq. II-5-62 for accumulating errors. In each formula σ should be regarded as the total RMS error per cell, rather than per layer.

Chapter III Applications of X-Ray Multilayer Coatings

Section III-1 - General Considerations

Part A) Introduction

In this chapter we discuss possible applications for x-ray multilayers in terms of the theory developed in chapter II. We will concentrate on two applications that are of current interest at the Laboratory for Laser Energetics of the University of Rochester; however, we will first discuss some points of general relevance concerning the performance of multilayers in the x-ray region.

In sec. III-2 we will then discuss the possibility of using multilayers to form cavity mirrors for projected x-ray lasers (wavelength of order 100\AA). In sec. III-3 we will discuss the use of multilayers in short wavelength x-ray microscopy (wavelength of order 1\AA).

Part B) General Constraints on Multilayer Performance

The results of secs. II-2 and 3 show that the reflecting performance of x-ray multilayers is strongly limited by absorption and by the weak interaction of the layer materials with the incident beam.

According to figs. II-2-4 and 5, absorption will limit the reflectivities of multilayers to at most 0.8, and much poorer reflectivities will be typical in most of the soft x-ray spectrum unless new materials combinations prove feasible.

In sec. II-3 we have shown that x-ray multilayers have a very narrow bandwidth as a result of the weak coupling between the structure and the radiation. This makes very difficult the development of x-ray optical components that are achromatic or wide-field. (However, the spectral selectivity of x-ray multilayers may be useful in certain applications, see below).

Eq. II-3-39 suggests that centered optical systems of moderately high aperture can be devised for the long wavelength region around 100\AA . The strongest drawback to such systems may be the limitation that absorption will impose on the total number of reflecting surfaces.

As the wavelength falls below about 100\AA , either the angle of incidence to the surface or the 2d-spacing must be reduced; according to eq. II-3-21 the aperture and field-of-view of a coated x-ray optical element must then decrease.

As the wavelength is decreased still further, the necessity of maintaining layer thicknesses of at least a few angstroms will require that the multilayers operate very far from normal incidence; according to

eq. II-3-23 the largest possible fields of view will then be obtained at angles as close as possible to the surface.

The geometrical aberrations in such highly decentered systems will then impose additional constraints on field of view.

So far we have only discussed the limitations on performance that are imposed by materials properties. Experimental observation shows that the reflectivities of multilayers fabricated with present technology are usually somewhat lower than those of an ideal structure, although uncertainty in the optical constants makes such a conclusion difficult to establish unambiguously. Fairly good agreement with theory can be obtained when the theory makes provision for defects in the multilayer structure (Haelbich, Segmuller, and Spiller, 1979; Barbee, 1982).

We now discuss published experimental results in order to gauge their implications for practical devices.

Multilayer reflectivity generally drops off rapidly when the 2d-spacing is reduced below 40 or 50 Å. The measured performance also generally comes closer to the defect-free value under short wavelength (~ 1.5 Å) illumination at glancing angles, than otherwise.

To date there have only been tentative attempts to compare the observed degradation to theoretical models, and only the simplest degradation model has been considered. Haelbich, Segmuller, and Spiller (1979); and Barbee (1982), have each attempted to model their experimental results with an expression of the form

$$R(\sigma) = \left| \rho_{\text{Ideal}} \cdot e^{-2 \left(\frac{2\pi\sigma \cos\theta}{\lambda} \right)^2} \right|^2$$

$$= R_{\text{Ideal}} \cdot e^{-\frac{16\pi^2 \sigma^2 \cos^2 \theta}{\lambda^2}} \quad (\text{III-1-1})$$

Multiplication of the entire multilayer reflectivity by such a Debye-Waller factor (rather than the individual interfacial reflectivity as in sec. II-6), has been shown by Eastman (1978) to correspond to what he calls the identical film model of roughness, in which some particular roughness profile (generally that of the substrate) is replicated identically in all succeeding layers.

The problem of multilayer roughness is potentially a very complicated one, since there is an enormous range of possible statistical magnitudes and correlations for the roughness, with varied correlations being possible both within each layer, and across the different layers. Further, the analysis of roughness will in general require the solution of a three-dimensional electromagnetic problem.

We will describe our own initial investigation of multilayer roughness in the section of chapter IV that deals with future work; the simple, limiting case models that we analyze there may prove useful in planning the kind of detailed experimental investigation of the reflecting performance of multilayers that will be necessary to characterize their structures in detail. In chapter IV we briefly describe certain characteristic signatures in multilayer reflecting properties that defects of different kinds (including various kinds of roughness) will produce. However, the experimental results published to date appear to permit only limited interpretation.

Barbee (1982) has fit the Debye-Waller factor of eq. III-1-1 to several measurements of peak reflectivity made in first order at 1.54\AA with multilayers having a variety of 2d-spacings. (See his fig. 7. Note that

in this figure, the solid curve is an interpolation between experimental points, rather than a theoretical calculation.) Barbee has used four data points in his fit to eq. III-1-1, and has obtained a final RMS error of $\pm 5\%$. (The best-fit value of σ was 3.15\AA). The experimentally observed fall-off is slightly sharper than that predicted by eq. III-1-1. (We should note that Barbee's multilayers probably do not contain enough layers to operate in steady-state).

Unfortunately, the sensitivity of multilayer reflectivity to any of the various degradation mechanisms considered in chapter II will have a dependence on 2d-spacing that is similar to that of eq. III-1-1.

For example, multilayer reflectivity in the presence of either interlayer diffusion, non-accumulating thickness errors, or the kind of roughness that we term "smoothing films" (see chapter IV) will, in the steady-state, be approximately given by (here reproduced from eq. II-6-23)

$$R = \left| \frac{\tau_0 e^{-2\langle \xi^2 \rangle}}{\sqrt{t_0^2 - \tau_0^2 e^{-4\langle \xi^2 \rangle}} - t_0} \right|^2 \quad (\text{III-1-2})$$

where $\sqrt{\langle \xi^2 \rangle} = 2\pi\sigma \cos \theta / \lambda$.

Eq. III-1-2 has the same similarity in shape to eq. III-1-1 that the Darwin-Prins solution of eq. II-2-11 bears to our approximate solution in eq. II-3-1. Thus, it will usually be difficult to experimentally distinguish the two kinds of structural defects by varying the 2d-spacing.

particularly with a small number of data points, and with the Debye-Waller coefficient serving as an adjustable parameter.

Other kinds of multilayer defects will also resemble the dependence of eq. II-1-1, at least qualitatively.

For example, we find from eqs. II-5-27 and 3-15 that accumulating errors will have a dependence on $2d$ -spacing of the approximate form:

$$R(d) = R_{\text{Ideal}} \cdot \frac{1}{\left(1 - \frac{A}{d^4}\right)^2} \quad (\text{III-1-3})$$

where A is independent of the spacing.

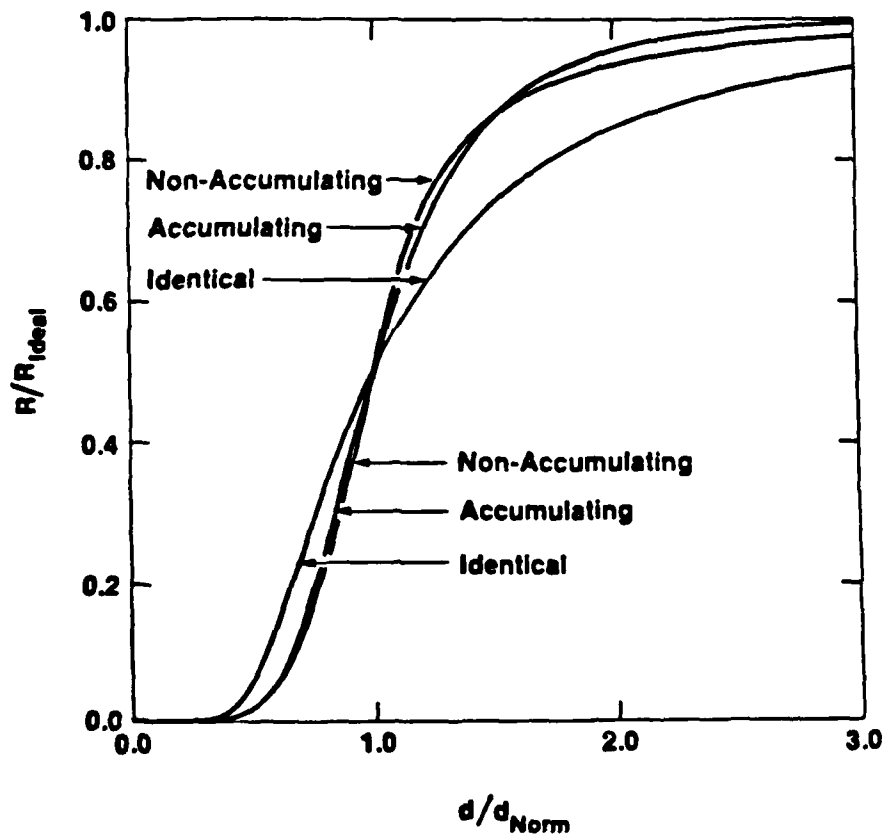
This function will have a slightly sharper fall-off than eq. III-1-1 in the soft x-ray regime, but will have a slightly more-rounded toe. Accumulating errors will produce a greater change in bandwidth than will non-accumulating errors.

Eqs. III-1-1, 2 and 3 are compared in fig. III-1-1; in each equation the σ value has been chosen to make the degradations equal to 0.5 at a common d -spacing (d_{Norm}). The optical constants used in eq. III-1-2 are those of tungsten and carbon at $\lambda = 1.66\text{\AA}$ (comparable to Barbee's wavelength of 1.54\AA).

The near coincidence of these curves shows the difficulty in trying to use the dependence of reflectivity on $2d$ -spacing to determine the nature of the structural defects in multilayers.

SCALING OF REFLECTIVITY DEGRADATION WITH 2d-SPACING

UP
LLE



X363

Figure III-1-1

To date there has been one direct experimental indication that roughness has a detectable effect on multilayer reflectivity; Spiller et al. (1980) have found that the measured reflectivity of a 55 layer gold-palladium/carbon multilayer is increased if the detector aperture is increased, indicating that the reflected beam contains scattered radiation.

We might mention that at short x-ray wavelengths, the onset of reflectivity loss predicted by eq. III-1-2 will become somewhat sharper than the onset at longer wavelengths. The presence of structural defects satisfying this equation might then explain why moderate 2d-spacing multilayers tend to have short wavelength reflectivities that are closer to the defect-free values than are the reflectivities at longer wavelengths.

Haelbich, Segmuller, and Spiller (1979) have made use of a multidimensional optimization code that numerically determines the particular thicknesses for each of the layers in a multilayer, and the particular complex indices of refraction, that will produce the best agreement with a measurement of reflectivity versus θ under monochromatic illumination. A Debye-Waller coefficient then forms a final degree of freedom. The agreement achieved is moderately good (see their fig. 3), but with so many free parameters, it is difficult to judge how reliable a test this is of the assumed degradation model.

In chapter IV we will discuss briefly the kinds of measurements with which one might characterize the structural defects in multilayers. For the moment we draw one important conclusion from existing experimental work, namely that x-ray multilayers can be expected to show a rapid loss in reflectivity when the 2d-spacing drops below about 40\AA .

Such a degradation is not surprising. According to eq. II-6-25, an interfacial gradient with a characteristic depth of order 4\AA will cause a factor of two reflectivity loss in a multilayer having a $2d$ -spacing of 40\AA .

One might consider such a fall-off in reflectivity to be essentially inevitable, since an interface cannot be sharp on a sub-atomic scale.

While this may prove to be correct as a practical matter, we might note that there are x-ray crystallographic arguments which suggest that the ultimate limit imposed by atomic structure on $2d$ -spacing is actually much smaller. Under a classical atomic model, the gradient in the atomic electron density distribution causes a fall-off in the atomic scattering factor; this fall-off is usually measured in terms of the quantity $\sin \theta / \lambda$ (see James, 1965, chapter III, for a discussion of these concepts). The fall-off typically becomes pronounced when $\sin \theta / \lambda \sim 0.5\text{\AA}^{-1}$ (i.e. $2d = 2\text{\AA}$).

AD-A136 306

DEVELOPMENT OF X-RAY LASER MEDIA MEASUREMENT OF GAIN
AND DEVELOPMENT OF C..(U) ROCHESTER UNIV N Y LAB FOR
LASER ENERGETICS J FORSYTH FEB 83

33

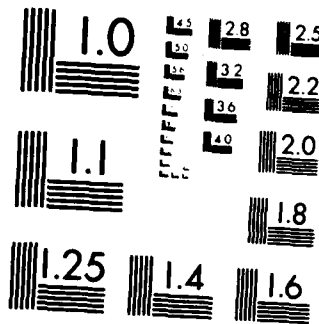
UNCLASSIFIED

AFOSR-TR-83-1136-VOL-2 AFOSR-81-0059

F/G 14/2

NL





MICROCOPY RESOLUTION TEST CHART
NATIONAL BUREAU OF STANDARDS 1963-A

Section III-2 - Cavity Mirrors for X-Ray Lasers

Part A) Multilayer-Coated Cavity Mirrors

There has been considerable interest in recent years in the possibility of achieving optical amplification at x-ray wavelengths (Forsyth, et al., 1976; Waynant and Elton, 1976). In most schemes, the amplifying region is a plasma formed at or near the focus of a high power visible pump laser (where characteristic temperatures are in the range of 1 keV). Such an x-ray amplifier could form the basis for a true x-ray laser if a cavity of adequate quality could be constructed.

Much of the x-ray laser research conducted to date at the Laboratory for Laser Energetics (LLE) has concentrated on a scheme based on three-body recombination (Bhagavatula and Yaakobi, 1978, Conturie, 1982).

In these experiments, a pulse from the pump laser (duration typically 1 nanosecond) is focussed through a slit of width $\sim 200 \mu\text{m}$ (or past a half-plane) onto a target having a Z of order 10 (the target is typically located $\sim 200 \mu\text{m}$ below the slit). The laser-produced plasma undergoes a jet-like expansion back into the direction of the incident beam, where it is cooled through collision with a cold plasma formed in the slit.

It has been established experimentally that population inversions occur in the rapidly cooled plasma, most probably through the mechanism of three-body recombination (Conturie, 1982).

The most extensively studied inversion is one that has been observed on the $n=4$ to $n=3$ transition in helium-like aluminum (wavelength $\sim 130\text{\AA}$), but inversion has also been observed from a number of low-to-moderate Z targets, and on a number of x-ray transitions (including in particular the

80Å 3-2 transition in hydrogen-like fluorine).

For a frequency-tripled Nd:Yag pump laser ($\lambda = .35 \mu m$), Conturie (1982) has tentatively identified $9 \leq Z \leq 13$ as the region of best performance, which will tend to limit transition wavelengths to the region above 50Å.

For this reason our discussion will initially concentrate on the possibility of using multilayers to form cavity mirrors for the 100Å regime.

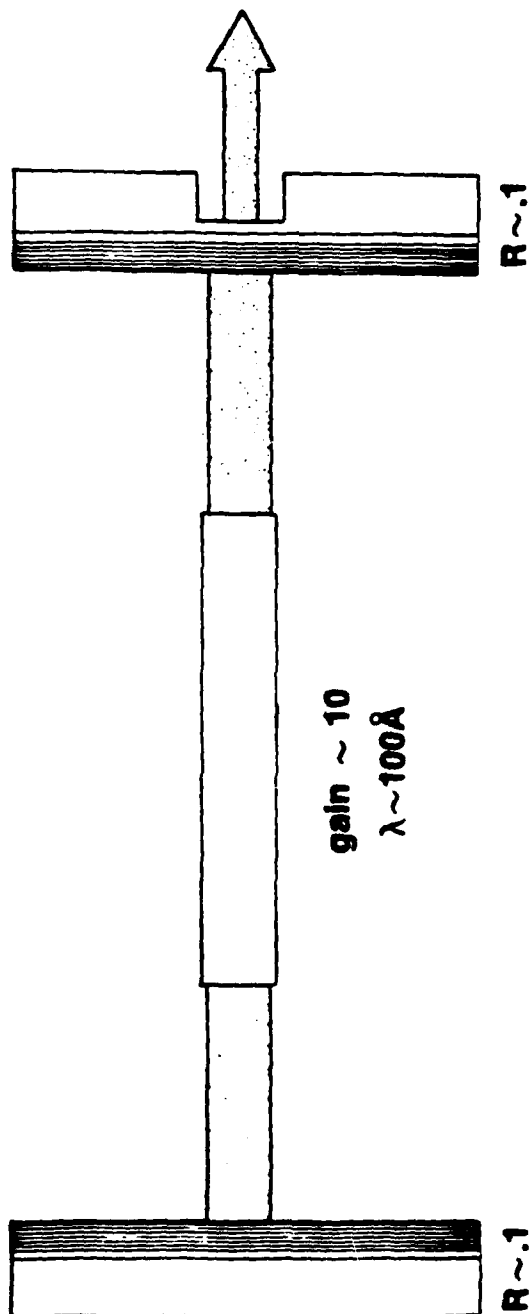
According to fig. II-2-5, the reflectivity of a tungsten-carbon multilayer at such wavelengths will be of order 0.1. As shown in fig. II-2-4, we might hope to achieve higher reflectivities with new materials combinations, but it is clear that in the soft x-ray region, multilayers cannot achieve the reflectivities of virtually unity that are possible in the visible.

However, even with a reflectivity of 0.1, it is possible to get above the threshold for true lasing, and so improve the coherence of the emitted radiation, if the gain in the amplifier can be raised above 10, so that each 90% loss on reflection will be compensated for by a pass through the amplifier (fig. III-2-1).

The key to the two-mirror configuration shown in the figure is that the multilayer structures have been tuned to reflect precisely at normal incidence (i.e. their structures are optimized according to the results of sec. II-2-B), so that each single lossy reflection is compensated for by a pass through the amplifier.

PROPOSED CAVITY CONFIGURATION

LR
LLE



Periodicity of reflecting multilayers has
been tuned to within $\sim 1 \text{ \AA}$

X239

Figure III-2-1

III-2-4

According to eqs. II-3-20 and I-11, the absolute tolerance on systematic error in the unit cell thickness d that is imposed by the need to have adequate reflectivity at normal incidence is

$$\delta d_{(A)} \cong \frac{d_{(A)}}{\pi} \cdot \delta \varphi_{FWHM} \cong 1.3 \times 10^{-6} (2d_{(A)})^3 \quad (\text{III-2-1})$$

If these tolerances are not met, so that the multilayer resonance angle is not sufficiently near $\theta = 0^\circ$, one might turn to a cavity configuration like that shown in fig. III-2-2a, where a grazing reflection is employed to return the beam to the second mirror.

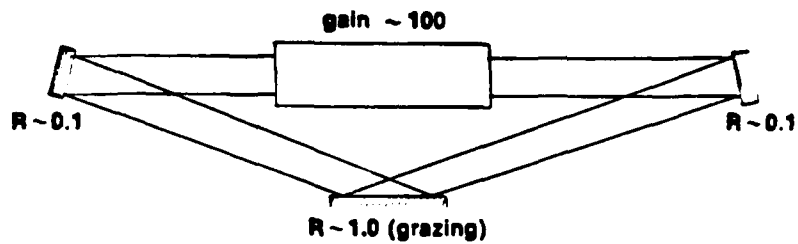
However, there are now two lossy, near normal-incidence reflections required for every pass through the amplifier, so that a higher gain is required than is needed with the two mirror cavity.

Further, because of the symmetry that exists between the grazing regime and the normal incidence regime (see sec. II-3), we can show that when the multilayer's detuning error is sufficient to rule out the configuration of fig. III-2-1, the grazing reflection will then likely occur at too large an angle for efficient reflection.

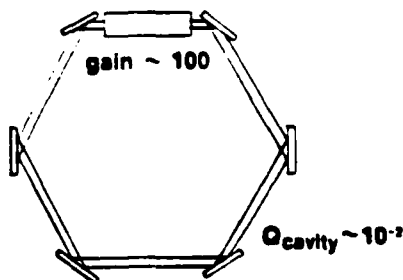
According to eq. II-3-39, the half-angular width of the multilayer reflectance profile at normal incidence is

$$\delta \theta_{FWHM} \cong \sqrt{\frac{2\Delta''}{\pi}} \cong \sqrt{\frac{2\Delta_n''}{\pi}} \quad (\text{III-2-2})$$

OTHER CAVITY CONFIGURATIONS



A. Cavity formed from non-optimal multilayers



B. Ring cavity formed from grazing reflectors

Ring should contain at least M mirrors, where

$$M = \sqrt{\frac{\pi^3 \operatorname{Im}(n)}{2(1 - \operatorname{Re}(n))^{5/2} \ln 2}}$$

Refractive index of mirror material is n .

The limiting Q is given by

$$Q = \exp \left[-4\pi \frac{\operatorname{Re}(\sqrt{n^2 - 1})}{|n^2 - 1|} \right]$$

X333

Figure III-2-2

assuming $\beta \approx 1$, $\Delta_1 \ll \Delta_n$. This is also the approximate half-width of the region about normal incidence within which $\delta\theta_{FWHM}$ is approximately constant. The critical angle (no longer a sharply defined cutoff at long wavelengths) is given by $\theta_c = \sqrt{2|\Delta'_s|}$, where $1+\Delta_s$ is the index of the bulk reflector. In order that the two-mirror scheme of fig. III-2-1 be ruled out while the scheme of fig. III-2-2a be still worthwhile,

$$\sqrt{2|\Delta'_s|} \geq 2 \cdot \sqrt{\frac{2\Delta_n''}{\pi}} \quad (\text{III-2-4})$$

or

$$|\Delta'_s| \geq \frac{4\Delta_n''}{\pi} \quad (\text{III-2-5})$$

Even in the soft x-ray regime where absorption is quite significant, it will generally be possible to technically satisfy eq. III-2-5. Nonetheless, it is clear that in addition to implying a greater loss per cavity transit, the incorporation of a grazing reflection as in fig. III-2-2a will not greatly reduce the fabrication requirement of eq. III-2-1, because it will not in general be possible to satisfy the inequality of eq. III-2-5 in a strong way.

III-2-7

For the above reasons we consider the most promising cavity configuration for an x-ray laser in the 100\AA regime to be one based on normal incidence multilayers.

Part B) Ring Cavity

The degradation mechanisms discussed in sec. III-1 imply that the cavity configuration of fig. III-2-1 will become inadequate for transition wavelengths shorter than about 40\AA .

At short wavelengths one might attempt to configure the multilayers in a polygonal ring in order to increase the $2d$ -spacing, but the resulting exponentiation of the reflection loss will imply a low overall throughput (the ideal single-pass resonant reflectivity from multilayers can be at most 0.8 in the soft x-ray regime).

However, as the angle of incidence against a specular reflecting surface goes to zero, the reflectivity can approach unity.

On this basis, Bremer and Kaihola (1980) have devised a ring cavity in which a large number of grazing reflections from polished substrates are used to return the beam to the amplifier (fig. III-2-2b). They have shown that if the ring contains sufficiently many mirrors, the fraction of the beam returned to the amplifier approaches the limiting value

$$Q \approx e^{-\sqrt{2} \pi \frac{\Delta''}{|\Delta'|^{3/2}}} \quad (\text{III-2-6})$$

where $n_s = 1 + \Delta_s$ is the index of the mirror material.

In Appendix 13, we show that in order to approach the limiting throughput, the ring must contain at least $M_{1/2}$ reflectors, where

$$M_{1/2} \approx 5 \sqrt{\frac{\Delta''}{|\Delta'|^{3/2}}} \quad (\text{III-2-7})$$

(We note that $M_{1/2}$ is often substantially larger than the number of mirrors that would be required simply to put the incidence angle at the critical angle). The fall-off in R as the number of mirrors is decreased below $M_{1/2}$ is very rapid.

We also show in Appendix 13 that a general formula for the throughput in S polarization when $M \gg M_{1/2}$ is

$$Q_s = e^{-4\pi \frac{\text{Re}(\sqrt{n_p^2 - 1})}{|n_p^2 - 1|}} \quad (\text{III-2-8})$$

Eq. III-2-8 can differ substantially from eq. III-2-6 in the ultrasoft x-ray regime.

Using eq. III-2-6, and the limited set of x-ray optical constants that were then available, Bremer and Raihola (1980) identified two wavelength-reflector combinations where moderately high performance might be expected; these are polystyrene at $\lambda = 67.6\text{\AA}$ ($Q_s = 0.04$), and magnesium at $\lambda = 2.1\text{\AA}$ ($Q_s = 0.3$).

They reported that even performances such as these appeared generally to be limited to isolated wavelength-material combinations. Further, a literature review reveals that the particular optical constants measurements which form the basis for the 67.6\AA polystyrene reflector have essentially been retracted by the spectroscopist who made the measurements (Lukirskii et al., 1965, initial results reported in Lukirskii et al., 1964).

In addition, application of eq. III-2-7 to the 2.1\AA Mg reflector indicates that the ring will require approximately 240 reflections. Even if one avoided the resulting alignment problem by using a cylinder rather than a polygon, the minimum allowable size of each facet (dictated either by the amplifier length or by damage considerations) would probably imply a cavity circumference greater than one meter. Thus, one would have to add to the formidable difficulty of achieving amplification at short wavelengths, the need to maintain the inversion for even longer than the nanosecond durations that are contemplated in the 100\AA regime.

For these reasons we initially considered the ring cavity to be considerably less promising than the multilayer configuration of fig. III-2-1.

However, we have recently conducted a materials search using the recent compilation of optical constants made by Henke et al. (1982). The results are shown in table III-2-1; in the longer part of the soft x-ray spectrum the search program has identified cavity materials that yield nominal throughputs of up to 0.4.

While these are not as high as the reflectivities that are obtained in a search for multilayer materials (fig. II-2-4), they are certainly high enough to make the ring cavity look quite interesting for transition wavelengths above $\sim 65\text{\AA}$.

Optimum Materials for Ring Cavity

λ (Å)	Q (S Pol)	M(1/2)	M(Crit)	Element
124.000	.3641025953573	7.51	7.29	RHODIUM
121.040	.3921299229287	7.47	7.54	RHODIUM
118.151	.4182819668938	7.44	7.80	RHODIUM
115.331	.3955354172620	7.98	8.11	RHODIUM
112.578	.3566595935351	8.71	8.40	RHODIUM
109.891	.3291879913218	9.32	8.67	RHODIUM
107.268	.2850703515461	10.24	8.96	RHODIUM
104.707	.2522392515925	10.83	9.05	RUTHENIUM
102.208	.2264432242987	11.57	9.31	RUTHENIUM
99.768	.2023748964901	12.34	9.58	RUTHENIUM
97.387	.2029227829216	12.62	9.80	SILVER
95.062	.2125785074919	12.94	10.22	SILVER
92.793	.1775126130385	14.24	10.64	SILVER
90.578	.1483135039153	15.53	11.05	SILVER
88.416	.1163074612112	17.19	11.51	SILVER
86.306	.0890465894562	17.88	11.28	RUTHEN.
84.246	.0740252495011	19.06	11.59	RUTHEN
82.235	.0629664087553	20.16	11.90	RUTHEN
80.272	.0540046097159	24.38	14.03	INDIUM
78.356	.0584580751483	25.19	14.71	INDIUM
76.485	.0628288060968	26.04	15.42	INDIUM
74.660	.0444836744491	28.89	16.13	INDIUM
72.878	.0299965650159	32.04	16.85	INDIUM
71.138	.0353809877597	30.37	16.36	LANTHUNUM
69.440	.0449242525942	30.39	17.00	LANTHUNUM
67.782	.0558698077888	30.42	17.66	LANTHUNUM
66.165	.0717400426828	30.31	18.42	LANTHUNUM
64.585	.0750066570867	31.28	19.18	LANTHUNUM
63.044	.0416450779567	36.13	19.99	LANTHUNUM
61.539	.0219788948089	41.04	20.71	LANTHUNUM
60.070	.0140820920987	57.01	27.26	CARBON
58.636	.0133696653412	59.19	28.14	CARBON
57.236	.0124442741563	61.66	29.08	CARBON
55.870	.0113654363679	64.43	30.08	CARBON
54.537	.0101470675794	67.71	31.22	CARBON
53.235	.0087420769778	71.40	32.40	CARBON
51.964	.0070910928000	76.14	33.81	CARBON
50.724	.0053461688895	82.02	35.42	CARBON
49.513	.0035967330555	89.62	37.32	CARBON
48.331	.0018793132260	100.91	39.78	CARBON
47.177	.0006449053022	118.27	43.09	CARBON
46.051	.0000561201248	154.81	48.82	CARBON
44.952	.0000249689810	72.20	21.49	CHROMIUM
43.879	.0000234809186	74.10	22.01	CHROMIUM
42.832	.0000226497750	75.92	22.53	CHROMIUM
41.809	.0000213902624	77.90	23.08	CHROMIUM
40.811	.0000199946934	79.99	23.64	CHROMIUM
39.837	.0000185326460	82.25	24.24	CHROMIUM
38.886	.0000173651901	84.41	24.82	CHROMIUM
37.958	.0000160923393	86.77	25.44	CHROMIUM
37.052	.0000147284590	89.27	26.08	CHROMIUM
36.168	.0000133237546	91.91	26.75	CHROMIUM
35.304	.0000121280221	94.63	27.44	CHROMIUM

Table III-2-1

Optimum Materials for Ring Cavity

λ (Å)	Q (S Pol)	M(1/2)	M(Crit)	Element
34.462	.0000106690404	97.59	28.15	CHROMIUM
33.639	.0000094204381	100.67	28.90	CHROMIUM
32.836	.0000081844422	103.95	29.67	CHROMIUM
32.052	.0000069705225	107.46	30.48	CHROMIUM
31.287	.0000058342894	111.31	31.35	CHROMIUM
30.540	.0000051698340	114.91	32.22	CHROMIUM
29.811	.0000043060991	119.01	33.13	CHROMIUM
29.100	.0000035484615	123.49	34.12	CHROMIUM
28.405	.0000028021737	128.37	35.15	CHROMIUM
27.727	.0000022382416	131.57	36.14	COBALT
27.065	.0000021347739	134.56	37.12	COBALT
26.419	.0000020114377	137.72	38.12	COBALT
25.789	.0000018689708	141.06	39.15	COBALT
25.173	.0000021463589	209.34	57.12	BERYLLIUM
24.572	.0000026708443	212.73	58.56	BERYLLIUM
23.986	.0000032707119	216.28	60.03	BERYLLIUM
23.413	.0000041001999	219.67	61.54	BERYLLIUM
22.854	.0000050253768	223.28	63.09	BERYLLIUM
22.309	.0000060673091	227.08	64.68	BERYLLIUM
21.776	.0000077398673	230.37	66.31	BERYLLIUM
21.257	.0000096400645	233.91	67.98	BERYLLIUM
20.749	.0000117805326	237.66	69.69	BERYLLIUM
20.254	.0000146593254	241.24	71.45	BERYLLIUM
19.770	.0000179611181	245.01	73.25	BERYLLIUM
19.299	.0000220340768	248.78	75.09	BERYLLIUM
18.838	.0000284884506	251.93	76.98	BERYLLIUM
18.388	.0000361553334	255.28	78.92	BERYLLIUM
17.949	.0000418610502	259.80	80.91	BERYLLIUM
17.521	.0000486134398	264.33	82.94	BERYLLIUM
17.103	.0000606588480	267.92	85.03	BERYLLIUM
16.694	.0000727212247	272.05	87.17	BERYLLIUM
16.296	.0000881710569	276.03	89.36	BERYLLIUM
15.907	.0001078347626	279.88	91.61	BERYLLIUM
15.527	.0001306676291	283.85	93.91	BERYLLIUM
15.157	.0001593946264	287.71	96.26	BERYLLIUM
14.795	.0001917968792	291.78	98.68	BERYLLIUM
14.442	.0002272059188	296.11	101.15	BERYLLIUM
14.097	.0002694053500	300.41	103.69	BERYLLIUM
13.760	.0003208726122	304.64	106.29	BERYLLIUM
13.432	.0003774263806	309.10	108.95	BERYLLIUM
13.111	.0004432890668	313.57	111.68	BERYLLIUM
12.798	.0005249066838	317.87	114.47	BERYLLIUM
12.493	.0006232975746	322.08	117.34	BERYLLIUM
12.195	.0007324482448	326.50	120.27	BERYLLIUM
11.904	.0008701721502	330.63	123.28	BERYLLIUM
11.620	.0010350574823	334.68	126.36	BERYLLIUM
11.342	.0012161348034	338.98	129.51	BERYLLIUM
11.071	.0014132805211	343.52	132.74	BERYLLIUM
10.807	.0016628845464	347.69	136.06	BERYLLIUM
10.549	.0019342937161	352.12	139.45	BERYLLIUM
10.297	.0022503197159	356.49	142.92	BERYLLIUM
10.052	.0025908233891	361.12	146.48	BERYLLIUM
9.812	.0029804056776	365.73	150.13	BERYLLIUM
9.577	.0034261007700	370.30	153.86	BERYLLIUM

Table III-2-1

(continued)

Optimum Materials for Ring Cavity

λ (Å)	Q (S Pol)	M(1/2)	M(Crit)	Element
9.349	.0039327952120	374.87	157.69	BERYLLIUM
9.126	.0044725829306	379.69	161.61	BERYLLIUM
8.908	.0051194666344	384.24	165.63	BERYLLIUM
8.695	.0058052048274	389.06	169.74	BERYLLIUM
8.488	.0065269399242	394.14	173.95	BERYLLIUM
8.285	.0073827789902	398.95	178.27	BERYLLIUM
8.087	.0083597341518	403.63	182.69	BERYLLIUM
7.894	.0093833485641	408.61	187.22	BERYLLIUM
7.706	.0105721968466	413.35	191.86	BERYLLIUM
7.522	.0118135474950	418.38	196.61	BERYLLIUM
7.342	.0131696703243	423.46	201.48	BERYLLIUM
7.167	.0147163189309	428.35	206.47	BERYLLIUM
6.996	.0163986744697	433.27	211.57	BERYLLIUM
6.829	.0182406833019	438.19	216.80	BERYLLIUM
6.666	.0203218321951	442.93	222.16	BERYLLIUM
6.507	.0224733434753	447.97	227.65	BERYLLIUM
6.352	.0248780019589	452.85	233.28	BERYLLIUM
6.200	.0274467481236	457.83	239.04	BERYLLIUM

Table III-2-1
(continued)

Part C) Damage

The high temperature environment of the plasma amplifier suggests that damage may be a significant problem for x-ray laser cavities.

While an accurate assessment of the damage threshold can only be made experimentally, there is reason to believe that the limitation imposed by damage may be less severe than one might expect, at least in the context of the LLE recombination laser experiments described in part A.

In the first place, in these experiments amplification does not occur precisely in the focal region. If fig. III-2-1 is oriented with the mirrors at left and right, and if the pump beam is brought from the top to a left-right line focus on a target at bottom, then the region of highest time-averaged gain will be formed near the cooling slit, whose axis will be parallel to the optical axis. The cooling slit will, in turn, be positioned $\sim 200 \mu\text{m}$ above the target. The time-averaged high gain region will have a width of $\sim 200 \mu\text{m}$ and a length approximately equal to that of the line focus. (This time-averaged description is somewhat oversimplified; Conturie's simulations (1982) show that the region of high instantaneous gain travels outward with the velocity of the expanding plasma.)

Thus, the mirrors could be shielded from the hot plasma formed at the focal line, and need see only the relatively cold plasma in the amplifying region near the slit. Conturie's experiments show that the particulate blow-off would not flow isotropically through the slit, but would instead flow preferentially in the direction of the pump laser (Conturie, 1982).

The x-rays emitted by the amplifier are then likely to be the principal agent of damage in the mirrors. Even though most of the x-ray radiation emitted by the plasma may be fluorescent (arising from a number of x-ray transitions), it is the stimulated emission which is most likely to cause damage, because it will be concentrated on a narrow area of the mirrors. Stimulated emission into the coherent spatial modes of the flat-mirror cavity of fig. III-2-1 will undergo virtually no diffraction spreading at the mirrors, because the cavity length can be no more than a few centimeters if coherent oscillation is to be established during the ~ 1 nsec duration of the gain. (This assumes, somewhat arbitrarily for purposes of illustration, that the gain duration is of the order of the pump pulse duration).

For purposes of a rough estimation we will consider the maximum permissible beam energy to be determined by thermal loading on the mirrors. Tungsten has a thermal conductivity $K = 1.78$ Watt/cm $^{\circ}$ K and a heat capacity $C = 0.132$ Joule/gm $^{\circ}$ K (Bechtel, 1975). The thermal properties of graphite are typically $K = 1.29$ Watt/cm $^{\circ}$ K, $C = 0.712$ Joule/gm $^{\circ}$ K (CRC Handbook of Tables for Applied and Engineering Science, 1973).

The distance that heat can propagate in a time t is of order

$$S \sim \sqrt{\frac{Kt}{\rho C}} \quad (\text{III-2-9})$$

which (assuming bulk densities) works out to about 3000\AA in a nanosecond

for either tungsten or carbon.

Using eq. II-3-19, we have that the approximate total thickness of the multilayer stack is

$$D_{(\text{\AA})} \approx Nd_{(\text{\AA})} \approx \frac{1.25 \times 10^5}{2d_{(\text{\AA})}} \quad (\text{II-2-10})$$

Thus, the heated region will not be a great deal thicker than the multilayer stack, so that we can use the thermal properties of the multilayer materials themselves in order to estimate the heat rise.

The melting points of bulk tungsten and carbon are each about 3500 °K. Given a heated volume 3000 Å deep with a cross-sectional area 200 μm across (that of the collimated laser beam), we can estimate that the maximum energy allowed in the beam is $\sim 8 \cdot 10^{-5}$ Joules.

Conturie's simulations indicate that inversion occurs at electron densities of $\sim 10^{20} \text{ cm}^{-3}$ (Conturie, 1982); this corresponds to an ion density of $\sim 10^{19} \text{ cm}^{-3}$ for $Z = 10$. We also assume that recombination could bring as many as 1% of these ions into inversion across the 4-3 transition. At the upper limit in which coherent emission accounts for all de-excitation of the upper level, the total output from a cylindrical amplifier 200 μm in diameter and 1 cm long would then be $\sim 2 \cdot 10^{-4}$ Joules.

Thus, output at the estimated damage limit of $8 \cdot 10^{-5}$ Joules could be regarded as a quite respectable performance in an initial demonstration experiment.

Of course, even for refractory materials like tungsten and carbon, the above method of damage estimation may be unrealistic. For example, the separation between photon absorption sites is only about 20\AA under the above conditions, so that a large number of photoelectrons will be generated in the multilayer stack. (However, based on a crude comparison with the x-ray exposure characteristics of photoresist, one can estimate that the lifetime of these photoelectrons will likely be of order femtoseconds, so that the instantaneous density of secondary electrons will be substantially reduced).

It may be possible to raise the damage threshold somewhat by using curved mirrors to expand the beam. Given the short wavelength, the cavity would have to have a borderline-unstable, near-concentric geometry, in order to produce a narrow diffracting waist at the center of the amplifier. Further, since only a fairly small number of reflections are likely to be possible during the ~ 1 nsec gain duration, the intensity distribution on the mirrors will likely resemble the initial ASE distribution for a significant portion of the shot; therefore the effective illuminated area would likely be little larger than that illuminated by ASE despite the curvature.

According to Slaymaker (1978), the far-field FWHM angular spread of the ASE will be approximately equal to the aspect ratio of the amplifier. We might estimate that if the mirrors are in the mid-field at ~ 1 cm from the ends of an ~ 1 cm amplifier, the ASE illuminated area at the mirrors might be a few times the aperture area. A curved mirror cavity might then succeed in increasing the damage threshold to an extent.

Since each shot will only irradiate a small portion of the mirror surface, it will also be possible, if necessary, to use the multilayers in a quasi-one-shot mode in which most of the surface is masked off during each shot.

We might mention at this point that if future devices operating substantially above lasing threshold should exceed the threshold for mirror damage, it may be possible to devise target configurations that distribute the laser radiation over a larger area of the mirrors.

For example, if one rotated the cooling slit 90° out of the plane of fig. III-2-1, and spaced a number of such slits beneath the cavity axis in a grating-like fashion, then with an appropriate focussing system to generate a focal line beneath each slit, one would form an amplifier that was segmented along the cavity axis, but expanded in the perpendicular direction.

For the above reasons, we feel that there is reason to be optimistic about the question of damage in multilayer cavity mirrors, but of course the uncertainties are such that the issue can only be settled experimentally.

Section III-3 - Multilayer Coatings for Short Wavelength X-ray Microscopy

Part A) Introduction

In this section we consider the possibility of using x-ray multilayers to form spectrally selective coatings for a short-wavelength x-ray microscope. To our knowledge this idea was first conceived at Lawrence Livermore Laboratory, but has not been discussed quantitatively in the literature.

The microscope configuration considered is that invented by Kirkpatrick and Baez (see fig. III-3-1, after fig. 8 of Franks, 1977) and is one of the first x-ray optical systems ever developed (Kirkpatrick and Baez, 1948). This configuration is used at LLE to image the x-ray emission from laser fusion targets. We will discuss our own investigation of possible applications for multilayer coatings in the LLE system.

At present, each of the spherical substrates in the system (radii of curvature about 3600 cm) is coated with a single nickel layer, which is illuminated at a grazing (subcritical) angle to the surface θ . At small θ the spherical substrates are effectively cylindrical because the curvature transverse to the beam possesses virtually no power.

In the longitudinal meridian, however, the substrate can be shown to have a focal length $R \cdot \theta / 2$ (Kirkpatrick and Baez, 1948). Thus, two spherical substrates with crossed orientations can provide the analogue of a thin lens. One may also regard the second element as correcting for an extreme astigmatism.

**CORRECTION OF ASTIGMATISM BY SUCCESSIVE
GRAZING REFLECTIONS FROM TWO MUTUALLY
PERPENDICULAR (CYLINDRICAL) MIRRORS** 

(After A. Franks, 1977)

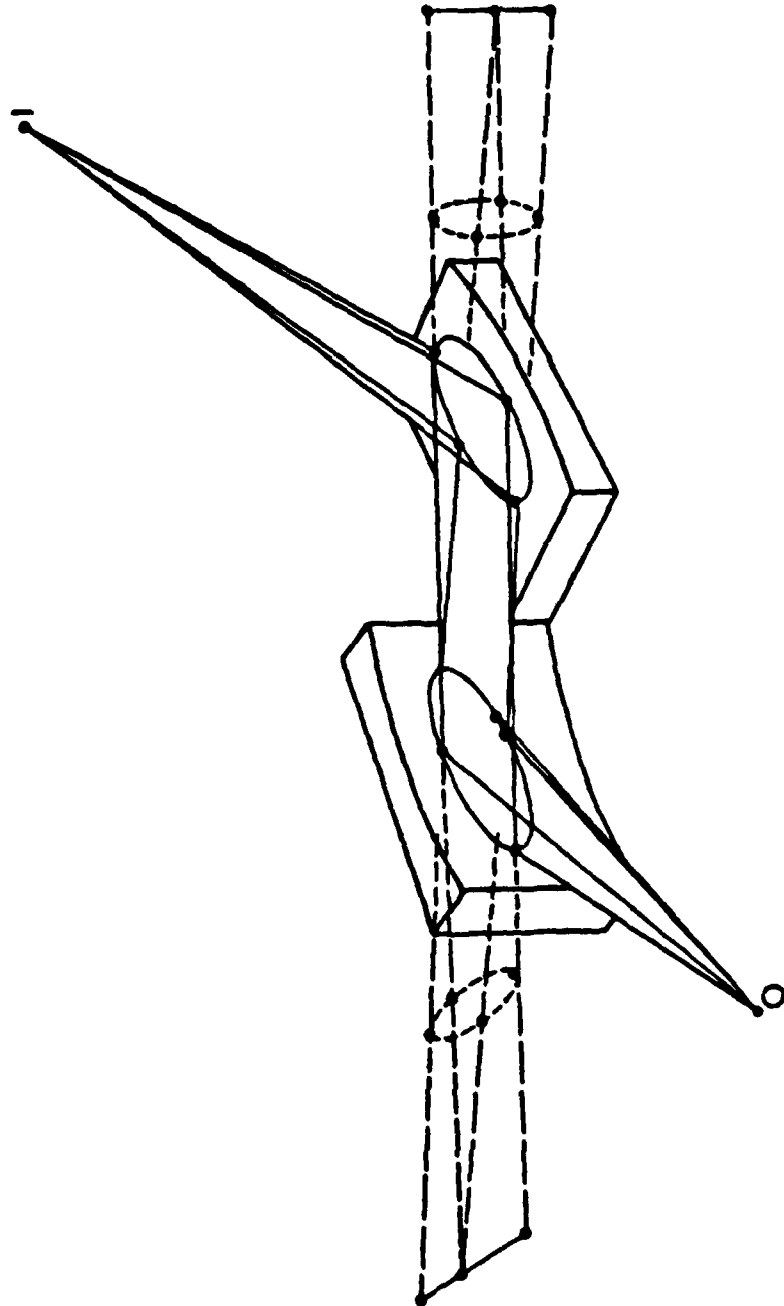


Figure III-3-1

In the configuration in use at LLE, θ is about 0.8° , the working distance is about 20 cm, and the magnification is about 5.

Since the individual substrates are operating very far off-axis (89.2°), the geometrical performance of the overall system is very poor by conventional standards. For a $5\text{ }\mu\text{m}$ resolution at a 20cm working distance, spherical aberration limits the aperture to about $60\text{ }\mu\text{m}$ when $\theta = 0.8^\circ$, and coma limits the field of view to about $200\text{ }\mu\text{m}$ (Hopkins, 1981). This field of view is very small, but is about the size of a laser fusion target.

The aberrations become less severe if θ is increased; however at a given wavelength, a single layer cannot reflect radiation at angles larger than critical. At an angle of 0.8° to the surface, the shortest wavelength that the present nickel coating can reflect is about $2.5\text{ }\mu\text{m}$.

In this section we discuss the possibility of converting the single layer coating to a spectrally selective multilayer coating in order to bring the operating wavelength down to the $1.5\text{ }\mu\text{m}$ regime, while maintaining the angle of incidence at about 0.8° .

The spectral selectivity can be very useful in laser fusion diagnostic applications. For example, the spectral selectivity permits discrimination between the x-rays emitted in the core of a laser fusion target, and those emitted by elements in the target's shell. (At short wavelengths, most of the x-rays are emitted into isolated spectral lines having species-dependent wavelengths, rather than into continuum). The spectral selectivity could also be used to discriminate between x-rays emitted by the primary target and those emitted by a backlighting source (Richardson,

1981).

With multilayer coatings and short wavelength illumination, one can operate the microscope at angles of up to a few degrees from the surface before the required 2d-spacing becomes impractically small.

However, eq. II-3-23 shows that the acceptance angle or field of view of the coating will decrease as the angle to the surface is increased. We may regard a single layer coating as a limiting version of a multilayer, so eq. II-3-23 implies that the acceptance angle of a multilayer coating must necessarily be smaller than that of the single layer. As θ is increased, the limitation imposed on field of view by the coating will eventually become equal to that imposed by coma; at this point one begins to trade off field of view for increased collection aperture and resolution (the spherical aberration continues to improve as θ is increased).

In the present application, we wish to maintain the field of view at the $\sim 150\mu m$ limit imposed by geometrical aberrations in the single layer system; this requires that θ remain at 0.8° , which, it turns out, is the angle at which the acceptance angle of a tungsten-carbon multilayer becomes approximately equal to the angular field allowed by coma (see below).

In future systems, it might be worthwhile to exploit the trade-off between coating acceptance angle and increased collection aperture, by having the system operate at an angle of 2° or so; such a system could be used to obtain high resolution, narrow field images of the small compressed core of a laser fusion target. Further, if the hard x-ray emission from a source were broad-band, it would be possible to use a larger θ system

without decreasing the field of view.

The alignment and fabrication tolerances in the larger ξ systems would be more stringent than those in the $\xi = 0.8^\circ$ system discussed here, however.

The maximum angle at which a single layer coating can reflect is given by (Bilderback, 1982)

$$\xi_c = 1.6 \times 10^{-3} \sqrt{\rho_{(g/cm^3)}} \lambda_{(\text{\AA})} \quad (\text{III-3-1})$$

which at $\rho = 20 \text{ gm/cm}^3$ and $\lambda = 1.66\text{\AA}$ gives $\xi = 0.7^\circ$. Since the present system is designed to operate at an angle of 0.8° , the principle advantage gained with multilayer coatings over high density coatings in our application is that multilayers are spectrally selective.

Part B) Calculation of Performance

Fig. III-3-2 shows the calculated spectral and angular selectivity of tungsten/carbon multilayer coatings designed to convert the LLE Kirkpatrick-Baez microscope from operation at a minimum wavelength of 2.5\AA to operation at 1.66\AA (Ni- K_{α}). The calculations use $\lambda = 1.66\text{\AA}$, which is the wavelength of low temperature Ni- K_{α} emission. The actual line used would be the Be-like resonance line, which would have a slightly different wavelength.

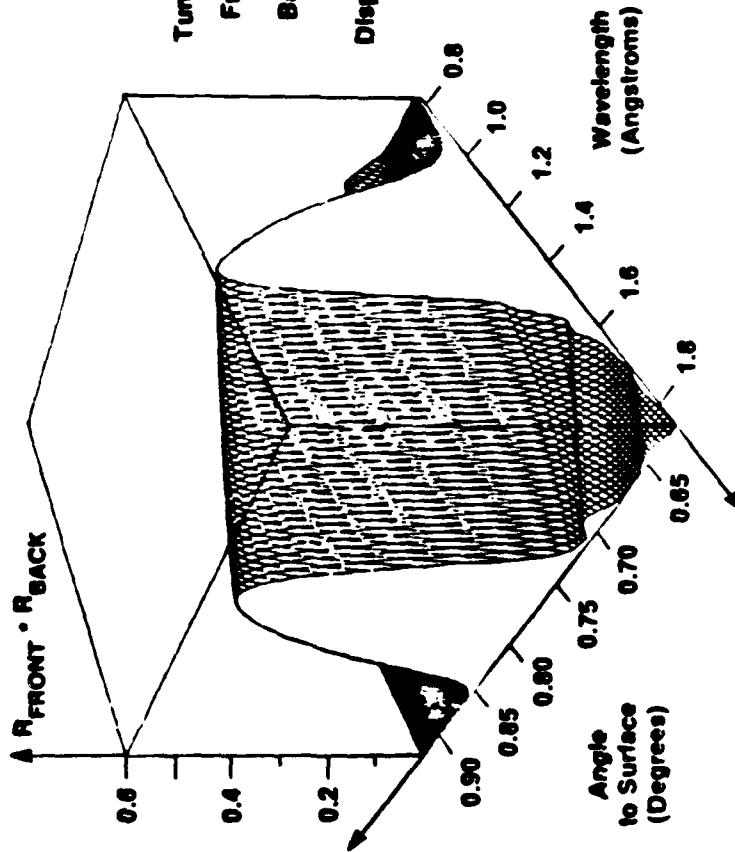
The thicknesses chosen for the coating are $d_w = d_c = 40.0\text{\AA}$ in the front mirror ($2d = 160\text{\AA}$), and $d_w = d_c = 41.5\text{\AA}$ for the rear mirror ($2d = 166\text{\AA}$).

It might ultimately be worthwhile to reoptimize the thickness ratio slightly; however, large changes in the ratio would cause a decrease in performance. A multilayer with a substantially thinner W layer would have higher reflectivity, but only at the expense of quite severely restricting the field of view. A substantial increase in the W thickness could increase the field of view, but only at the expense of rapidly degrading the double mirror reflectivity. A small change in the thickness ratio from $d_w = d_c$ would cause only small changes in the performance of the coating.

Fig. III-3-2 also assumes that different coatings are used on the two mirrors of the Kirkpatrick-Baez pair; this compensates for the difference in angle of incidence that results from the different distances of the two mirrors from the target.

MULTILAYER-COATED X-RAY MICROSCOPE

Spectral and Angular Sensitivity



Tungsten-Carbon Multilayers

Front mirror:

$d_w = d_c = 40 \text{ \AA}$

Back mirror:

$d_w = d_c = 41.5 \text{ \AA}$

Dispersion neglected.

Figure III-3-2

X332

Only about 4 layer pairs are required to approach the absorption-limited peak reflectivity. Comparison of this value with eq. II-3-19 shows that the soft x-ray approximations of sec. II-3 are becoming inaccurate at the present short wavelength.

In fact, the number of layers participating in the reflection is becoming sufficiently small that inaccuracy in the basic x-ray formalism derived from eq. II-1-20 is becoming noticeable.

We have found that our formalism is still accurate to about 1% in its calculation of peak reflectivity, but becomes increasingly inaccurate in the wings; in addition the calculated position of the reflectance peak is off by about 15%. For these reasons we have performed the final calculations in this section numerically, with the x-ray formulas used only to determine trial values for the parameters. The numerical calculations are carried out with the non x-ray characteristic matrix solution of eq. II-1-22.

The calculations use densities measured by Barbee (1981) of 15 gm/cm³ and 2 gm/cm³ for the tungsten and carbon layers, respectively. The real index of refraction used for tungsten is based on anomalous dispersion data obtained by Brentano and Baxter, as quoted in Table IV.11 of James (1965). The real index for carbon was calculated with the free electron model. The imaginary indices for tungsten and carbon are based on data obtained by Henke et al. (1982).

The optical constants used are

$$\Delta_w = -4.12 \times 10^{-5} + i 4.14 \times 10^{-6}$$

(II-3-2)

$$\Delta_c = -7.44 \times 10^{-6} + i 1.38 \times 10^{-8}$$

Despite the small number of layer pairs required at the center of field, we have chosen to use 35 pairs in the system. Even with 35 pairs, there is still a faint residual ringing in the image outside the $\pm 150 \mu m$ field. (This is a consequence of extinction being due to depletion by back-reflection, rather than by absorption).

The worst drawback to the coating is probably the limitation that its finite acceptance angle imposes on the microscope's field of view. This limitation is probably tolerable; the angular FWHM of double reflectance for an ideal coating is 0.08 degrees at $\lambda = 1.66 \text{ \AA}$, which, as indicated, leads to a ± 150 micron field of view at a working distance of 21cm; this represents only a slight decrease from the field of view allowed by aberrations. However, the narrow field leaves little margin for error in designing and fabricating the coating.

The angular boundaries of the zone of high double reflectance from the multilayer are reasonably sharp, even though the zone is somewhat asymmetric. (Because of the asymmetry, the angle of peak reflectivity has been decentered from the optical axis). The wavelength response of the coating is fairly broad. Neglecting dispersion, the nominal wavelength range (FWHM of the double reflectance curve) is from 1.5 \AA to 1.8 \AA . (With dispersion included the range becomes 1.55 \AA to 1.75 \AA .)

The tolerance on the layer thicknesses, as far as maintaining high reflectivity for an on-axis point is concerned, is comparatively mild, about $\pm 4 \text{ \AA}$. However, despite the relatively wide range of layer thicknesses that can provide high on-axis reflectivity, there is little margin for error in the alignment of the zone of high reflectance with the

optical axis (assuming a quasi-monochromatic source). Therefore it would be preferable to be able to accurately calibrate the deposition system in an effort to obtain layer thicknesses accurate to about 1\AA .

The 9mm separation between the two mirrors implies a difference in incidence angle of 0.03 degrees. Fortunately this is somewhat smaller than the 0.08 degree FWHM of the coating. However, because of the need to center the high reflectance zones of both coatings accurately, one would prefer that the two coatings be made with slightly different 2d-spacings.

To consider the effect of fabrication error, suppose that the layer thicknesses are 39\AA instead of 40\AA , and that the same coating is used on both mirrors. One then finds that the optical axis intersects the half-maximum of the double reflectance curve, so that roughly speaking only half of the field will be imaged (i.e. the angular half-width of the field is zero). If the second coating is independently optimized, and has the desired layer thicknesses of 41.5\AA , the angular half-width in the previously un-imaged direction becomes 0.025 degrees (given the same 1\AA systematic error in the layers of the front mirror). If the intended thicknesses of the layers of the second coating are 41.5\AA , but they instead have an error equal to that in the first coating (so that their thickness is 40.5\AA), the angular width becomes 0.021 degrees. If the layers of the second coating have the same errors in the opposite direction (i.e. a thickness of 42.5\AA), the half-width becomes 0.03 degrees. (As mentioned above, with no errors in the independently specified coatings, the half-width is 0.04 degrees.)

Thus, the use of a different target thickness in the rear coating will definitely reduce the sensitivity to error.

The coatings should be relatively insensitive to other kinds of defects in structure, due to the large 2 δ -spacings.

From the 36m radius of curvature, the 60 micron aperture, and the working distance of 21cm, one can calculate that that the variation in angle of incidence across the aperture due to curvature of the mirrors is 0.0075 degrees. (The main variation is due to displacement in the longitudinal direction).

Thus, the narrow 0.08° bandwidth of the coatings will not reduce the aperture of the system.

**NU
DATE
ILME**